CHALMERS
UNIVERSITY OF TECHNOLOGY

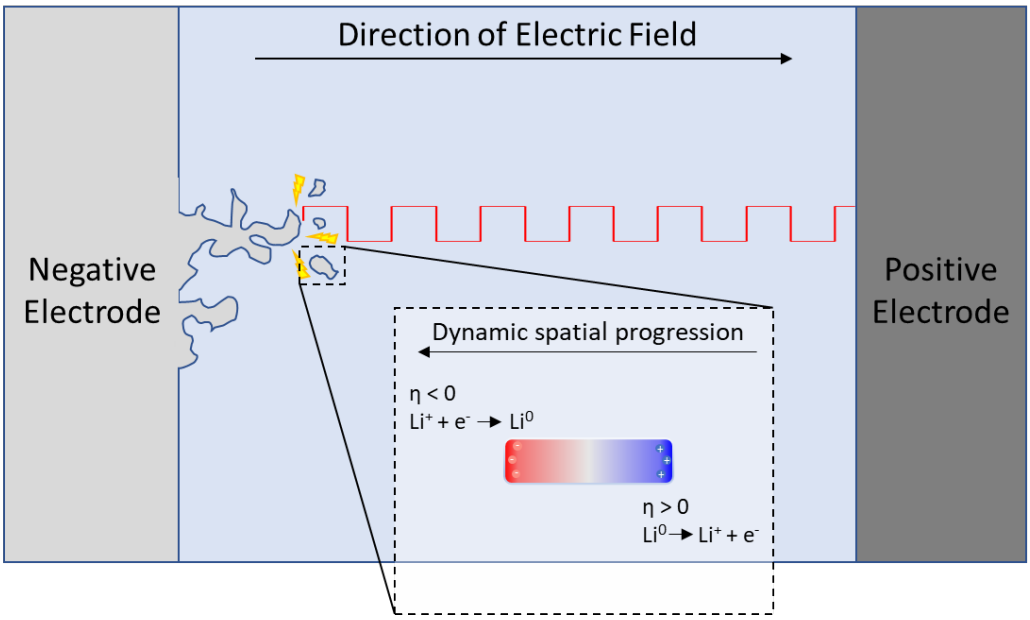

Regeneration of Lithium-Ion Cells

An Initial Investigation of the Potential for Regeneration in Lithium-Battery Cells as a Method to Extend the Life-Cycle

Master's Thesis in Sustainable Energy Systems

ELIN DUFVENIUS ESPING & MARCUS RASMUSSEN

DEPARTMENT OF CHEMISTRY AND CHEMICAL ENGINEERING
CHALMERS UNIVERSITY OF TECHNOLOGY
Gothenburg, Sweden 2023
www.chalmers.se

Master's thesis 2023

Regeneration of Lithium-Ion Cells

An Initial Investigation of the Potential for Regeneration in Lithium-Battery Cells as a Method to Extend the Life-Cycle

ELIN DUFVENIUS ESPING
MARCUS RASMUSSEN

CHALMERS
UNIVERSITY OF TECHNOLOGY

Department of Chemistry and Chemical Engineering
Division of Energy and Materials
Chalmers University of Technology
Gothenburg, Sweden 2023

Regeneration of Lithium-Ion Cells
An Initial Investigation of the Potential for Regeneration in Lithium-Battery Cells as a Method to Extend the Life-Cycle
ELIN DUFVENIUS ESPING
MARCUS RASMUSSEN

Supervisor: Hafid Zehri, Volvo Group Truck Technology
Examiner: Martina Petranikova, Department of Chemistry & Chemical Engineering

Master's Thesis 2023
Department of Chemistry and Chemical Engineering
Division of Energy and Materials
Chalmers University of Technology
SE-412 96 Gothenburg
Telephone +46 31 772 1000

Cover: Schematic illustration of a regenerative approach to recover capacity lost in aged lithium-ion battery cells.

Typeset in LaTeX
Printed by Chalmers Reproservice
Gothenburg, Sweden 2023

Regeneration of Lithium-Ion Cells
An Initial Investigation of the Potential for Regeneration in Lithium-Battery Cells as a Method to Extend the Life-Cycle
ELIN DUFVENIUS ESPING & MARCUS RASMUSSEN
Department of Chemistry & Chemical Engineering
Chalmers University of Technology

Abstract

Electric Vehicles (EVs) are a key factor in the vision of reaching the goal of net-zero emission by 2050, and Lithium-Ion Batteries (LIBs) are one of the most promising technologies for EVs in this pursuit. However, as the demand for LIBs increase, the waste generated by the spent batteries also increases. From a material supply shortage perspective, as well as a waste management perspective, further improvements are needed to achieve a more sustainable approach. While recycling is an important aspect, regeneration could provide a more efficient solution by extending the LIB lifecycle. In this work, a study to investigate the potential for capacity regeneration of lithium-ion cells was initiated. The aim was to develop and validate a general non-invasive regenerative approach which in the long run could be implemented into the Volvo battery management system.

Lithium-ion cells were aged with two different charging rates during a two-month period, after ageing, three different regenerative approaches were investigated. The cells consisted of an NMC cathode. Performance tests and Electrochemical Impedance Spectroscopy (EIS) were performed before ageing, after ageing and after regeneration to quantify the effects of ageing as well as regeneration. Differential Analysis and EIS were used to identify the different modes of degradation occurring in the cells, meaning Loss of Active Material (LAM) and Loss of Lithium Inventory (LLI). The cells were cycled for 365 cycles and displayed a maximum capacity fade of 3.18 %, reaching around 97 % State of Health (SoH). Furthermore, LAM, LLI and internal resistance increase were identified as plausible causes for capacity fade.

Three different regeneration approaches were investigated based on crystal spatial movement, current pulses and a combination if spatial and current pulses. Electrochemical characterization suggested additional capacity fade after the end of regeneration for all approaches. However, an indication towards regained active anode material was observed for all regenerated cells. The combination of crystal spatial movement and current pulses showed indications of regained lithium inventory. Further investigations and results validation are required to confirm those results.

Keywords: lithium-ion batteries, battery degradation, loss of active material, loss of lithium inventory, capacity regeneration.

Acknowledgements

This thesis in Sustainable Energy Systems was conducted during the spring of 2023 as part of the Master's programs Material's Chemistry and Physics at Chalmers University of Technology. It was done at the Division of Energy and Materials at the Department of Chemistry and Chemical Engineering in collaboration with Volvo Group Truck Technology.

Firstly, we would like to thank and express our deepest gratitude to our supervisor at Volvo, Hafid Zehri, without whom the idea of trying to regenerate lithium-ion batteries would not have been materialized. Thank you for all the support, feedback and valuable discussions during this period. It's been a pleasure working with you.

We would also like to thank Gustav Giske who helped us immensely during the initial parts of the thesis, and continued to provide valuble feedback and ideas all throughout.

A big thank you to the entire ESS Component Verification team in CampX at Volvo Group Truck Technology. Thank you for welcoming us to the team, inviting us to social gatherings, sharing your knowledge and providing us with valuable help and support throughout the whole process. A special thanks to Fareed Ahmed whose expertise using electrochemical impedance spectroscopy was truly invaluable.

We would also like to extend our appreciation to Elin Dornerus for valuable discussions and helping us investigate the use of material characterization. Thank you.

We would furthermore like to like to express our gratitude to our examiner Martina Petranikova for the help and support throughout the thesis.

Elin Dufvenius Esping & Marcus Rasmussen, Gothenburg, June 2023

List of Abbreviations

Acronyms

AA	After Ageing
AC	Alternating Current
CC	Current Collector
CCCV	Constant Current Constant Voltage
CF	Capacity Fade
CL	Conductivity Loss
CPE	Constant Phase Element
CT	Charge Transfer
DC	Direct Current
DCIR	Direct Current Internal Resistance
DVA	Differential Voltage Analysis
ECM	Equivalent Circuit Model
EIS	Electrochemical Impedance Spectroscopy
EoL	End of Life
ESS	Energy Storage System
EV	Electric Vehicle
HOMO	Highest Occupied Molecular Orbital
ICA	Incremental Capacity Analysis
LAM	Loss of Active Material
LAM_{NE}	Loss of Active Negative Electrode Material
LAM_{PE}	Loss of Active Positive Electrode Material
LCA	Life Cycle Analysis
LIB	Lithium-Ion Battery
LLI	Loss of Lithium Inventory
LUMO	Lowest Unoccupied Molecular Orbital
PF	Power Fade
RPT	Reference Performance Test
SEI	Solid Electrolyte Interface
SoC	State of Charge
SoH	State of Health
OCV	Open Circuit Voltage

Chemicals

Al	Aluminium
C	Carbon
Co	Cobalt
Cu	Copper
Dead Li	Dead Lithium
G	Graphite
H	Hydrogen
i-Li	Isolated Lithium
LCO	Lithium Cobalt Oxide
LFP	Lithium Iron Phosphate
Li	Lithium
LMO	Lithium Manganese Oxide
LPF	Lithium Hexafluorophosphate
M	Manganese
Ni	Nickel
NMC	Nickel Manganese Cobalt
O	Oxygen
Pb	Lead
S	Sulphur
Si	Silicon

Symbols

α		Constant Phase Element Exponent	[a.u.]
η		Overpotential	
μ		Potential	[V]
	μ_a	Anode Potential	
	μ_c	Cathode Potential	
ω		Frequency	[Hz]
Φ		Electric Potential	[V]
	Φ_{Li}	Electric Potential of Lithium	
	Φ_{I}	Electric Potential of Electrolyte	
ϕ		Phase Shift	[°]
C		Capacitance	[F]
E		Potential	[V]
	E_{eq}	Potential of Lithium Deposition/Dissolution	
I		Current	[A]
L		Inductance	[H]
Q		Capacity	[Ah]
R		Resistance	[Ω]
	$R_{\mathrm{CT/SEI}}$	Charge Transfer & SEI Resistance	
	R_{Ω}	Ohmic Resistance	
	$R_{x\mathrm{s}}$	Direct Current Internal Resistance After x Seconds	
t		Time	[s]
V		Voltage	[V]
	V_{max}	Maximum Voltage	
	V_{min}	Minimum Voltage	
	V_{OC}	Open Circuit Voltage	
Z		Impedance	[Ω]
	Z_{cap}	Impedance of ECM Capacitor	
	Z_{CPE}	Impedance of ECM	
	Z_{res}	Impedance of ECM Resistor	

Contents

List of Figures

List of Tables

1

Introduction

The release of carbon dioxide into the atmosphere through the combustion of fossil fuels is recognized as a significant contributor to climate change. This poses a threat to the ecosystem as well as the economy. The global transport sector consumes a quarter of the total energy consumption and accounts for nearly 40 % of the emissions from end of use. As of 2022, oil dominated in transport, accounting for 90 % of consumption [1]. One of the largest markets for heavy-duty trucks internationally is the United States. These vehicles play a essential role in the nation's transportation system. Specifically, trucks account for over 72.2 % of the country's total freight movement by weight, signifying their impact within the economy [2]. However, to reach the goal of net-zero emission by 2050, the transportation sector is required to reduce its carbon dioxide and nitrogen oxides emissions, where the most prominent solution appears to be a shift from combustion engines to electric motors.

Lithium-based battery technologies has experienced tremendous commercial and academic progress over the past 30 years. The rechargeable Lithium-Ion Battery (LIB) has been vastly used in many applications due the many advantages. LIBs posses high gravimetric and volumetric energy densities. Combined with low self-discharge and cyclability, makes them suitable for both stationary and mobile applications. Therefore, they have been proven to be an efficient Energy Storage System (ESS). In addition, LIBs are one of the most promising candidates full electrification of transport vehicles (EVs). As by 2050, two billion batteries would be needed on the roads in addition to the global electricity demand nearly doubling [1]. The tangible and ubiquitous demand for high-performance batteries, and the added interest in green energy technology caused by climate change, has led to a tremendous growth of battery research. Though, from a materials supply shortage perspective to battery waste management, and improving the sustainable approach towards net-zero emission, further developments in battery technology are needed to support the green transition towards a more responsible use of the finite resources.

At Volvo AB, sustainability has been one of its core values driving its development since the 1970s, with electromobility being one of the more important factors evaluated in recent years. In order to meet the goals set forward in the Paris Agreement, Volvo aspires to be net-zero of greenhouse gases by 2040. On top of the climate goals, Volvo also strives for circularity, and more specifically a strengthened life-cycle management for their batteries. Recovery of materials and prolonging the

lifetime of batteries goes hand in hand with Volvo's aspirations today.

Currently, all batteries in the European Union must have a minimum of 50 % of their weight recycled [3]. Yet, there is no further specification provided for recycling of lithium-ion batteries, meaning that companies may choose their approach depending on which materials they want to focus on as long as they reach the requirement of 50 wt%. Hence the focus is naturally on the most valuable material, which currently is cobalt (34.18 $/kg at the time of writing). However, a proposition by the European Commission to the European Parliament aims to revise the current legislation [4]. The result would be to first increase the required recycling weight of lithium-ion batteries to 65 % by 2025, with additional requirements on the material recovery rates. The required rates would be 90 % for cobalt, nickel and copper, as well as 35 % for lithium. In 2030 the EU suggests a further increase to 70 % of the total weight recycled, with specific requirements of 95 % for cobalt, nickel and copper, and 70 % for lithium [5].

Regeneration of LIBs could provide an efficient extension of the battery life-cycle, aiding in this ongoing transition. Initial research investigations have demonstrated promising results to recover some of the performance lost with age and use of LIBs after reaching their End of Life (EoL). Lead-acid battery regeneration techniques have already been established, where the most common causes for failure are a culmination of sulfation accumulating on the battery plates [6, 7]. The most efficient solution has proved to be pulse technology, where parameters such as frequency, amplitude, duty cycle, and relaxation time were shown to affect the battery performance [8]. In the case of LIBs, one prominent degradation mechanisms causing capacity loss is the formation of inactive, or dead, lithium (i-Li). *Chengbi et al.* have presented a lithium restoration method based on a series of iodine redox reactions, effectively rejuvenating dead lithium [9]. Still focusing on i-Li: despite the loss of electrical connection, in further research [10], *Liu et al.* theorize that the exposure of i-Li to an external electric field would induce a separation of positive and negative charges across the ends of the i-Li islands. It was reported that during charge, as the lithium-ions move from the positive electrode (cathode) to the negative electrode (anode), the i-Li fragments move towards the positive electrode trough spatial progression. Moreover, as the overpotential at the end of the i-Li near the positive electrode became negative, local lithium deposition occurred. Meanwhile, the overpotential at the other end became positive, leading to local lithium dissolution. Charge neutrality is ensured and maintained by electron transport from one side to the other of the i-Li, while enabling the simultaneous occurrence of deposition and dissolution at its ends. This results in dynamic spatial progression of the i-Li towards the positive (negative) electrode during charge (discharge), which can lead to reconnection, and thus a potential recovery mechanism for i-Li was discovered.

1.1 Aim

The aim of the thesis is to develop and validate a general, non-invasive capacity regeneration approach. To achieve capacity regeneration, the underlying causes of

ageing must first be identified, where the focus will be on the modes and mechanisms behind capacity fade. In this study, the cells will initially be aged with various charging rates and State of Charge (SoC) windows, after which they will be regenerated.

Electrochemical characterization will be conducted before ageing, after ageing and after regeneration. Characterization techniques include Reference Performance Tests (RPT), which is further used for the purposes of Differential Voltage Analysis (DVA) and Incremental Capacity Analysis (ICA), and Electrochemical Impedance Spectroscopy (EIS). The techniques are utilized to assess changes in capacity as well as other forms of degradation.

While the main purpose is to achieve significant capacity fade and then attempt to regenerate parts of said fade, it is also of interest to observe if there is a difference in capacity fades or forms of degradation between cells cycled at difference charging rates or SoC windows. Furthermore, another interesting aspect is whether a generic capacity regeneration method is viable, or if it needs to be tuned to the individual cell chemistries and underlying degradation mechanisms.

1.2 Limitations

The thesis will focus on an initial understanding of different parameters that affects the commercial LIB cells' performances. The framework of the thesis will focus on developing a fundamental understanding of the effect of various regeneration approaches on the capacity of LIB cells.

Nine cells were available, where one cell is kept as reference and eight cells were cycled, and three regenerated afterwards. Since the number of cells is restricted, and not significant from a statistical point of view, it infers an uncertainty to the study. Furthermore, there was no time, or enough cells, to repeat any of the experiments in an attempt to verify any observations made.

The ageing of the cells was carried out using two different charge current rates and a small difference in SoC window with the purpose of accelerating ageing. Other operational or extrinsic parameters was not considered, although they might still have a large impact on cells. Again, this is a consequence of the limited time and cells. In regards to the regeneration, while three approaches were evaluated only a few degradation mechanisms and modes, which were deemed most relevant during the initial literature study, were targeted in these approaches.

Lastly, the analysis performed is restricted to electrochemical measurements, no *post-mortem* analysis or material characterization was performed.

2

Background & Theory

To develop a non-invasive regenerative approach for LIBs, the first step is to comprehend the operation of the battery. After gaining knowledge regarding the mechanisms of the electrochemical cell, the causes and effect of cell ageing can be understood. This facilitates the fundamentals to develop a regenerative procedure to recover lost capacity trough irreversible cell degradation.

2.1 Lithium-Ion Batteries

A LIB is an electrochemical cell, or series of cells, that converts chemical energy into electrical energy and vice versa. The cells can be either pouch cells, cylindrical or prismatic, and the conversion of chemical energy is performed via a reversible redox reaction inside of the cell and the electrons are forced through an external circuit, thereby generating electricity. The main components of a lithium-ion cell are current collectors, electrodes, electrolyte, and separator, see Figure 2.1.

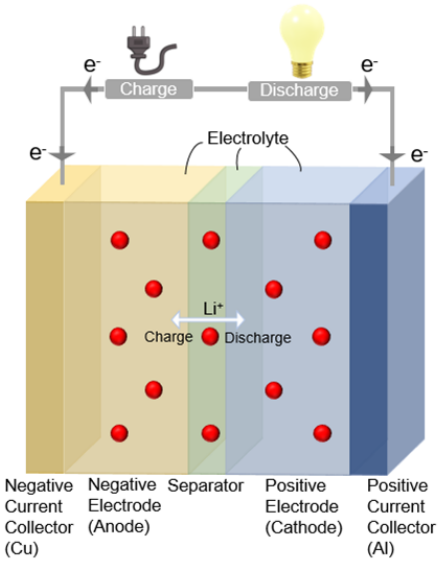

Figure 2.1: Schematic illustration of a lithium-ion battery. During discharge (charge), lithium-ions move from the anode (cathode) towards the cathode (anode).

The negative electrode, also referred to as anode, typically consists of graphite. The positive electrode, cathode, consists of a metal oxide, such as LCO (lithium cobalt oxide), LFP (lithium iron phosphate), LMO (lithium manganese oxide) or NMC (lithium nickel manganese cobalt). Since the specific capacity is generally lower for the cathode materials, more cathode material is typically used to compensate. However, it is always desirable for the negative electrode to have a slight excess of capacity as well as a geometrically oversized area to minimize the risk of lithium plating. Not only is lithium plating a severe aging mechanism, which will be discussed later on, but it is also a significant safety-deteriorating process. The relationship between the negative and positive electrode is described using the N/P-ratio and commonly ranges between 1.03 and 1.2 in commercial LIBs [11].

Each electrode also contains a binder which acts as a glue to hold the active material together and to establish a connection with the current collector, which is made of either copper or aluminum. The current collector in turn is responsible for transporting electrons between the electrodes through the external circuit. In between the electrodes there is a separator. The separator is a permeable polymer membrane with the purpose of separating the negative and positive electrode, thereby preventing a short-circuit. All cell components are submerged in the electrolyte. The electrolyte is needed to allow for ionic conduction between the electrodes and consists of a combination of organic solvents, such as ethylene carbonate and dimethyl carbonate, and a lithium salt, such as LPF (lithium hexafluorophosphate).

2.1.1 Working Principle of Lithium-Ion Cells

The principle operating mechanisms of LIBs can be compared to a "rocking chair", where lithium-ions are moving back and forth between the two electrodes driven by their different potentials. During discharge, lithium-ions deintercalate from the negative electrode, see Equation 2.1, and move towards the positive electrode where they intercalate, see Equation 2.2 where M_yO_z represents the cathode transition metal oxide.

$$Li_xC_6 \rightarrow C_6 + {Li_x}^+ + xe^- \tag{2.1}$$

$${Li_x}^+ + xe^- + Li_{1-x}M_yO_z \rightarrow LiM_xO_z \tag{2.2}$$

Intercalation refers to the process in which lithium ions are reversibly inserted into vacant sites in the crystal lattice of the electrode material, and as such the rate of intercalation depends on the diffusion rate [12]. During intercalation, lithium-ions will stack themselves to minimize the system's total energy, creating different structural compositions throughout a cycle. The different structures are represented by four graphite stages as illustrated in Figure 2.2.

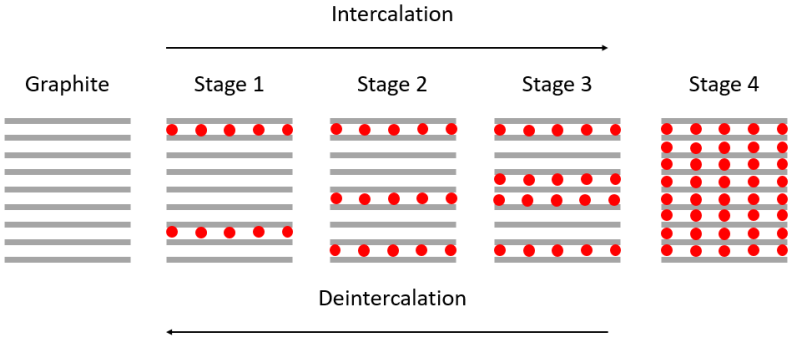

Figure 2.2: Schematic figure illustrating the different lithium-ion intercalation and deintercaltion stages of graphite.

Furthermore, since intercalation depends on the number of vacant sites in the crystal lattice, different material compositions will be able to host a varying amount of lithium. Commonly reported electrode material and their structure, theoretical and experimental capacity is presented in Table 2.1. The commercialized cathode structures are all compounds including transition-metal oxides with either layered, spinel or olivine structures [13]. Note that the experimental capacity below differs significantly from the theoretical due to factors such as material composition and phase transitions related to redox-reactions and lithium deficiencies. As for the anode material, the most commonly used is graphite. Another interesting anode material is silicon, as the theoretical specific capacity is almost ten times higher compared to graphite. However, silicon is still not a viable commercial alternative, mainly due to the significant volume increase of up to 300 % during lithiation. The massive increase in volume during lithiation causes significant mechanical stress upon the electrode and cell which reduces cycle stability [14]. While a pure silicon anode is not yet feasible, integration of silicon into a graphite anode compound is an interesting compromise which have reached the commercial market.

Table 2.1: Structure and specific capacity for different cathode and anode materials [15–18].

	Material	Structure	Theoretical Capacity	Experimental Capacity
Cathode	LCO	Layered	274 mAh/g	140-148 mAh/g
	LFP	Olivine	170 mAh/g	160-165 mAh/g
	LMO	Spinel	148 mAh/g	120 mAh/g
	NMC	Layered	280 mAh/g	160-200 mAh/g
Anode	Graphite	Layered	372 mAh/g	360 mAh/g
	Silicon	-	3590 mAh/g	-

Since the electrons move much faster than the lithium ions, the electron will arrive at the cathode and reduce the metal oxide, which will then incorporate a lithium ion from the surrounding electrolyte to compensate for the negative charge. At the same time in the anode, the corresponding lithium ion will deintercalate and start

diffuse towards the cathode to charge-compensate for the ion which was taken from the electrolyte. This results in a concentration polarization across the battery.

To achieve a current net flow across a battery an overpotential, η, is needed. The overpotential represents the deviation from the equilibrium potential and depends largely on the internal resistance of the battery [19]. It can be described as the difference between the positive electrode potential and the negative electrode potential. For a galvanic cell, the existence of overpotentials essentially means more energy is lost than predicted by thermodynamics, and will lead to further changes in the voltage during cycling. The most prominent causes of overpotential include solid-state diffusion and migration of lithium ions inside electrodes and the electrolyte, charge transfer reactions at the interfaces as well as the electronic conduction in the electrodes and current collectors [20].

2.1.2 Internal Resistance

The battery's internal resistance comprises all factors relevant to hamper the movement of ions between electrodes and causes the terminal voltage to differ from the Open-Circuit Voltage (OCV) [21]. In complex electrochemical systems, as a LIB, the internal resistance is attributed to a contribution of multiple factors, such as complex transport phenomena, electrochemical processes, and microstructures. Furthermore, the internal resistance is directly affected by operational parameters, such as the battery's SoC and temperature, and has a direct impact on the characteristics of the battery, *e.g.* capacity and working voltage [22].

Simplified, the internal resistance can be split into two categories: ohmic resistance and dynamic polarization resistance. The ohmic resistance is a result of the material resistance, originating from the electrodes, electrolyte, separator and current collector along with the contact resistance between the different components. The polarization resistance encompasses all types of resistance generated from polarization, such as activation polarization and concentration polarization [23].

There are different ways of quantifying the internal resistance. The two methods used in this study are: the use of direct current (DC) pulse signals such as pulse current tests and using alternating current (AC) signals, *i.e.* EIS. Both of these current signal methods and their use are discussed further on in the report.

Figure 2.3 illustrates an example of the voltage drop caused by a DC discharge pulse. Several phenomena are incorporated in the ohmic and polarization resistance, each governed by its respective timescale, and contribute to the voltage drop.

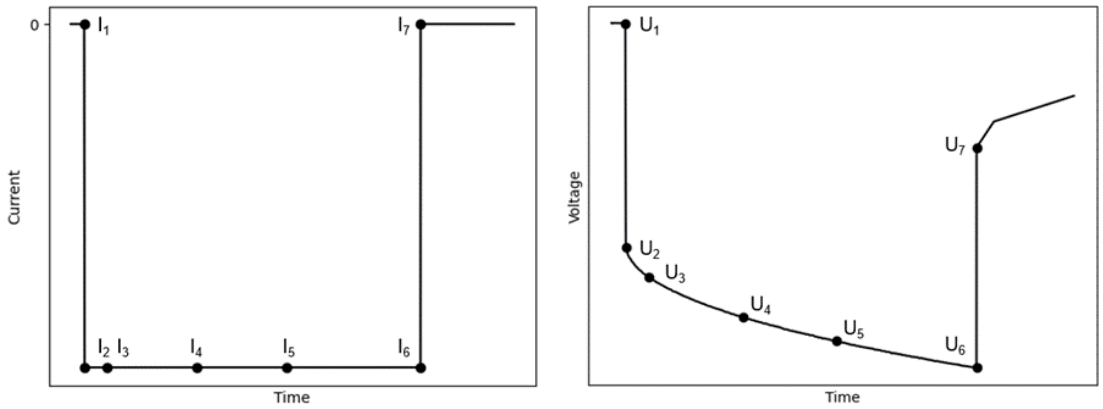

(a) (b)

Figure 2.3: Current [A] (a) and voltage [V] (b) response profile against time for a lithium-ion cell during a discharge current pulse.

Firstly, the instantaneous voltage drop occurring between U_1 and U_2 is primarily attributed to the pure ohmic resistance of the cell. Secondly, within the first seconds of discharge, the drop between t_2 and t_3 is attributed to the cell's double layer capacitance and charge transfer resistance and is hence associated with the charge transfer reactions taking place at the interface between the electrode and electrolyte. Finally, the more gradual, close to linear voltage drop, observable between U_5 and U_7, can be attributed to the polarization resistance. This resistance originates from the ionic diffusion and is often regarded as the rate-determining step for LIBs.

By comprehending these various resistances, an intuitive understanding of the underlying electrochemical processes of the cell and how they evolve over the course of its lifetime can be gained. [22].

The ohmic resistance is calculated instantaneously at the start of the pulse, according to Equation 2.3, using the current I_2 as I_1 will be equal to zero.

$$R_{ohm} \approx \frac{U_2 - U_1}{I_2} \tag{2.3}$$

In contrast to the ohmic resistance, the step resistance at Δt includes contributions from both the ohmic resistance, the reaction kinetics and polarization up until Δt. The choice of Δt was set between two and 30 seconds.

$$
\begin{aligned}
R_{2s} &= \frac{U_3 - U_1}{I_3} \\
R_{10s} &= \frac{U_4 - U_1}{I_4} \\
R_{18s} &= \frac{U_5 - U_1}{I_5} \\
R_{30s} &= \frac{U_6 - U_1}{I_6}
\end{aligned}
\tag{2.4}
$$

The same equivalent equations can be applied for both charge, discharge, and rest pulses.

2.1.3 Cell Degradation - Ageing & Ageing Mechanisms

As battery cells are cycled, they experience continuous deterioration due to both the passage of time and usage. Hence cell degradation is an inevitable phenomena. Cell degradation originates from generally irreversible reactions arising inside the cell, including various undesirable chemical and mechanical reactions. Accompanied by a reduction in available energy and power, these side reactions are associated with an internal resistance rise and capacity loss. Cell capacity quantifies the total amount of electrical charges that can be stored in the cell. Comparatively, internal resistance is related to how quickly the stored energy can be delivered, i.e., the cell power. Therefore SoH is a metric typically used to quantify the degradation in cell performance. SoH is parameterized in terms of both cell capacity and internal resistance. Accordingly, the battery's lifespan is conventionally considered to reach its end, known as the EoL, when the capacity drops to around 80 % of its initial beginning-of-life (BoL) value or when the internal resistance increases to 200 % of the BoL value [24, 25].

The battery ageing is unavoidable, whether the battery is in operation or not. The type of ageing is divided into cycle ageing and calendar ageing, respectively. Calendar ageing is defined as the irreversible fraction of the capacity lost during storage and is hence highly determined by the storage conditions [26]. In contrast to calendar ageing, cycle aging occurs during either charge or discharge, and therefore is a direct consequence of the utilization mode and operational conditions. The utilization mode of a battery in an EV, would for example include how the vehicle stops at red light and accelerates afterwards. Consequently, many factors are involved with this type of ageing. Additionally, as the battery aging is directly linked to the utilization mode, capacity decrease and power fading do not originate from one single source, but several processes and interactions.

2.1.3.1 Cell Capacity Fading, Causes & Effects

The overall total capacity and power fade observed in ageing LIB cells are attributed to various degradation mechanisms occurring in multiple different cell components.

These mechanisms include degradation of the current collectors, electrodes, electrolyte, and separator, all occurring simultaneously and intertwined. They contribute to a loss of both cyclable lithium and active material in the electrodes, and a variety of other degradation mechanisms. Since the degradation often lead to similar effects regarding the physical properties of the cell, rather than individual distinct ageing effects, it is possible to categorize them into several degradation modes based on their shared characteristics. The generally acknowledged degradation modes are [25, 27, 28]:

1. Loss of Lithium Inventory (LLI). LLI is associated with the consumption of lithium-ions caused party by parasitic side reactions. For LIBs with a graphite anode, LLI mainly arises form the formation and growth of the Solid Electrolyte Interface (SEI) between the negative electrode surface and electrolyte, electrolyte decomposition reactions and lithium plating. These reactions irreversibly consume lithium-ions, thereby contributing to the capacity fade of the cell. Furthermore, lithium plating can also lose it's electrical connection and become isolated, which will be discussed further on in the report.

2. Loss of Active Material at the Negative Electrode ($\mathrm{LAM_{NE}}$). $\mathrm{LAM_{NE}}$ indicates that active material related to the negative electrode has become inaccessible for lithiation, due to e.g. cracking of the active material, active sites being blocked by resistive surface layers as well as the active material losing its electrical contact. Consequently, these processes causing $\mathrm{LAM_{NE}}$ can result in both capacity and power fade of the cell.

3. Loss of Active Material at the Positive Electrode ($\mathrm{LAM_{PE}}$). $\mathrm{LAM_{PE}}$ indicates that active material related to the positive electrode has become inaccessible for lithiation, due to e.g. cracking of the active material, the active material losing electrical contact and structural disordering. Additionally, $\mathrm{LAM_{PE}}$ can be caused by material loss related to, for instance, metal dissolution. Consequently, these processes causing $\mathrm{LAM_{PE}}$ can result in both capacity and power fade of the cell.

The cause and effect of each degradation mechanism relates to individual but often integrated factors, such as different environmental circumstances (*e.g.* temperature and mechanical stress), operational parameters (*e.g.* SoC during operation and current) and battery chemistry. As the behavior of the cell follows the Arrhenius equation, all reaction rates are directly correlated to the temperature [29]. Furthermore, the viscosity of the electrolyte is temperature dependent, which affects the diffusivity, and as a result also impacts the ion conductivity and charge transfer resistivity [30]. The SoC corresponds to the concentration of ions in the electrodes, directly translating to the potential difference between the electrode and electrolyte interface. As a result, the energy barrier and activation energy is affected, thus potentially promoting side reactions, and parasitic reactions, further ageing the battery [26]. Some of the typically proclaimed causes behind LIB cell degradation mechanisms include [25, 31]:

- Temperature: Low temperatures lowers the ionic conductivity and hinders

the kinetics of lithium-ions. As a result, the migrating lithium-ions become entrapped in the graphite layers during intercalation, where the reduced conductivity of the graphite and SEI retards the ion transfer. Due to the charge accumulation, lithium may precipitate from the electrolyte and deposit on the electrode surface. The occurrence of lithium deposition is facilitated by the fact that the potential of lithium deposition is close to that of the graphite anode. The proximity of the two potentials becomes magnified when the lithium intercalation kinetics are hampered, *i.e.*, during low operation temperatures, leading to LLI by forming plated lithium. The highly reactive deposited lithium can undergo subsequent reactions forming a new SEI film (LLI) resulting in local volume expansions, which can lead to mechanical stress and cracking during continuous cycling (LAM). Continuous growth of lithium dendrites leads to an increased risk of the separator being penetrated, causing an internal short circuit and cell failure [29]. High temperatures instead accelerate side reactions by lowering the activation barrier, including parasitic reactions such as (i) the growth rate of the SEI on the anode (resulting in LLI and increased internal resistance), (ii) electrolyte and binder decomposition and (iii) metal dissolution. LLI and LAM are both initiated by (ii) and (iii) [32–34].

- Overcharge/overdischarge: Occurs when current is applied even though the cell has reached its upper or lower voltage limit. When overcharged, the positive and negative electrode active material is over-delithiated and over-lithiated respectively. Overcharge results in (i) irreversible structural change at the positive electrode, (ii) transition metal dissolution and (iii) decomposition of active material, resulting in LAM. Moreover, an increase in internal resistance can be observed due to overcharging. Overcharging is more likely to occur at low temperatures, as the polarization effect causes the charging cut-off voltage to become prone to be exceeded [35]. When over-discharged, the negative electrode potential increases and consequently heightens the risk of corrosion of the copper (Cu) current collector (LAM), and as such Cu^{2+} ions are released into the electrode [33]. Corrosion products that exhibit poor electronic conductivity cause overpotential and favours non-homogeneous current and potential distribution, and thus, lithium plating (LLI and LAM).

- SoC: At lower SoC, and temperatures, the electrode surface exhibit a higher degree of passivation. At higher SoC the electrolyte approaches, or exceeds, its stability limit relative to both the negative and positive electrode, resulting in accelerated SEI growth (LLI). Additionally, some cathode-anode material combinations prefer certain voltage ranges, limiting the voltage window, and thereby the SoC window. As a consequence the accessible energy is limited, but it will also lengthen the overall lifetime of the cell [36, 37]. When operating in a smaller SoC window, the volume expansion of the electrode is less significant, putting the SEI under less stress meaning it stays more or less intact. Conversely, a larger SoC window intensifies the volume expansions during intercalation, thereby aggravating the stress on the electrodes (LAM, and as new SEI is formed LLI).

- High current rates: Charge and discharge can generate localized overcharge, evoking similar degradation mechanisms as during overcharge/overdischarge. As the rate of intercalation is limited, fast charging of cells with a graphite anode results in a localized overpotential. Due to the proximity of the equilibrium potential of graphite and the metallization potential of lithium-ions, the resulting larger polarization at the anode, instead causes lithium plating as intercalation becomes less energetically favorable [29]. Additionally, during charging at high current rates solvents can be forced to co-intercalate with the lithium, causing gas generation. The resulting pressure build-up can cause particle cracking and graphite exfoliation (LAM) [33]. Moreover, high current rates lead to increased cell temperature [37], due to the Ohmic resistance and polarization effect. This is a result of the friction caused by the anions as they diffuse in the opposite direction [35].

- Mechanical stresses: LIB cells are subjected to mechanical stress from multiple sources, including: (i) applied external preload from cells being packaged in constrained spaces, for instance in modules, and (ii) the volume expansion of the electrode materials during lithium intercalation and deintercalation. Carbonaceous anodes experience a 10 % volume increase during a full charge-discharge cycle. In comparison, the metal-oxide cathodes experience a 5 % increase, silicon anodes a 300 % increase and pure lithium a 100 % volume increase. The volume change can lead to cracking of the active material along the internal grain boundaries or near the separator, which for a carbonaceous anode evoke SEI formation at the newly exposed graphite. Similarly, volume changes can cause the pre-existing SEI to crack, once again exposing the anode material and resulting in SEI formation, or even contact loss between graphite particles. All-in-all, causing a significant degradation of cell performance and capacity fade [32, 38].

Figure 2.4 presents an overview of the most influential operational parameters causing the different degradation mechanisms, linking the ageing phenomena together with respective cause, degradation mode and effect. For more in-depth details regarding two commonly reported degradation mechanisms, SEI growth and electrocrystallization (lithium deposition and dissolution), see Sections 2.1.4 and 2.1.5, respectively.

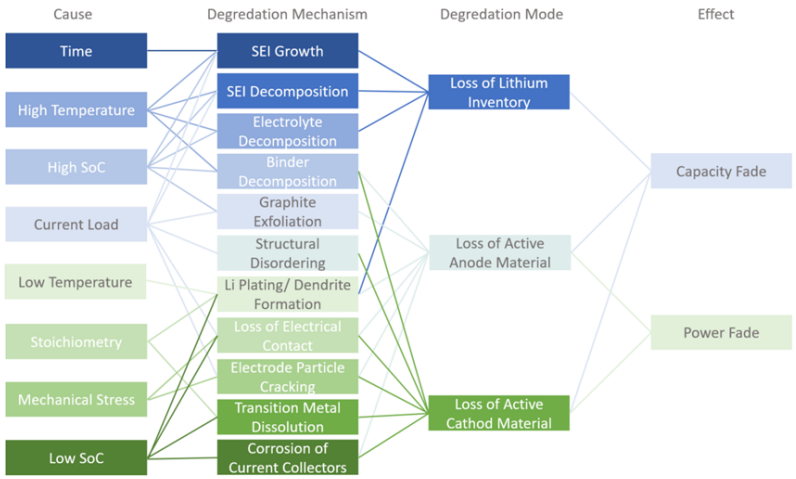

Figure 2.4: Summery over the cause and effect of LIB cell degradation mechanisms and associated degradation modes. Figure adapted from [27].

A part of the lost capacity during cell ageing can be recovered, leading to a differentiation between reversible and irreversible capacity loss. And the effect of the anode overhang largely contribute to the reversible capacity loss [39]. The anode overhang area is the small portion of the anode that extends past the opposed cathode. During extended periods of storage, lithium can diffuse into the overhang area and consequently start acting as a reservoir of active lithium. The charge and discharge, or storage and release, of the active lithium in the overhang area alters the available lithium inventory and by extension also the coulombic efficiency of the cell. [40]

2.1.4 Solid Electrolyte Interface

It is commonly acknowledged that the SEI is crucial to the performance of LIBs. The SEI is a key attribute in making the cell reversible, but also has a large impact the cell's safety [41]. While its existence is vital for stable operation of the cell, the formation and growth are complicated processes, as the chemical composition, morphology, and stability of the SEI depend on multiple different aspects.

2.1.4.1 Formation

The Open Circuit Voltage (OCV), V_{OC}, is a fundamental parameter of the cell. The OCV is defined as the potential difference between the positive and negative electrodes when no load is applied. Cell performance is contributed to the OCV, and for stable operation the OCV is constrained to lie within the stability window of the electrolyte. The stability window for operation is defined by the highest occupied molecular orbit (HOMO) and lowest unoccupied molecular orbit (LUMO) of the electrolyte. Provided a mismatch, meaning the either LUMO is lower than the anode potential (μ_a) or if the HOMO is greater than the cathode potential (μ_c), the electrolyte will be reduced or oxidized. For commercial LIB cells, the intercalation potential for lithium into the anode generally falls below the stability of the com-

monly used organic electrolytes. Hence, stable operation call for the the formation of a passivation layer between the electrolyte and the negative electrode. This is known as the SEI. Upon initial operation, the electrolyte will be reduced, forming the SEI, which becomes an ionically conductive layer while still being electronically insulating. This property is crucial for further intercalation/deintercalation during continued cycling, but simultaneously prevents further undesired decomposition of the electrolyte (LLI). Nonetheless, during the first full cycle, 10 % of the original capacity is typically consumed in the irreversible formation of the SEI, and this addition of a passivasion layer will affect the ion permeability during lithiation, resulting in an increased internal resistance [32, 41].

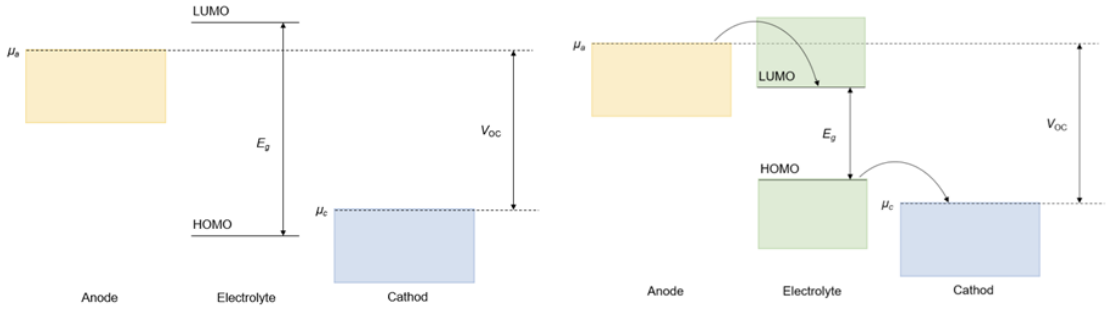

Figure 2.5: Schematic molecular orbital diagram of a LIB cell, illustrating two cases of when the anode and cathode electrochemical potentials (μ_a, μ_c) lie either: (a) within the stability window of the electrolyte or (b) outside the stability window of the electrolyte, where in the case of (b) passivation layers will form (*e.g.* the SEI).

2.1.4.2 SEI Growth as a Degradation Mechanism

During continuous intercalation and deintercalation, the SEI must withstand expansion and contraction although maintaining thin enough not to be too resistive. However, it will gradually thicken during repeated cycling due to continuous electrochemical reduction of the electrolyte. The gradual, and non-uniform, thickening further lowers the cells capacity due to the continued consumption of lithium-ions (LLI) as well as increased internal resistance. Several operational parameters affect and accelerate the SEI growth, such as high temperature and mechanical stress, which can result in cracks and exfoliation of the anode [27].

2.1.5 Electrocrystallization - Lithium Deposition & Depletion

For LIBs operating under normal working conditions, the intercalation/deintercalation is reversible. However, under very severe operational conditions, such as charging at low temperatures or when overcharging the cell, the lithium-ions can be reduced to metallic lithium and deposit throughout the cell. This phenomena is called electrocrystallization and describes the process of crystallization caused by

mass transfer accompanied by charge transfer. It is one of the most severe ageing mechanisms in LIBs.

2.1.5.1 Formation & Deposition

The impelling cause for electrocrystallization is the overpotential in the cell, *i.e.* the deviation of the electrode potential from the OCV. At potentials higher than the OCV, the overpotential becomes negative, and electrodeposition of metals becomes facilitated [42]. In a LIB, electrodeposition generally occurs when the anode surface potentials falls below the potential of Li/Li^+. In this instance, lithium deposition forming lithium metal is more thermodynamically favorable than the lithium ions being intercalated. Moreover, different non-uniformities, such as crystal orientation, or factors causing low diffusivity or slowed down intercalation kinetics (temperature and the properties of the electrolyte), will restrain the ion transport. The hindered kinetics results in locally induced overpotentials, causing lithium to become plated [43].

The final microstructure of the electrodeposited metal is determined by multiple different factors and processes. Consequently, the deposited lithium form several different surface morphologies. Commonly reported lithium morphologies include dendritic (needle-like), moss-like, and particulate (granular) deposits. In order for lithium to become plated, compact, sooth and adherent deposits are needed which are typically favored by a low overpotential. Consequently, low voltage anodes will experience lithium plating to a higher degree than high voltage anodes. Graphite anodes have a small reversible potential compared to Li/Li^+, accounting for the large occurrence of lithium-plating [44].

For LIBs, lithium deposition, but also dissolution, is an inherent process at the anode interface during normal cycling. When the anode potential rises above Li/Li^+, which usually happens at the end of either charge or discharge, a portion of the plated lithium gets dissolved and returns to the electrode. Therefore, lithium plating is partly a reversible process as long the electrical connection between the deposited lithium and the anode active material is maintained [45, 46].

2.1.5.2 Dead & Isolated Lithium

As previously mentioned, lithium can deposit non-uniformly, most commonly forming structures either in a mossy-like or a needle-like manner. Quick growth of these microstructures have severe safety hazard implications, as they can cause thermal runway and even short-circuiting the cell. Upon discharge, the plating can be stripped, which in turn can cause the unstable structures to collapse. These collapsed structures constitute the irreversible plating, and will react with the surrounding electrolyte, causing them to be encapsulated by a SEI layer (LAM and LLI), rendering them fully disconnected from the current collector [44]. As the lithium metal has lost its electrical connection, it can no longer participate in the lithiation, and as such they are referred to as dead or isolated lithium (i-Li). Note that i-Li is not only generated during stripping, but can also occur during plating as a consequence of the fast SEI formation, which can cut the connection to the current

collector. A simplified schematic of the formation is illustrated in Figure 2.6. While this behavior is most prominent in batteries with a lithium metal anode, it can also be an issue in graphite anode LIBs during fast- and over-charging [10].

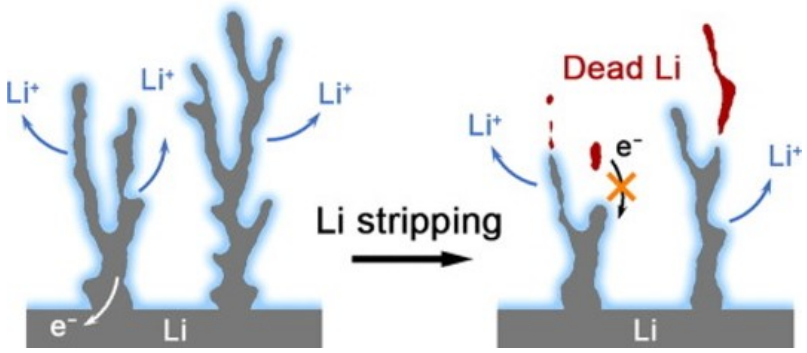

Figure 2.6: Schematic illustration of the formation of dead-Li during the process of lithium stripping. The illustration is adapted from [47].

2.2 Regeneration

In this work, the term regeneration is defined as the recovery or restoration of capacity with the purpose of extending the effective lifespan of battery cells. When speaking of battery cells, regeneration should be distinguished from recycling. In literature, these are sometimes used synonymously, or in a way where the processes depends on one another. These are often methods of recycling battery materials [48] or proposing a method relying on disassembly of the battery as an *ex-situ* regeneration technique [49, 50]. *Jin et al.* presents a lithium restoration method based on iodine redox chemistry that can effectively rejuvenate electrochemically inactive lithium in both the SEI and i-Li [9]. Utilizing the chemical composition of the electrolyte and the SEI, the authors found that introducing iodine into the electrolyte gave rise to beneficial electrochemistry in the cell, resulting in continuous spontaneous redox reactions removing and redepositing lithium from the inactive lithium in the SEI to the cathode. Though this method presents an *in-situ* chemical rejuvenation method, it is constructed for a specific cell chemistry. This motivates the search for a more general procedure, which can later be adapted to different cell types and chemistries.

2.2.1 Electrical Pulse Techniques

The lead-acid battery is one of the earliest generation of rechargeable batteries used in EVs. Compared to LIBs, the lead-acid batteries are cheaper but has a relatively low energy density. The main components of a lead–acid battery are the two electrodes (or plates) submerged in the electrolyte comprised of a combination of sulphuric acid (H_2SO_4) and water, with a plate separator in between the electrodes. The anode is made of metallic lead (Pb) and the cathode is made of lead dioxide (PbO_2).

Occasionally fragments of crystallized lead sulfate remains on the plates after cycling, commonly referred to as sulfation. Over time, these crystals harden and even become chemically inactive.Consequently, the battery's capacity reduces due to the loss of active material. [6]. This phenomenon arises naturally throughout cycling. However, during certain conditions, such as prolonged charged deprivation, sulfation is more prominent [51, 52].

A potential approach to counteract the impact of sulfation involves utilizing current pulses. Various pulse-charging systems and patents are currently available in the market for this purpose. Two significant benefits have been found with the pulse current technique, namely a reduction in charge time and an increase in cycle life. Pulse technology presents a viable approach for addressing sulfation in lead-acid batteries, as it offers the potential to dissolve the crystals and restore the sulfates. By carefully introducing controlled DC pulses into the battery (focusing on rise time, pulse width, frequency, and waveform shape), the sulfates are liberated from the crystal formations, enabling them to once again participate as active electrolyte components. The pulses allow for a small energy input, just enough to individually energize the molecules to dissolve and liquefy the crystals whilst not damaging the battery [53].

Another way to reverse the sulfation process is to send electrical pulses at the resonance frequency (3.26 MHz) of the crystals. During this process, the crystals starts to vibrate, and the sulphur ions collide with the plates which have the effect of dissolving the lead sulphate covering them [52, 54, 55].

Pulse technology has been further extended to lithium-ion battery technology. Generally, the pulsed current is implemented as charging strategies to reduce the charging time [56–58]. Pulsed technology has also proven to have impact on the lifetime and temperature rising of lithium-ion batteries [59–62] or as a mean to control electrodeposition and SEI formation [63], and as an operation to stabilize the future grids [64]. Motivated by the promising results of implementing pulse-technology in LIBs and the success of desulfation using pulses in lead-acid batteries, perhaps a similar technique can be proposed to regenerate LIBs.

2.2.2 Recovery of Dead Lithium

Another interesting possibility for capacity regeneration is to recover i-Li. *Liu et al.* has proved that i-Li remains responsive to electrochemical processes [10]. Even though the i-Li has lost contact with the current collectors it is still responsive to the electromagnetic field present across the electrolyte. The charge distribution over the i-Li will be altered dependingly, resulting in polarization. The positive/negative charges will accumulate and eventually distort the i-Li/electrolyte interface equilibrium. The resulting overpotential, η, can be described as,

$$\eta = \Phi_{\mathrm{Li}} - \Phi_{\mathrm{I}} - E_{\mathrm{eq}} \tag{2.5}$$

where Φ_{Li} is the electric potential of lithium, Φ_{I} is the electrolyte potential and E_{eq} is the potential of lithium deposition/dissolution.

Upon discharge the electric potential gradient points from the negative electrode towards the positive electrode. The dynamic polarization of the i-Li will result in a negative overpotential, and thereby lithium deposition at the end closest to the negative electrode, and a positive overpotential, and lithium dissolution at the end closest to the positive electrode. The result will be a dynamic spatial progression towards the negative electrode during discharge, see Figure 2.7. The reverse is true during charge.

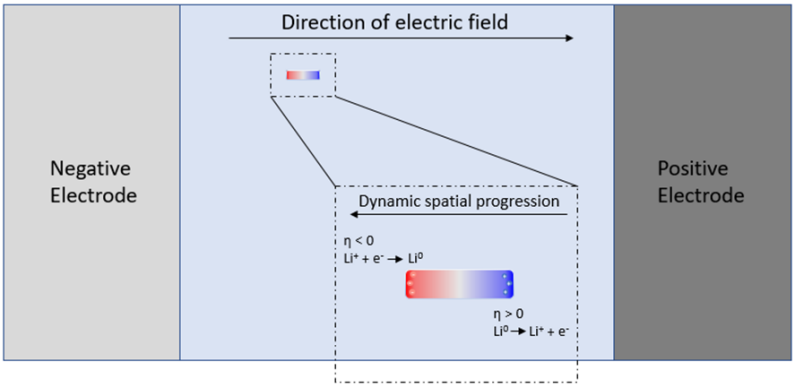

Figure 2.7: Schematic illustration of the i-Li in a LIB during discharge. The electric potential gradient gives rise to an electric field pointing towards the positive electrode. The surface of the i-Li will screen and respond to the electric field, resulting in a negative overpotential at the end closest to the negative electrode and positive overpotential at the end closest to the positive electrode. The consequence will be a dynamic spatial progression of i-Li towards the negative electrode. Image adapted from [10].

2.3 Differential Voltage Analysis & Incremental Capacity Analysis

Differential Voltage Analysis (DVA) and Incremental Capacity Analysis (ICA) are non-destructive techniques used for capacity estimation and investigation of cell degradation. A quantitative correlation between the Differential Voltage (DV) and Incremental Capacity (IC) peaks to the capacity fade can be observed for SoH monitoring [28].

DVA and ICA works by transforming the cell voltage plateaus into identifiable $\frac{\mathrm{d}Q}{\mathrm{d}V}$ and $\frac{\mathrm{d}V}{\mathrm{d}Q}$ peaks, respectively. The plateaus, likewise the peaks, portray the underlying cell phase transition characteristics during the intercalation/deintercalation in the electrodes. As illustrated in Figure 2.8, the voltage can be seen as a monotonously increasing function of the capacity. At the end of the voltage curve, it decreases (or increases) rapidly. Each peak appearing in the IC curve corresponds to one voltage plateau, therefore representing the process of phase transformation. The same process is true for a DV curve [28, 65, 66].

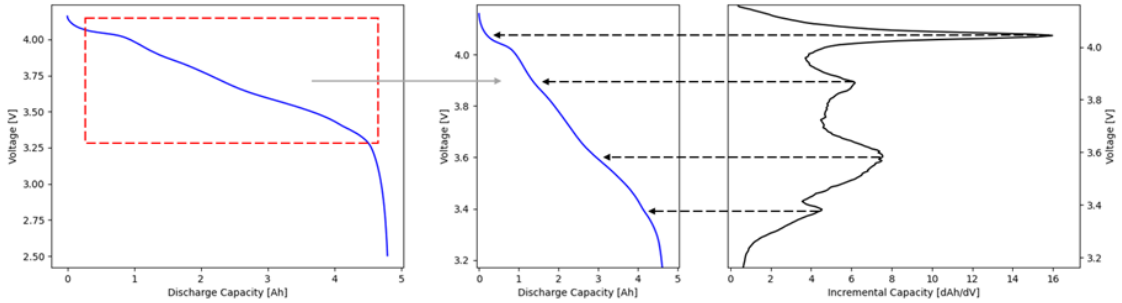

Figure 2.8: The OCV and IC curve of a full (NMC/Si-G) cell during discharge, highlighting the correlation between peaks in the IC curve and plateaus in the OCV. Figure adapted from [65].

Mathematically, the IC curve is defined as the gradient of the capacity (Q) with respect to displacement of the cell voltage (V). The DV curve is defined as the inverse on the IC. This is presented in Equation 2.6,

$$\begin{aligned} \frac{\mathrm{d}Q}{\mathrm{d}V} &= \frac{\Delta Q}{\Delta V}, \\ \frac{\mathrm{d}V}{\mathrm{d}Q} &= \frac{\Delta V}{\Delta Q} \end{aligned} \tag{2.6}$$

for the ICA and DVA respectively. Moreover, the DV for the cell represents a linear superposition of the derivative of the anode and cathode potential [66, 67].

$$\begin{aligned} V_{\text{cell}} &= V_{\text{cathode}} - V_{\text{andode}} \\ \frac{\mathrm{d}V_{\text{cell}}}{\mathrm{d}Q} &= \frac{\mathrm{d}V_{\text{cathode}}}{\mathrm{d}Q} - \frac{\mathrm{d}V_{\text{anode}}}{\mathrm{d}Q} \end{aligned} \tag{2.7}$$

In ageing studies, DVA is utilized to separate different ageing modes, such as anode and cathode degradation, possible due to the relationship between the electrodes, as seen in Equation 2.7. Generally, half-cells are built in order to identify which resulting peaks in the full cell differential voltage that are contributed to which electrode [67].

As batteries age, peak shifts, and variations in height and width, can be observed due to the influence of increased resistance and polarization. Furthermore, using DVA and ICA, both LLI and LAM can be evaluated by analyzing how the peaks in the IC and DV curves shift throughout the cell's lifetime [66]. An overview of the DVA and ICA related to LIB ageing is summarized in Table 2.3, highlighting the most prominent degradation modes, mechanisms and final effects in terms of Power Fade (PF) and Capacity Fade (CF).

Table 2.2: Relationship between the changes in the IC-DV curves and the most pertinent degradation modes, potential degradation mechanisms and most prominent observed effects [31].

Change in IC Curve	Change in DV Curve	Most Prominent Degredation Mode	Potential Degredation Mechanism	Most Prominent Effect
Shifting towards lower voltages	No change	Conductivity Loss (CL)	CC corrosion	PF
			Binder decomposition	CF
Decrease in peak height and shift towards lower voltages	Shifting towards lower capacities	LLI	Electrolyte decomposition	CF PF
			Lithium plating	CF PF
			Solvent co-intercalation	CF PF
Decrease in peak height at approximately constant voltage	Decrease in valley depth at approximately constant capacity	LAM	Electrolyte decomposition	CF PF
			Crystal structure disordering	CF PF
			Transition metal dissolution	PF
			Solvent co-intercalation	CF PF

2.4 Elecrochemical Impedance Spectroscopy

EIS is a non-invasive electrochemical characterization method where an AC potential is usually applied over a range of frequencies and the current response is measured. Using this information the impedance can be determined, which is a measure of the opposition to electrical flow.

As presented by *Dillmann et al.* [68], the applied potential can be described as:

$$E_{\mathrm{t}} = E_0 \sin(\omega t) \tag{2.8}$$

where E_{t} is the potential at a given time, E_0 is the amplitude and ω is the frequency in radians. The current response out of the system can in turn be described as:

$$I_{\mathrm{t}} = I_0 \sin(\omega t + \phi) \tag{2.9}$$

where ϕ represents the phase shift. The impedance can now be described in a manner similar to the resistance in Ohm's law:

$$Z = \frac{E_{\mathrm{t}}}{I_{\mathrm{t}}} = \frac{E_0 \sin(\omega t)}{I_0 \sin(\omega t + \phi)} = Z_0 \frac{\sin(\omega t)}{\sin(\omega t + \phi)} \tag{2.10}$$

As shown in Equation 2.10, the impedance can be expressed as an amplitude, Z_0, and a phase shift, ϕ. Furthermore, utilizing Euler's formula the impedance can also divided into a real and imaginary part.

The impedance is usually presented in a Bode plot or a Nyquist plot. The Bode plot shows both amplitude and phase shift plotted against frequency and is often separated into two graphs. The Nyquist plot instead show the real part of the impedance ($Z^{'}$) on the x-axis and the imaginary part of the impedance ($Z^{''}$) on the y-axis.

To analyse EIS data from battery cells, an Equivalent Circuit Model (ECM) is fitted to the data. The ECM is a model which describes the electrochemical system of a battery in terms of a circuit [69]. The ECM can predict the macroscopic physical parameters accurately and simulate the important macroscopic physical quantity distribution of the battery. Therefore, it is very suitable to realize the optimization design and safety analysis of LIBs.

The elementary components used in an ECM are resistors, capacitors, and inductors. When the potential is applied across a capacitor the voltage will lag behind the current, and for an inductor it will lead the current. This translates to a phase shift of $-\frac{\pi}{2}$ and $+\frac{\pi}{2}$ for the capacitor and inductor respectively. The impedance of each component can be seen in Equations 2.11-2.13 respectively:

$$Z_{\mathrm{res}} = R, \tag{2.11}$$

$$Z_{\mathrm{cap}} = -\frac{j}{\omega C}, \tag{2.12}$$

$$Z_{\mathrm{res}} = j\omega L \tag{2.13}$$

where R is the resistance, C is the capacitance, L is the inductance and j is the imaginary unit [70]. Since the capacitance is the interesting factor for the most part, the y-axis of the plots is usually inverted.

However, electrode surfaces in batteries do not behave as ideal capacitors. Therefore another element is commonly used, the Constant Phase Element (CPE), to model the capacitive behaviour:

$$Z_{\mathrm{CPE}} = \frac{1}{(j\omega)^{\alpha} Q} \tag{2.14}$$

where Q is the capacitive-like element and α is the CPE exponent which ranges from 0 to 1. When α is equal to one, the CPE behaves like an ideal capacitor, and when it is equal to zero it behaves like a resistor [71].

EIS is commonly employed when analysing ageing phenomena happening in LIBs. A study by *Pastor-Fernández et al.* found a correlation between Ohmic resistance and Conductivity Loss (CL), as well as between charge transfer/SEI resistance and LLI, see Table 2.3.

Table 2.3: The correlation between resistance increases in different ECM components and degradation modes.

ECM component	Most Prominent Degradation Mode	Potential Degradation Mechanism
Increase in R_{Ohm} [Ω]	CL	CC corrosion
		Binder decomposition
Increase in RCT/SEI [Ω]	LLI	Electrolyte decomposition
		Lithium plating
		Solvent co-intercalation

However, a study by *Schindler et al.* states that while increased SEI resistance is likely mainly due to LLI, an increase in both charge transfer resistance and ohmic resistance can be a result of both LLI and LAM. It is clear that further studies are needed to assess which degradation mode is the domineering for each ECM component, as well as how different cell chemistries and ageing aspects affect them.

3

Methods

The experimental work behind this thesis is divided into four main parts: initial characterization of the cells, ageing, regeneration, and electrochemical analysis. An outline of the experimental work is presented in Figure 3.1. One cell is kept as a reference, whilst the rest were aged, and then either regenerated or stored.

To understand how different parameters influence the ageing and affect regeneration, electrochemical tests are executed at three different stages of the cell lifetime: beginning-of-life, after cycling, and after regeneration. The electrochemical characterization include Reference Performance Testing (RPT) and EIS, as well as an additional formation test for the reference cell.

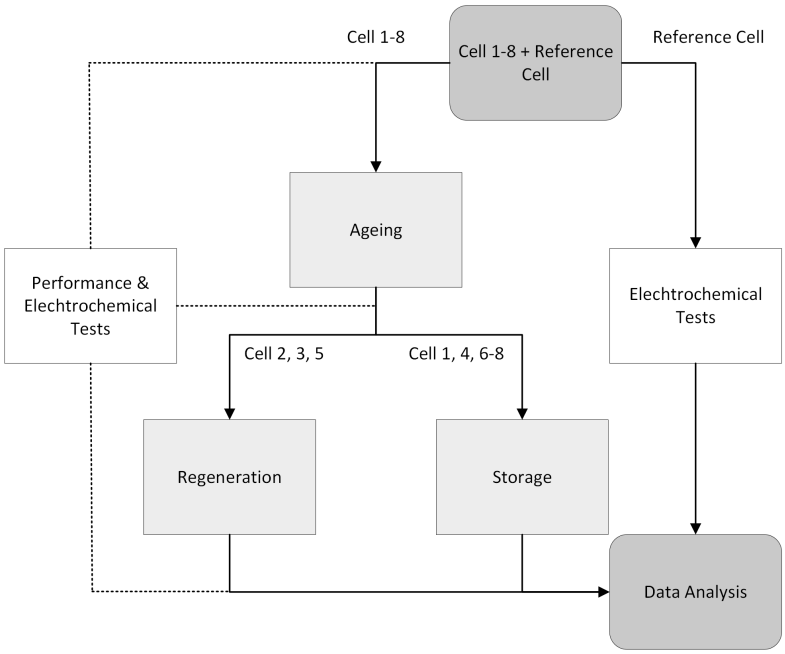

Figure 3.1: Flowchart illustrating the main parts of the experimental procedure.

Additional details regarding the experimental procedures, parameters of ageing and regeneration, as well as the operational conditions and procedures for conducting electrochemical characterizattion are presented in the subsequent sections below.

3.1 Materiel & Test Setup

All nine test cells used throughout the experiments are cylindrical rechargeable LIBs made by a commercial vendor of cell model LG INR21700M50LT. The nominal specifications of the cells are presented in Table 3.1. The cell chemistry and composition are not provided by the manufacturer, and hence unknown.

Table 3.1: Nominal specifications for cell type LG INR21700M50LT.

Item	Note	Specification
Energy	By standard charge/discharge	Nom. 18.2 Wh Min. 17.6 Wh
Max. charge voltage		4.20 V
Max. charge current	25 ~ 45°C (Atmosphere)	0.7 C (3.360 mA)
Min. discharge voltage		2.50 V
Max. discharge current	25 ~ 55°C (Atmosphere)	1.5 C (7.200 mA)
Weight		68.2 ±1.0 g

The cells were attached to cell holders, which were then connected to either a MACCOR or PEC battery tester, see Figure 3.2. A thermocouple of type K was used to observe the temperature throughout the experiments for all cells.

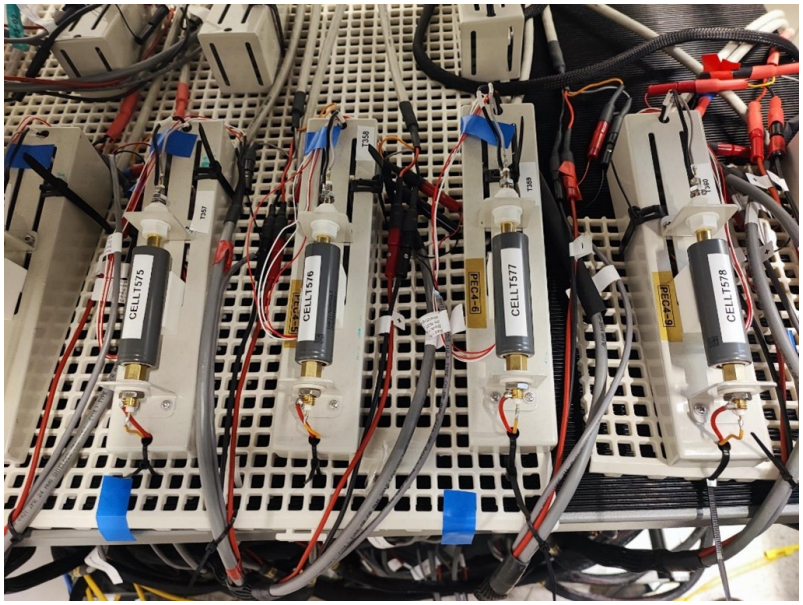

Figure 3.2: The experimental setup for cells 1-4 (left to right) on a PEC battery tester. The names in the image is used for internal cell identification.

3.2 Experimental Procedures

The experimental procedures include a formation test, RPTs, different ageing procedures, and three different regeneration procedures, all described below. All procedures were performed using MACCOR and PEC battery testers. During all procedures the current, voltage, capacity, energy time and temperature were recorded for the cells.

3.2.1 Formation Test

To evaluate if the cells had formed an SEI layer before arrival, a formation test was performed on the reference cell. By recording the charge and discharge cell capacity during its initial cycles, conclusions can be drawn regarding if the cell has formed an SEI or not. The formation test included 4 full 0.33C charge and 0.5C discharge cycles between the cell $V_{\text{max}} = 4.2$ V and $V_{\text{min}} = 2.5$ V.

3.2.2 Reference Performance Test

The RPT serves as a comprehensive evaluation method aimed at quantifying not only the capacity of the cells, but also the resistance, thereby capturing the effects of cell ageing and regeneration.

One RPT was performed before cycle ageing started, as a initial reference to the BoL of the cells. Additionally, one RPT was performed after cycling, and after regeneration to evaluate the ageing and regeneration procedures.

In summary, the RPT contains three major steps highlighted in Figure 3.3: First is an initial discharge to 0 % SoC, (1) followed by a fast charge-discharge cycle using a current rate of 0.33C, (2) a slower charge-discharge cycle using a current rate of 0.1C, and (3) a final SoC-adjustment comprised of an incremental 20 % SoC increase and decrease between levels of 20 %, 40 %, 60 % and 80 % SoC. For continuity, the 0.1C discharge capacity measured after cycle 2 was set as the reference capacity value. To mitigate the impact of heat generation, appropriate intervals of rest were incorporated between charge and discharge to allow the cells to cool down. This strategy aimed to minimize the extent to which heat influenced the overall capacity of the cells.

Following the initial two cycles, a series of DC pulse tests were performed. For every increment of 20 % SoC, the cell response to a 1C 30 seconds long charge/discharge pulse was recorded. The objective of the hybrid pulse power characterization test was to measure the dynamic cell response at different SoC, which is related to the cell's kinetic performance.

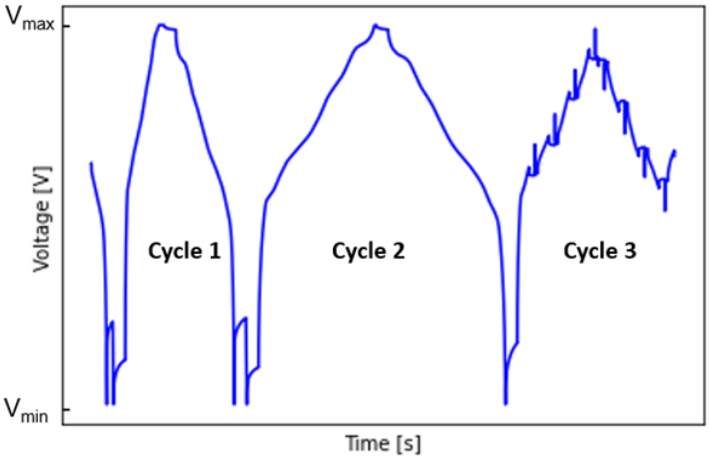

Figure 3.3: Voltage profile for a lithium-ion cell during the RPT. The three main components of the test are marked as cycle one, two and three, which represent a faster and slower charge/discharge cycle followed by incremental SoC adjustment with included DC pulses.

3.2.3 Cycle Ageing

To gain a deeper understanding of the different ageing processes in LIB cells, and to start development of a regeneration procedure, various cycling conditions were employed. These conditions were selected to explore common factors contributing to cell ageing, allowing investigation of how ageing progresses in relation to different operational parameters. By conducting these investigations, valuable insights can be gained, aiding in the design of an effective regenerative approach.

Limited by the time frame of this work, cells 1-8 were aged for a total of 365 cycles between $V_{\text{min}} = 2.5$ V and $V_{\text{max}} = 4.2$ V. Additionally, half of the cells, cells 1, 2, 5, 6, were cycled with a charge current rate of 0.7C and a discharge current rate of 1C (0.7C/1C). The other half, cells 3, 4, 7, 8, were cycled with 0.5C/1C. These operational parameters were chosen to accelerate the ageing by setting all values in the upper limit of the recommended voltage and current values, see Table 3.1.

The implemented cycle ageing procedure, visualized in Figure 3.4, utilized CCCV charging. In CCCV charging, the operation switches between CC charging, which charges with a Constant Current (0.7C or 0.5C) and CV that charges at a Constant Voltage of $V_{\text{max}} = 4.2$ V. During CV, the cell is kept charging until the cut-off current is reached. For cells 1-4 a cut-off current of 0.2C was used and for cells 5-8 a cut-off current of 0.05C, inducing slightly different aging conditions for the cells. The cells cycled with a smaller cut-off current will reach a higher SoC, and consequently be cycled at a slightly larger SoC window.

The general voltage and current profile for a lithium-ion cell during the cycle ageing procedure is presented in Figure 3.4. The cells are cycled between V_{max} and V_{min} for a total of eleven cycles followed by a cycle comprised of ten second relaxation pulses every four minutes during the charge.

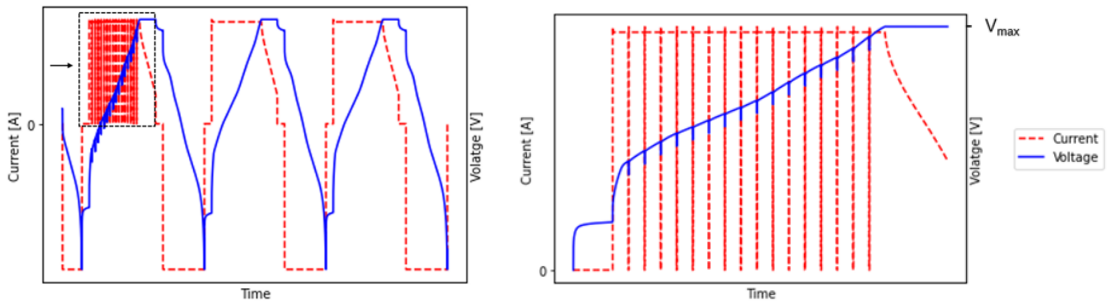

(a) (b)

Figure 3.4: Visualization of the general cycle ageing procedure (a). The procedure includes charge and discharge between V_{min} and V_{max} for eleven cycles, followed by an additional charge with implemented rest pulses highlighted in (a) every twelfth cycle. A zoomed in visualization of the marked area with the implemented rest pulses is seen in (b). Cycling repeated for a total of 365 cycles.

3.2.4 Regeneration

Regeneration was investigated through three different approaches, as seen below. Approach 1 aimed at reconnecting the i-Li to the anode. Approach 2 aimed at dissolving dendrites, the SEI as well as lithium crystals and other compounds where lithium-ion have been incorporated, and Approach 3 was a combination of the two.

3.2.4.1 Approach 1 - Reconnection

The cell was first charged using CCCV at 0.3C with a cut-off current of 0.05C following a published work by *Liu et al.*. Afterwards a discharge for two minutes at 1C was implemented with the purpose of stripping plated lithium. The cell was then rested for ten minutes before discharging fully at 0.1C. This procedure was done in ten cycle increments, reaching a total of 52 cycles, including a DC pulse at the beginning and end of each increment to be able observe any potential regeneration occurring throughout the experiment. A schematic representation of the cycle procedure with the representative steps marked is illustrated in Figure 3.5.

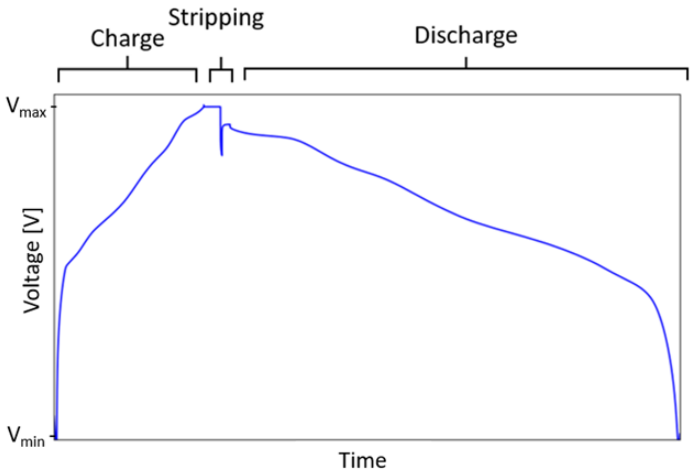

Figure 3.5: Visualization of a general cycle in regeneration Approach 1. The procedure includes a charge up to $V_{\max}$, followed by a fast stripping discharge and a subsequent slow discharge.

3.2.4.2 Approach 2 - Pulsing

Approach 2 is a pulsing method based on earlier a technology used for regeneration in lead-acid batteries. A test matrix was developed where different charging rates, pulse duration, number of pulses and SoC levels were explored (see Table 3.2), resulting in a total of 48 test iterations. To track the progress throughout the experiment, the capacity gain for each pulse was calculated.

Table 3.2: Test matrix for Approach 2.

Current Rate	Pulse Duration	Number of Pulses	Initial State of Charge
1C	100 ms	10	20%
1C	100 ms	100	20%
1C	100 ms	1000	20%
1C	500 ms	10	20%
1C	500 ms	100	20%
1C	500 ms	1000	20%
1C	100 ms	10	40%
1C	100 ms	100	40%
1C	100 ms	1000	40%
1C	500 ms	10	40%
1C	500 ms	100	40%
1C	500 ms	1000	40%
1C	100 ms	10	60%

Continued on next page

Table 3.2: Test matrix for Approach 2. (Continued)

1C	100 ms	100	60%
1C	100 ms	1000	60%
1C	500 ms	10	60%
1C	500 ms	100	60%
1C	500 ms	1000	60%
1C	100 ms	10	80%
1C	100 ms	100	80%
1C	100 ms	1000	80%
1C	500 ms	10	80%
1C	500 ms	100	80%
1C	500 ms	1000	80%
2C	100 ms	10	20%
2C	100 ms	100	20%
2C	100 ms	1000	20%
2C	500 ms	10	20%
2C	500 ms	100	20%
2C	500 ms	1000	20%
2C	100 ms	10	40%
2C	100 ms	100	40%
2C	100 ms	1000	40%
2C	500 ms	10	40%
2C	500 ms	100	40%
2C	500 ms	1000	40%
2C	100 ms	10	60%
2C	100 ms	100	60%
2C	100 ms	1000	60%
2C	500 ms	10	60%
2C	500 ms	100	60%
2C	500 ms	1000	60%
2C	100 ms	10	80%
2C	100 ms	100	80%
2C	100 ms	1000	80%
2C	500 ms	10	80%
2C	500 ms	100	80%

Continued on next page

Table 3.2: Test matrix for Approach 2. (Continued)

2C	500 ms	1000	80%

The procedure started with a 0.3C charge to the desired SoC, followed by a 30 minutes rest before running a DC pulse measurement, to later apply the pulses. After the pulses had finished, the capacity gained during the pulses was discharged using a current rate lower than 0.2C while reaching the equilibrium. This procedure was then repeated to allow the comparison of the DC pulse with the pre-pulsing DC pulse reference. The resistance measurement of the DC pulses was later on discarded and is not shown in the report. A schematic representation of the cycling procedure with the representative steps is illustrated in Figure 3.6.

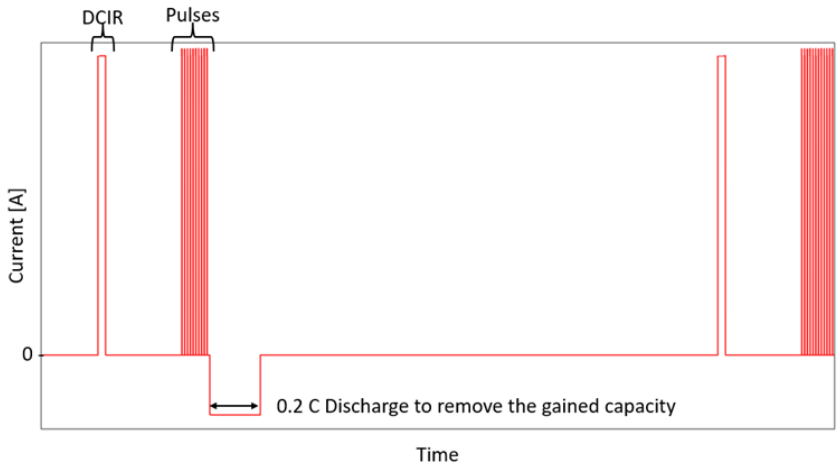

Figure 3.6: Visualization of the procedure in regeneration Approach 2. The procedure includes a DC pulse easement marked as DCIR, followed by the pulses of amplitude and duration decided accordingly to the iteration and a subsequent discharge to remove the gained capacity during the pulses. After the initial SOC is established, the cells were rested for 30 minutes before the DC pulse and the next iteration of pulses.

3.2.4.3 Approach 3 - Combination

Approach 1 and 2 were then combined to create a third approach, which was aimed at capitalizing on the strengths of both techniques. For this approach, pulsing was executed during the day and the reconnection scheme was implemented during the night. Using the same parameters as in Approach 2, fractional factorial design was utilized to reduce the number of iterations from 48 down to 16, see Table 3.3.

As in Approach 2, DC pulse measurements and capacity gain calculations were used to monitor the potential regeneration between iterations. Similarly, the cell was also charged up to the desired SoC at 0.3C followed by a 30 minute rest before the initial DC pulse measurement. The pulses were ran, after which the gained capacity was discharged. After a set of two pulses at the same SoC along with the

final DC pulse was completed, the cell was charged and discharged using the same parameters as for Approach 1, including the stripping step. As for Approach 1, the resistance values calculated from the DC pulse for comparison are discarded. Upon complete discharge, the cells were allowed to rest until the next set of pulses was commenced.

Table 3.3: Test matrix for Approach 3, developed using fractional factorial design.

Charging Rate	Pulse Duration	Number of Pulses	State of Charge
1C	100 ms	10	20 %
1C	500 ms	100	20 %
1C	100 ms	1000	40 %
1C	500 ms	10	40 %
1C	100 ms	100	60 %
1C	500 ms	1000	60 %
1C	100 ms	1000	80 %
1C	500 ms	100	80 %
2C	100 ms	1000	20 %
2C	500 ms	100	20 %
2C	100 ms	10	40 %
2C	500 ms	1000	40 %
2C	100 ms	1000	60 %
2C	500 ms	100	60 %
2C	100 ms	100	80 %
2C	500 ms	10	80 %

3.3 Differential Voltage Analysis & Incremental Capacity Analysis

DVA and ICA are non-invasive techniques used for investigating battery and cell degradation mechanisms and capacity estimation. Typically, DVA and ICA are complemented by half-cell measurements. However, this was not possible in this study, instead, the experimental part begun with an initial characterization where the obtained DV and IC curves at the BoL for all cells were compared to literature to first identify the cell chemistry. The peaks where then identified and attributed to the different active electrode materials. After the initial characterization was completed, the DV and IC curves obtained after ageing and regeneration could be analyzed with the purpose of investigating the evolution of different degradation modes.

RPT cycle 2, the same slow cycle that was used to evaluate capacity fade, was then used to generate the profiles for DVA and ICA. Low C-rate charge/discharge data is needed to minimize the polarization effect. Using the voltage curve obtained at 0.1C, which is close to the equilibrium state, is enough to allow accurate observations of degradation phenomena [72]. Depending on cell quality, instrument resolution, and data recording settings, DV-IC profiles obtained by numerical differentiation are vulnerable to noise, as seen in Figure 3.7, where different amount of filtering is applied to the DV curve. For all obtained DV-IC profiles, differentiation and smoothing was performed in Python using a constant voltage interval ΔV of 10 mV between measurement points, which corresponding to what can be seen in Figure 3.7, provided an acceptable amount of smoothing without extensive curve morphing.

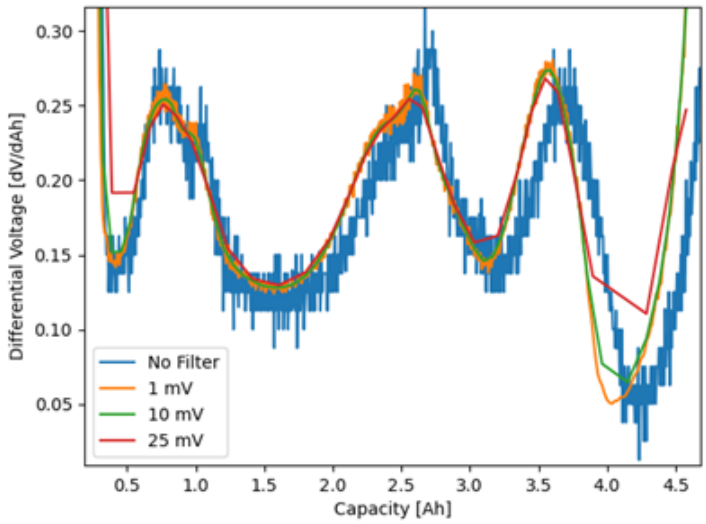

Figure 3.7: Influence of the filtering on the measured noise in a DV curve.

3.4 Electrochemical Impedance Spectroscopy

Specifically, Galvanostatic EIS - Adaptive Amplitude (GEIS-AA, hereon referred to as EIS) was used for all measurements since the cells studied are low-impedance systems. The equipment used for the EIS measurements was a Biologic MPG-210 battery tester, using a modulation amplitude of 10 mV and a frequency range from 10 kHz to 10 mHz. It was performed at 50 % SoC in connection to the RPT. The cells were discharged using 0.2C and charged using 0.33C. After reaching the desired SoC, and before performing EIS measurement, the cells were rested for one hour to eliminate any major diffusion effects which could impact the results.

3.5 Internal Resistance Measurement

As LIB cells starts to age, their internal resistance tend to increase. The resulting voltage response for an applied current load will therefore be altered, affecting both the capacity and power of the cell. In general, the better the battery, the lower the internal resistance. Therefore, the internal resistance is often used as an indicator of battery health.

Internal resistance calculations are incorporated throughout. At BoL, after ageing and after regeneration the AC internal resistance was measured using EIS. DC internal resistance calculations was also implemented in the initial RPT performed at BoL as well as after ageing, and was calculated using Equation 2.4 by applying four 30 seconds long 1C charge current pulses and four 30 seconds long 1C discharge current pulses during the RPT. The DC internal resistance was discarded after regeneration as well as for the rest pulses incorporated in the cycle procedures.

4

Results & Discussion

The results are presented below and divided into three different sections representing the cells life-cycle. Firstly, the results obtained during BoL are presented. These results are used as reference and evaluation of cell-to-cell variations as well acting as a reference for the ageing and regeneration steps. This section is followed by the results obtained after the cycle ageing the cells, focusing on connecting the results from the electrochemical tests to potentially occurring ageing phenomena. To distinguish and explain the cell degradation behaviour, DV, IC and EIS was performed to quantitatively analyze the degradation contributions from the different cell components and cycle parameters. The observed ageing was compared with results from the literature in order to distinguish the similarities and differences from previous work. Moreover, by comparing fresh and aged cells it was possible to further confirm if the capacity loss was ascribed to LLI, LAM, or impedance rise. Next the results from the regeneration procedures are presented. Additionally, the different operational parameters and their effect of the different degradation modes and mechanisms are analyzed.

4.1 Initial Characterization & Validation - Beginning of Life

Before cycling, RPT and EIS were performed for all nine cells. Additionally, a formation test was done for the reference cell. Formation tests were assumed to have been carried out by the manufacturer but were executed for the reference cell for verification purposes. As a complement, differential analysis and EIS provided a thorough characterization of the cell before ageing, assisting in the evaluation of potential changes observed during ageing or regeneration. Moreover, a comparison of the cells at BoL provides data used to evaluate cell-to-cell variations.

4.1.1 Formation Test

The formation test performed on the reference cell is presented in Figure 4.1. The charge and discharge capacities for the four formation cycles was measured, as seen in Figure 4.1a, where the red and blue circles indicate the capacity, and appurtenant endpoints of the charge and discharge in Figure 4.1b. The results show a stable discharge capacity value of 4.72 Ah for the different cycles. As the capacity is

constant for all cycles, formation testing can be confirmed to have be performed by the manufacturer and no additional formation was required on the other cells.

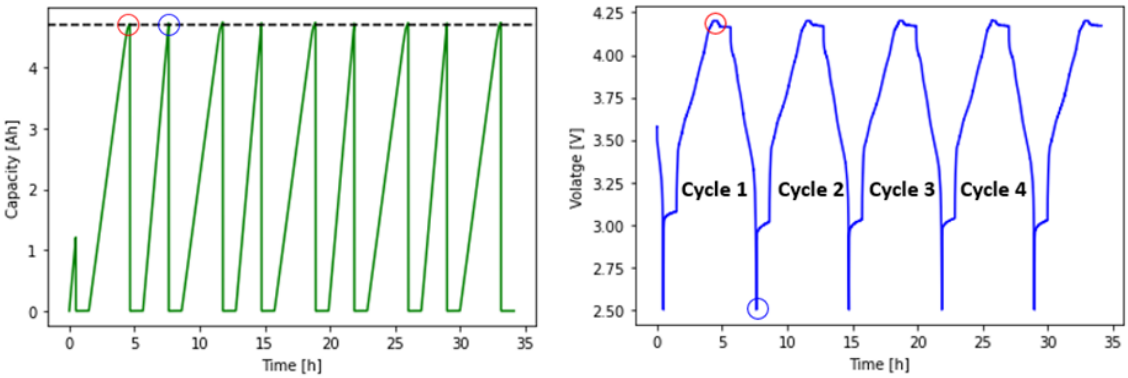

(a) (b)

Figure 4.1: (a) The measured cell capacity [Ah] and (b) voltage [V] during the formation test plotted against time [h] for the reference cell. A red circle marks the endpoint of the charge and the associated charge capacity value and a blue circle marks the endpoint of the discharge and the associated discharge capacity.

4.1.2 Initial Reference Performance Test

The resulting RPT performed at BoL for the reference cell and cells 1-8 can be seen in Figure 4.2. No significant fluctuations between the cells can be observed. The capacity is determined from the C/10 cycle (cycle 2), where the endpoints of the charge (red circle) and discharge (blue circle) are marked in Figure 4.2b and the associated charge and discharge capacities are marked in Figure 4.2a.

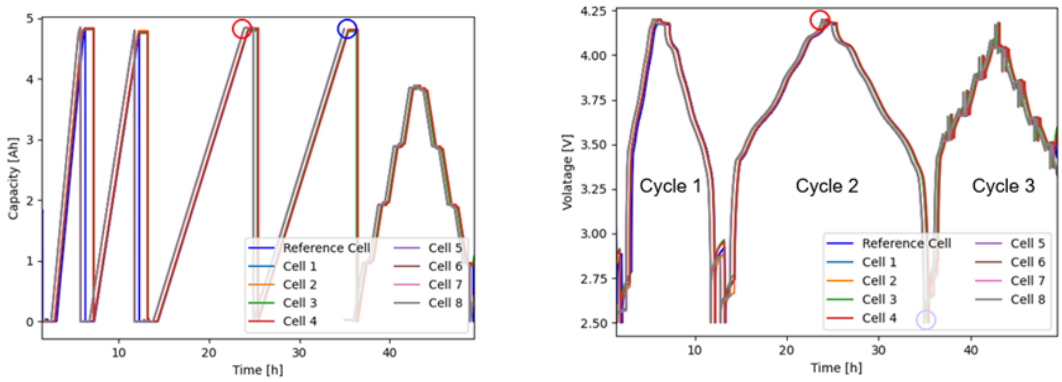

(a) (b)

Figure 4.2: Measured cell capacity (a) [Ah] and voltage (b) [V] plotted against time [h] during the initial RPT for all cells. The red circle marks the endpoint of the charge and the associated charge capacity value and the blue circle marks the endpoint of the discharge and the associated discharge capacity.

As the RPT results for the different cells overlaps, it can be assumed that formation has been performed beforehand by the manufacturer on all cells.

Figure 4.3 illustrates the capacity variations obtained for all cells, demonstrating a 4.81 ± 0.012 Ah on average. The capacity measured is consistent among the cells, further demonstrating the consistency of the cell performance. The nominal capacity of the cells is 4.79 Ah according to the supplier data sheet.

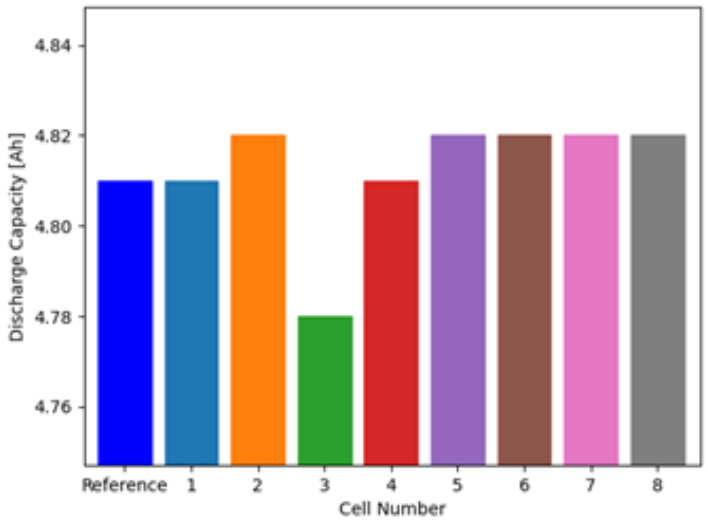

Figure 4.3: Bar plot of the measured discharge capacity [Ah] obtained from the initial RPT for all cells.

From the initial RPT it is found that the cells exhibit little cell-to-cell variations. The consistency in the cell quality assures that any observations in terms of cell performance do not originate from initial cell-to-cell variations, but more likely as a result of test conditions.

4.1.3 Differential Analysis, Initial Cell Characterization

DVA and ICA are useful techniques for investigating battery and cell degradation. A major shortcoming of IC compared to DV is that the contribution of the electrodes is convoluted, hence making each electrodes individual impact troublesome to evaluate. By careful peak indexation, however, this can be somewhat mitigated, facilitated by identifying the electrode composition and chemistry. As according to Equation 2.7, the full cell voltage is the anode potential subtracted from the cathode potential. Consequently, the peaks appearing in the full cell differential curve will be contributed to either electrode. The individual electrode peak contribution was determined by comparisons to the literature.

Since the exact chemical composition of the cells was not provided by the manufacturer, the obtained DV and IC curves for the cells were compared to signature peaks

of different electrode compositions. The supplyer data sheet defined the cylindrical calls as Lithium Nickel Manganese Cobalt Oxide (NMC). NMC cathodes have the general formula $LiNi_xMn_yCo_{1-x-y}O_2$, but there exists multiple relative stoichiometries of the three defining metals components. In EVs, NMC811 is a common cathode composition. By comparing the different features of the DV and IC curves to earlier work and the supplier's earlier iterations on the LG-M50 cells, it become possible to approach the composition of the cells as NMC811 with a silicon-graphite composite anode [73–76].

Presented in Figure 4.4 is the BoL DV during charge for cells 1-8. Using experimental data from other studies [73–76], the three main peaks can be assigned. The DV curve exhibits three main peaks, the first peak to the right, is composed of P_{NI} and P_{NII}, which reveals the signature of the Si-G anode, while the last peak P_{PII}, is contributed from the cathode. By comparing to [73–76], the second peak can be assumed to include contributions from both the anode P_{NIII}, and the cathode, *i.e.*, the small bump P_{PI} observed right before the sharp tip (assigned to the anode) of the peak. P_{NI}, P_{NII}, and P_{NII} represent the ordered transitions of graphite staging, as illustrated in Figure 2.2. In addition, the characteristic capacity values of the different material components in the electrodes can be quantified, namely silicon, carbon, Si-G, NMC and NMC/Si-G.

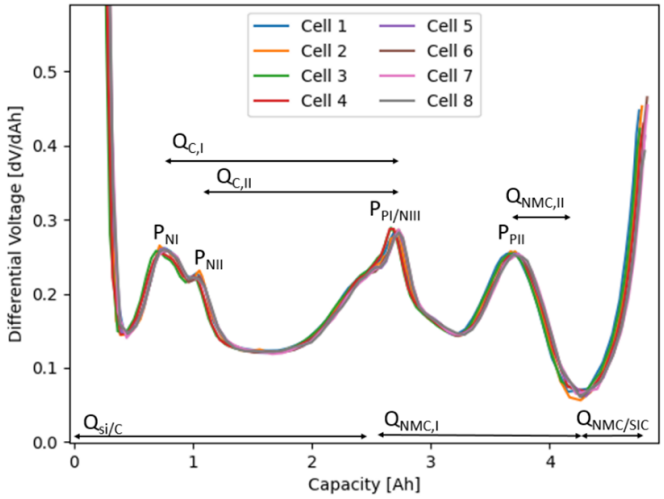

Figure 4.4: DV [dV/dAh] plotted against capacity [Ah] for cells 1-8. Peaks and characteristic capacities are marked according to [73–76].

Figure 4.4 marks the allocation of material characteristic capacities to the distinctive DV indicators based on the experiments performed by [73–76]. $Q_{\mathrm{Si/C}}$ is represented by the distance between the left boundary of the DV curve (0 % SoC) and the main graphite peak, P_{NIII}. This peak specifies the phase transition between LiC_{12} and LiC_6. In general, variations of $Q_{\mathrm{Si/C}}$ during cycling can be correlated to a change in the storage capabilities of the anode. The capacities represented by $Q_{\mathrm{C,I}}$ and $Q_{\mathrm{C,II}}$, which lies between the local maxima and the main graphite peak, describe the storage capability of graphite. Similarly, $Q_{\mathrm{NMC/SiC}}$, defined by the measure of distance

between the right border (100 % SoC) and the third main peak, provides information related to electrode balancing and partly the cathode storage capability. Q_{NMC} provides a more representative measure of the cathode's storage capacity.

Comparing the different cells, the specific characteristic capacities' shape of the peaks imply no significant deviation between the cells. Potential differences are often difficult to determine with certainty due to both intrinsic and extrinsic reasons.

Si additive slightly alters the voltage profile of the cell. The differences takes the form as two additional peaks in the DV curve close to 0 % SoC, attributed to the addition of Si. However, these peaks could not be distinguished in the DV curve for cells 1-8. Perhaps acquiring the data using an even smaller current than C/10 is needed, as *Zilberman et al.* reported the presence of both Si peaks using data acquired at the low current of C/30 [76]. Interestingly, after ageing cell 1 indicated a possible contribution from Si. This will be discussed further on.

According to *Jung et al.* [77], *Fuchsbichler et al.* [78] and *Schindler et al.* [74], the peaks of the IC curves illustrated in Figure 4.5 can be assigned to the following phase transformations: P_{I} to the deintercalation of lithium in the Si-G anode, P_{II} as a phase transition within the NMC cathode, and peaks $P_{\mathrm{III-IV}}$ to be specific to NMC811 cathodes.

Comparing cell-to-cell variations, no peak shift can be observed. However, a slight difference in the height of P_{IV} for cell 2 is noted compared to the rest of the cells. But as all other peaks overlap, and the initial RPT exhibited no major differences between cells, this is most likely caused by the use of different battery testers or measurement noise. Both the curve fitting and filtering has a large influence on DVA and ICA, as highlighted in Figure 3.7. The indirect impact of individual battery testers can not be neglected either, as the raw data extracted varies depending on the tester.

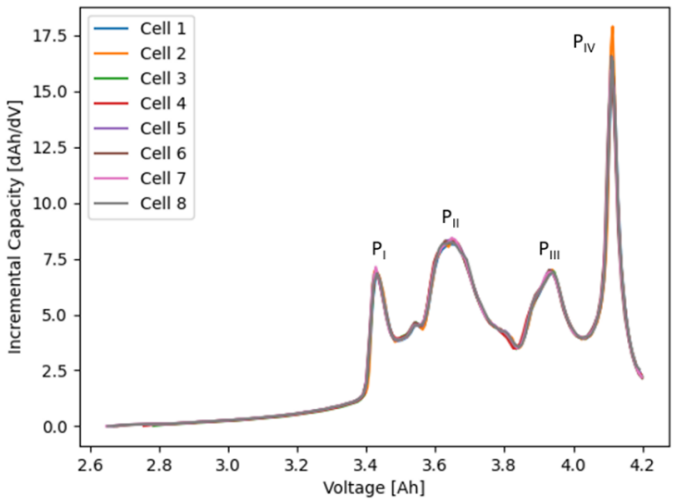

Figure 4.5: Incremental capacity [Ah/dV] plotted against voltage [V] for cells 1-8. Peaks are marked according to [74].

4.1.4 Electrochemical Impedance Spectroscopy, Initial Cell Characterization

The initial EIS for all cells was conducted at 50 % SoC and the resulting Nyquist plots can be seen in Figure 4.6. A variance among the cells can be observed, which is likely due to extrinsic changes and interferences affecting the equipment. Ideally when performing EIS measurements, no interference or change of cables, cell holders *etc.* should be done, as while EIS is a powerful characterization technique, it is also very sensitive to variations which will impact the measurement. Due to the environment of the lab in question, as well as the high demand of the equipment, it was not possible to maintain an ideal setup. Hence variations between measurements will occur, especially for the ohmic resistance.

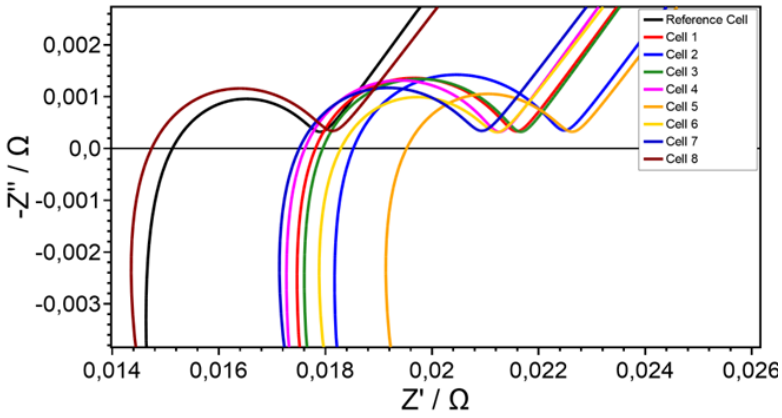

Figure 4.6: Nyquist plots for all cells at 50 % SoC before ageing with the best-fitted ECM.

4.2 Cycle Ageing of the Cells

The immediate effects of battery ageing are observed as losses of capacity and power. Some metrics for quantifying these performance losses are presented and discussed below, namely the evolution of cell capacity, polarization, impedance, and temperature. These tools provide a fair share of information about the rate and severity of the ageing.

4.2.1 Capacity Fade

Ageing was performed for a total of eight cells, all cycled between 2.5 V and 4.2 V for 365 cycles. Figure 4.7 presents the obtained relative capacity fade with increasing number of cycles. The exact reading of the capacity fade is not representative of the actual SoH of the cells. For a correct reading based on similar circumstances see Table 4.1. No significant difference is seen between cells except for cell 1 as it deviates linear capacity fade. Such behaviour was judged non-representative of the cell behaviour. Hence cell 1 is neglected for the purpose of further experiments. The cell degradation is discussed further down based on the different analytical techniques.

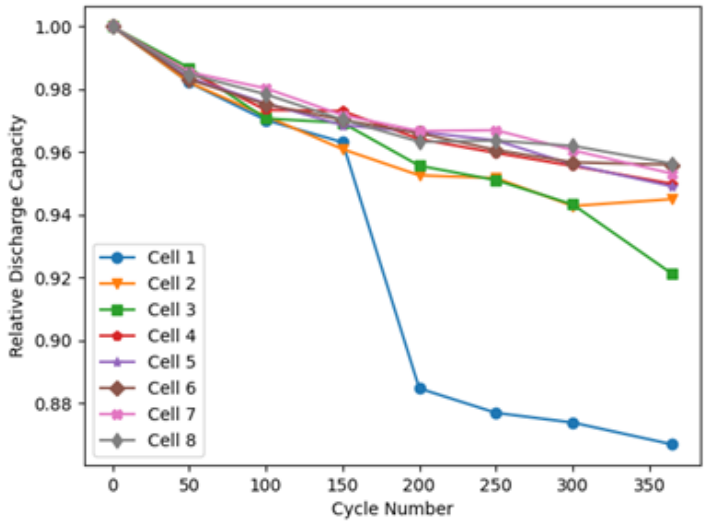

Figure 4.7: Measured relative capacity fade for cells 1-8 during cycling, plotted against the number of cycles.

Table 4.1 summarizes the BoL capacity, after ageing (AA) capacity, and the resulting capacity fade for each of the cells. The capacity for cells reaching their EoL after ageing is typically decided as 80 % of the initial BoL capacity. However, due to the time limit of this project, neither of the cells reached anywhere near that SoH.

Table 4.1: Capacity fades for cells 1-8 after 365 cycles. The capacity values are based on the RPTs done at BoL and after ageing.

Cell number	Charge rate	Total # of cycles	BoL Capacity	AA Capacity	Capacity Fade	SoH
1	0.7 C	365	4.81 Ah	4.37 Ah	9.10 %	90.92 %
2	0.7 C	365	4.82 Ah	4.67 Ah	3.10 %	96.90 %
3	0.5 C	365	4.78 Ah	4.68 Ah	2.11 %	97.89 %
4	0.5 C	365	4.81 Ah	4.68 Ah	2.72 %	97.28 %
5	0.7 C	366	4.82 Ah	4.66 Ah	3.18 %	96.82 %
6	0.7 C	365	4.82 Ah	4.67 Ah	3.14 %	96.86 %
7	0.5 C	366	4.82 Ah	4.67 Ah	3.18 %	96.82 %
8	0.5 C	366	4.82 Ah	4.67 Ah	3.16 %	96.84 %

As observed in Figure 4.7 and Table 4.1, there is no significant difference between cells 2 through 8 cycled at 0.5C/1C and 0.7C/1C. No correlation can be drawn between capacity loss and charge current rate after 365 cycles, as cells 5 and 7 cycled with two different current rates still exhibited the same capacity fade. In addition, cell 8 cycled at 0.5C/1C experienced a higher capacity fade than both cell 2 and 6 cycled at 0.7C/1C.

When comparing cells 2-4 with cells 5-8, a difference in capacity fade can be observed. The two sets of cells were cycled using two different battery testers, cells 1-4 using PEC and cells 5-8 using MACCOR. Moreover, the battery testers cycled the cells using slightly different procedures. Cells 5-8 were cycled using a lower cut-off current (C/20) compared to cells 1-4 (C/5). Due to this, cells 5-8 were cycled with a marginally larger SOC window, charging to a slightly higher SoC as compared to cells 1-4. Potentially as a consequence to the different SoC windows, cells 5-8 experience a higher capacity fade after cycling as compared to cells 2-4, with the exception of cell 1 which is considered an outlier.

4.2.2 Galvanostatic Voltage Profiles

Presented in Figure 4.8a-d are the charge and discharge curves for all cells at the BoL and after ageing. For cells 2-8, the shape of the charge and discharge curves does not considerably change as the cells age, indicating a lower degree of degradation. For all cells, the endpoint of the curves shifts towards lower capacities with the increasing number of cycles, representing the observed capacity loss. The position of certain plateaus shifts towards lower voltages as the cells age, advocating further cell degradation [79]. The implication of this and the underlying degradation mechanisms can be further analyzed using DVA and ICA, and is discussed further in Section 4.1.3.

As seen in Figure 4.8, many of the cells show similarly behavior both before and

after ageing, suggesting similar degradation mechanisms are occurring. As with the SoH, cell 1 demonstrates a certain aberration from cells 2-8, both regarding capacity decline and plateau shift.

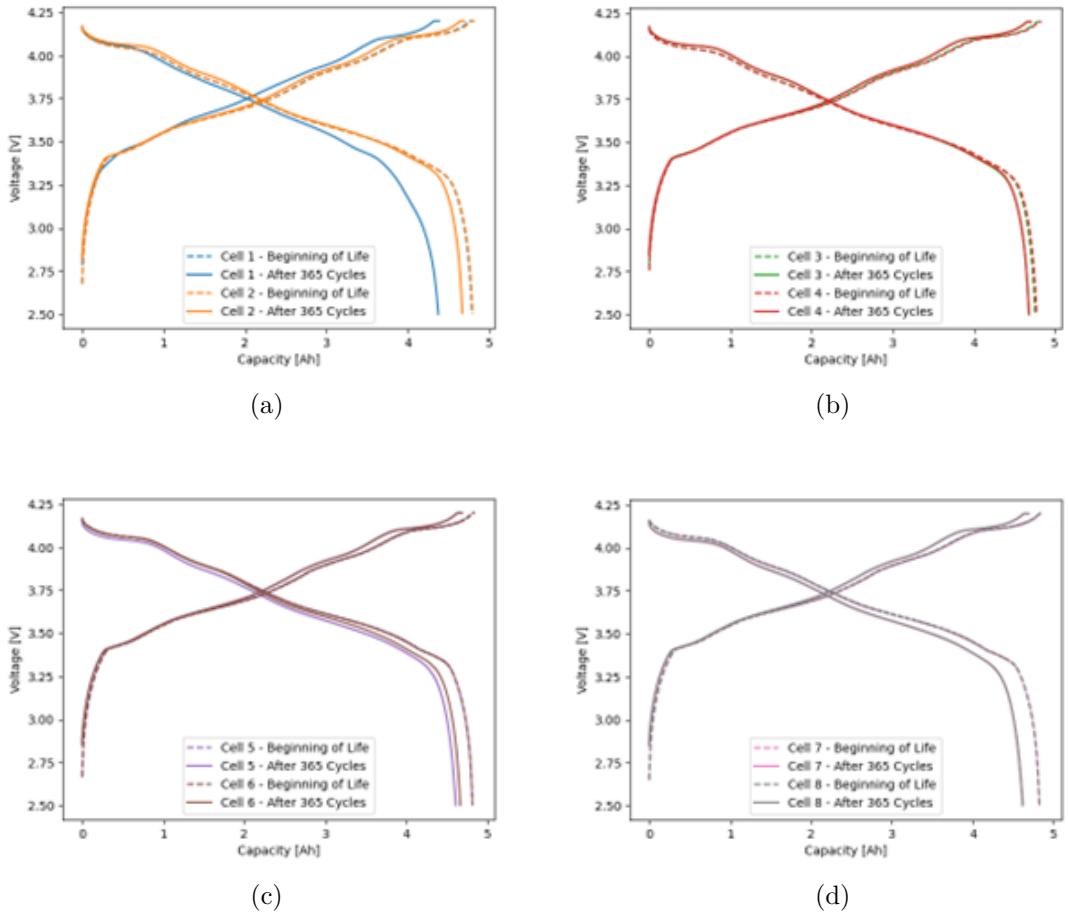

Figure 4.8: Measured charge and discharge voltage [V] profile plotted against the capacity [Ah] for cells 1-2 (a), 3-4 (b), 5-6 (c) and 7-8 (d) at BoL and after 365 cycles.

4.3 Cell Degradation Due to Cell Cycling

In Figure 4.9 the full cell charge (a) and discharge (b) voltage is plotted alongside the DV before and after 365 cycles, highlighting the relationship between the voltage plateaus and DV peaks. From the earlier characterization, see Section 4.1.3, peak P_1 can be assigned as a contribution from the anode, P_2 as a contribution to both the anode and cathode, and P_3 the cathode. More specifically, it was concluded that peaks P_{1-3} characterize the graphite staging and different phase transformations in the cathode. This identification process is illustrated in Figure 4.9.

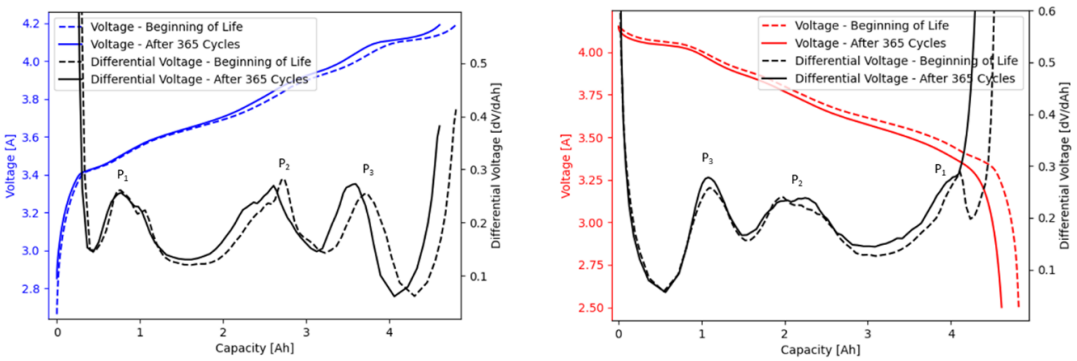

(a) (b)

Figure 4.9: Measured voltage [V] and DV [dV/dAh] plotted against the capacity [Ah] at BoL and after 365 cycles during charge (a) and discharge (b) for cell 5.

The IC curve for cell 5 during charge and discharge before and after ageing is presented in Figure 4.10. The peaks correlating to the identified phase transformations are marked based on the results from the initial characterization: P_{I} representing the deintercalation of lithium out of the Si-G anode, P_{II} to transformations within the NMC cathode, and P_{III} and P_{IV} to the cathode as well since they exhibit a behaviour possibly linked to the specific NMC811 composition.

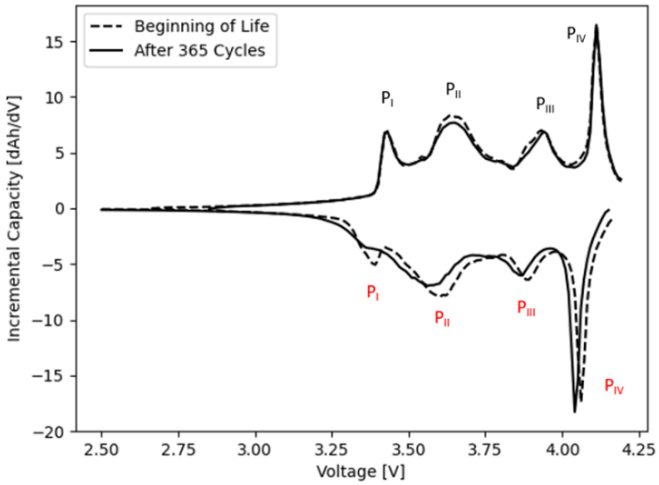

Figure 4.10: Measured IC [dAh/dV] plotted against voltage [V] at BoL and after 365 cycles during charge and discharge for cell 5.

To evaluate the curve variation evoked during ageing, the observed peak shifts in Figures 4.9 and 4.10 are marked and highlighted in Figures 4.11 and 4.12 respectively. As can be seen in Figure 4.11, not all peaks shift proportionally to each other, which would otherwise be expected of uniform loss of active material. A disproportionate

shift of the peaks imply that the capacity available for the specific reaction or phase transformation, determined by the characteristic capacity, has been reduced. In Figure 4.11 the uniform peak shifts are marked with red arrows (LLI), and the nonuniform with blue (LAM). A shift in peak P_1 is detected after ageing, indicating that the capacity available for the graphite ($Q_{\mathrm{Si/C}}$) or the phase transition between LiC_{12} and LiC_6 (Q_{CI}, Q_{CII}) was reduced during charge. In contrast, the distance between the endpoint of the curve and P_3, representative of the storage capability of the cathode, exhibited a uniform shift and hence no identifiable degradation ($Q_{\mathrm{NMC/SiC}}$) with cycling. During discharge, no apparent shift can be seen for peaks P_1 and P_2, and the shift of peak P_3 is hard to distinguish.

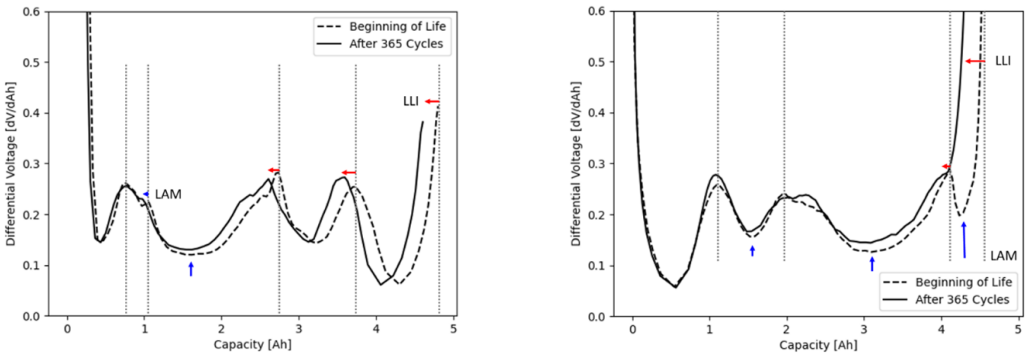

(a) (b)

Figure 4.11: Measured DV [dV/dAh] plotted against the capacity [Ah] at the BoL and after 365 cycles during charge (a) and discharge (b) for cell 5. The underlying degradation modes causing the observable changes in the curves are marked.

The IC in Figure 4.10 illustrate a decrease in P_{II} peak height during charge, when looking at the results after cycling. The corresponding point in the DV curve, see Figure 4.11a, exhibits a decrease in valley depth. This is an indication of LAM, as described in Table 2.3. Moreover, as P_{II} is attributed to the cathode, it can further be assumed to be $\mathrm{LAM_{PE}}$. This could be attributed due to the structural degradations such as the evolution of microcracks across the cathode or possibly even conductivity loss. This is further verified as degradation mechanisms for NMC/Si-G cell by *Li et al.*.

Despite the non-uniform evolution in IC curve peak, the shape remains almost the same and return to the same baseline voltage, suggesting that the cell reaction kinetics have not been significantly hindered. According to *Dubarry et al.* [80], the capacity fades is neither stemming from alternations in the interfacial kinetics of the cell nor the internal impedance, but instead suggests the $\mathrm{LAM_{PE}}$ to be associated to Mn dissolution. However, to conclude the actual cause of the $\mathrm{LAM_{PE}}$ evoked in the cells, *post-mortem* analysis is required.

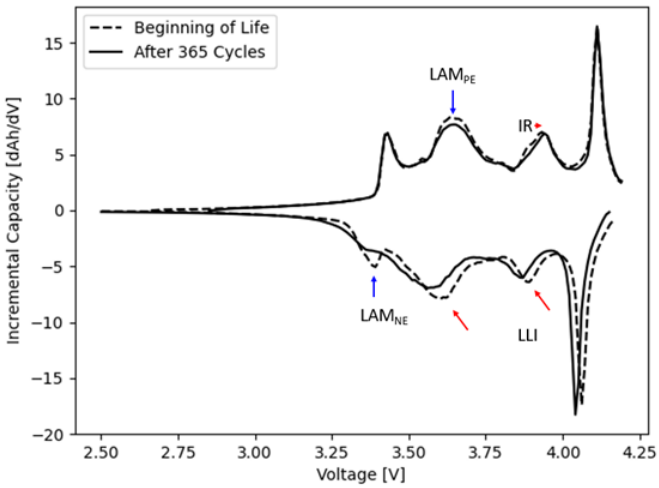

Figure 4.12: Measured IC [dAh/dV] plotted against voltage [V] at BoL and after 365 cycles during charge and discharge for cell 5. The underlying degradation modes causing the observable changes in the curves are marked.

When looking at the voltage profiles, Figure 4.8, as well as the DV, Figure 4.11, a consistent trend of shifting towards lower capacities can be observed. This is an indication of capacity lost due to LLI, which can further be attributed to secondary reactions, such as electrolyte decomposition, continuous SEI growth and lithium plating, all of which result in further consumption of lithium ions.

In Figure 4.12, the height of P_{I} during discharge is found to decrease at a constant voltage. The corresponding DV valley in Figure 4.11b is simultaneously decreasing in depth. The combination of both phenomena indicates the occurrence of $\mathrm{LAM}_{\mathrm{NE}}$, causing capacity loss related to the deintercalation of the Si-G anode. The loss of anode active material could potentially be related to the large volume expansions during lithiation. In addition to the valley decreasing in depth, the discharge peak P_{I} is marginally decreasing in height and becomes flatter, indicative of possible structural changes occurring associated with the graphite staging [81].

Herein, the DVA needs to be complemented with the ICA. Though the curve shift in Figure 4.11b is hard to distinguish, most valley depths are seen to decrease, potentially indicating LAM. In the ICA, discharge peaks P_{II} and P_{III} exhibit a shift towards lower capacities whilst simultaneously decreasing in peak height. This is generally contributed to LLI. However, as the DV peak does not shift towards lower capacities as expected but instead decrease in valley depth, this could potentially be attributed to a combination of LAM and internal resistance increase. Increase in internal resistance typically corresponds to an increase in the peak slope of the DV curve and for an IC peak a shift towards higher, or lower, voltages whilst the peak height is left constant [82, 83]. Due to these complications, further conclusions cannot be drawn without the addition of *post-mortem* analysis.

Since most cells degraded to a similar degree, it is of interest to investigate if the

various charge current rates or SoC windows evoked different degradation modes. In Figure 4.13 and 4.14 the discharge DV curve and IC curve for all cells is presented respectively. A clear distinction is seen between cell 1 and 2, further enhancing unpredictability and uncertainty regarding the degradation of cell 1. However, after ageing a potential DV peak related to Si is observed close to 0 % SoC. The DV and IC curves for cells 2-4 after ageing differs slightly from those presented in Figures 4.11 and 4.12. The main differences belongs to the discharge peaks $P_{\mathrm{I-III}}$ and the corresponding DV valley to discharge peak P_{I}. Cells 2-4 exhibit a deeper valley, as well as less of a decrease in peak height for peaks $P_{\mathrm{I-III}}$ compared to the same features of cells 5-8. By evaluating these differences, cells 2-4 experience LLI and $\mathrm{LAM_{NE}}$ to a lesser degree than cells 5-8. The lesser degree of $\mathrm{LAM_{NE}}$ and LLI coincides with the lower capacity fade for these cells. From Figure 2.4, the SoC is known as an important stress factor in causing both $\mathrm{LAM_{NE}}$ and LLI.

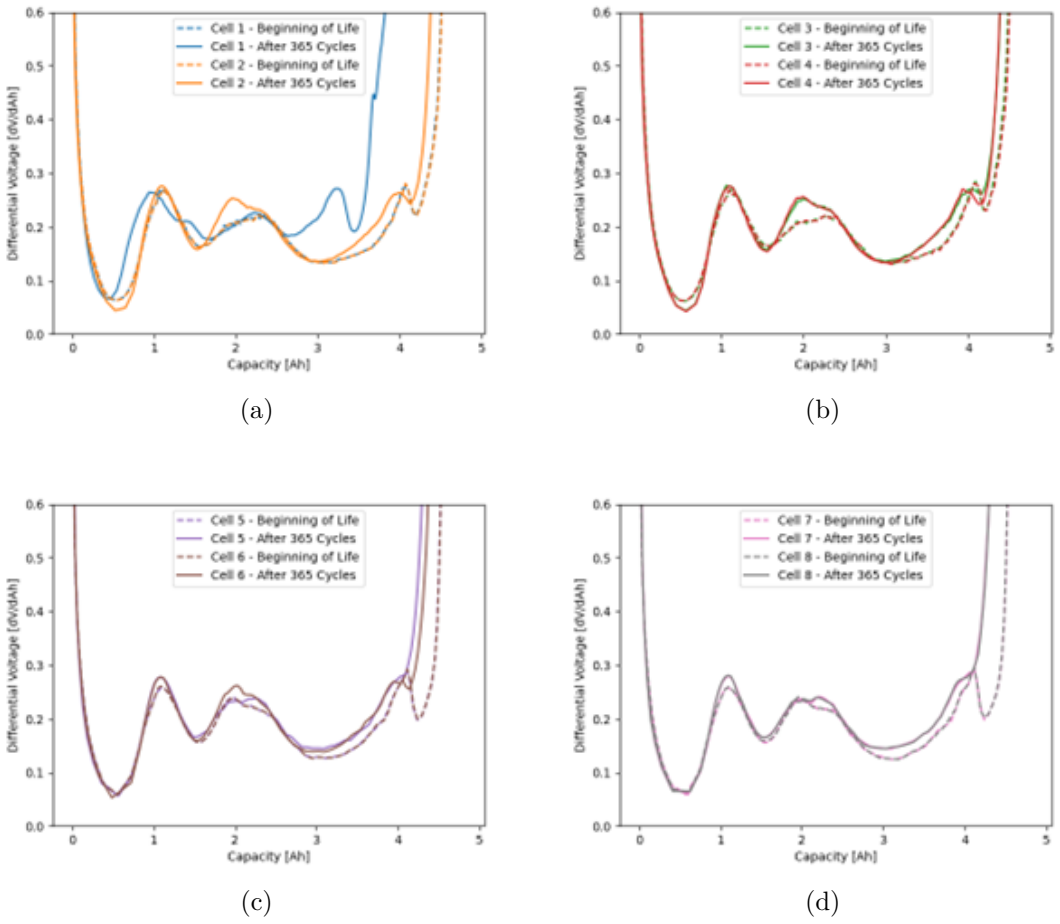

Figure 4.13: DV [dV/dAh] plotted against capacity [Ah] during discharge for cells 1-2 (a), 3-4 (b), 5-6 (c) and 7-8 (d) before and after ageing.

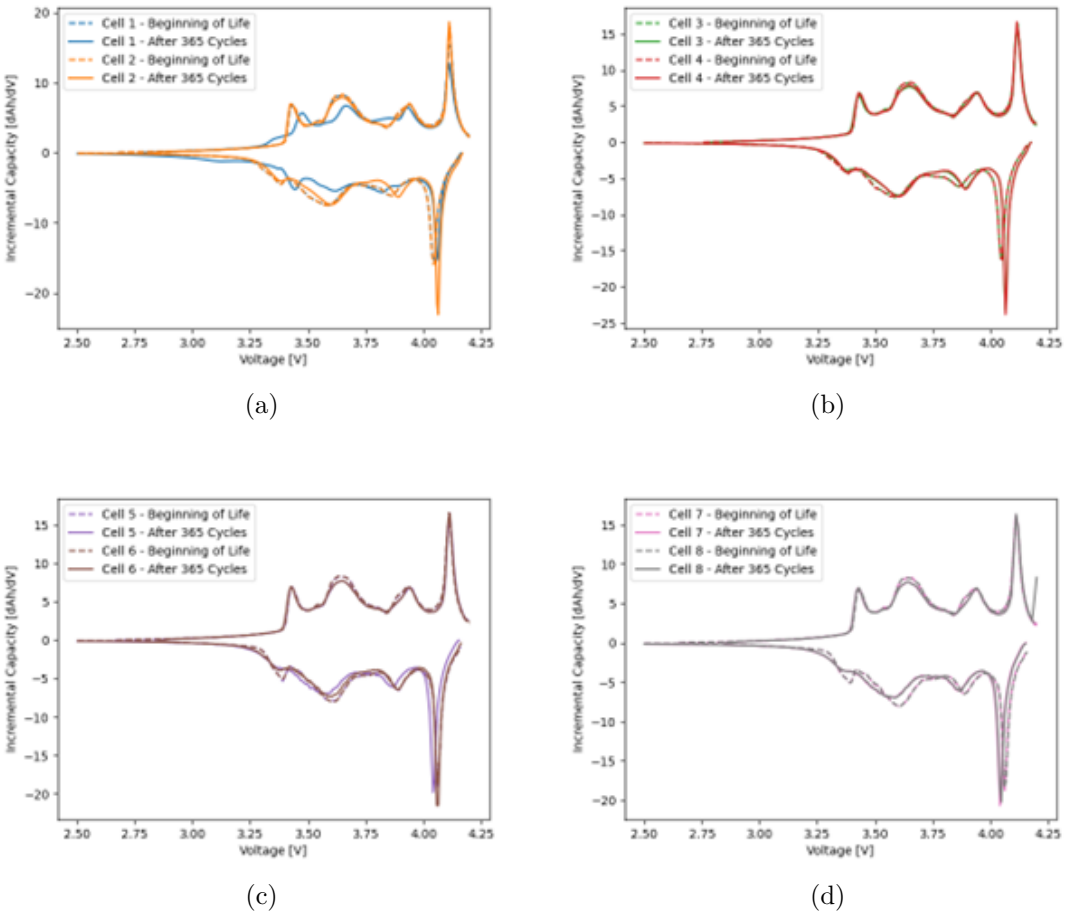

Figure 4.14: IC [dAh/dV] plotted against voltage [V] during discharge for cells 1-2 (a), 3-4 (b), 5-6 (c) and 7-8 (d) before and after ageing.

Visually, for all cells, the fraction of capacity lost to LAM and LLI appears proportional. Due to the likely addition of silicon in the anode, excessive volume expansions during intercalation can be expected which in turn increases the risk of SEI growth. Hence, simply based on the cell chemistry, it could be hypothesised that SEI would be the dominating degradation mechanisms causing LLI, and not lithium-plating. In addition, silicon displays a higher lithium-alloying potential relative to the low discharge potential of graphite, which can alleviate potential lithium plating [84].

One additional feature of the DV curve, which varies between the two sets of cells, is the peak height of discharge peak P_2 contributed to the anode. For cells 2-4, this part of the peak seemingly increases in height after ageing. The evolution of peaks with age is to typically become wider and less distinctive. This trend can be related to increased lithiation heterogeneity within the electrodes. [85]. As the cells age, the reaction and diffusion kinetics decline. This entails a risk for irregular lithium allocations which in turn evoke local degradation, such as lithium plating. The result is a reduced homogeneity of the lithium distribution throughout the cell which shows up as decreases in peak heights. This effect could contribute to the

fattening of discharge peak P_1, but the opposite is potentially the explanation for the behavior of peak P_2, where the peak height is seen to increase. Accordingly, the lithium distribution seems to have become more homogeneous.In addition to an increased homogeneous lithium deposition, one possible explanation to the increased peak height is that the voltage-capacity curve is easily susceptible to measurement noise, meaning that extracting DV and IC, especially in the flat voltage plateau region, is challenging to do accurately. This is further complicated by the fact that the tests performed after ageing for cells 1-4 used a different battery tester compared to at BoL. As all data was filtered with a constant ΔV, and the potential difference in data acquisition between cell testers were not considered in this step, additional measurement noise would therefore directly affect the DV and IC curve, and specifically the peak amplitude.

The spectra captured using EIS for cells 1-8 at 50 % SoC after ageing can be seen in Figure 4.15. The ECM used for the analysis is the same as previously used for the initial analysis, see Figure 4.17.

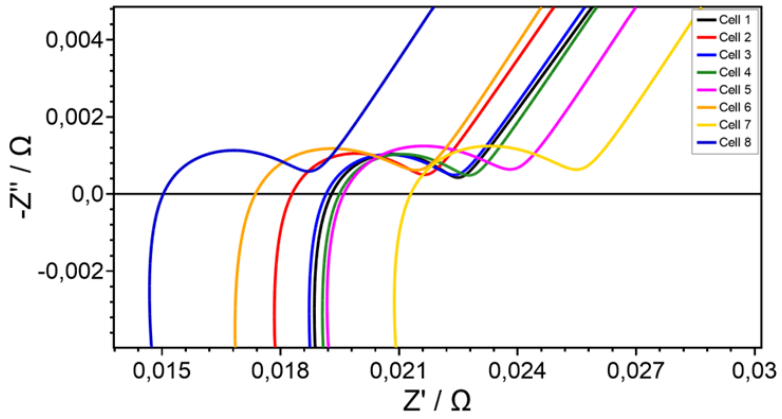

Figure 4.15: Nyquist plot showing cells 1-8 at 50 % SoC after ageing. The ECM used is the same as in the initial analysis.

Spectra in the form of Nyquist plots before and after ageing can be seen in Figure 4.16 for two cells at a time. The ohmic resistance, R_{ohm}, as well as combined resistance for the charge-transfer and the SEI, $R_{\text{CT/SEI}}$, for each cell before and after ageing can be seen in Table 4.2.

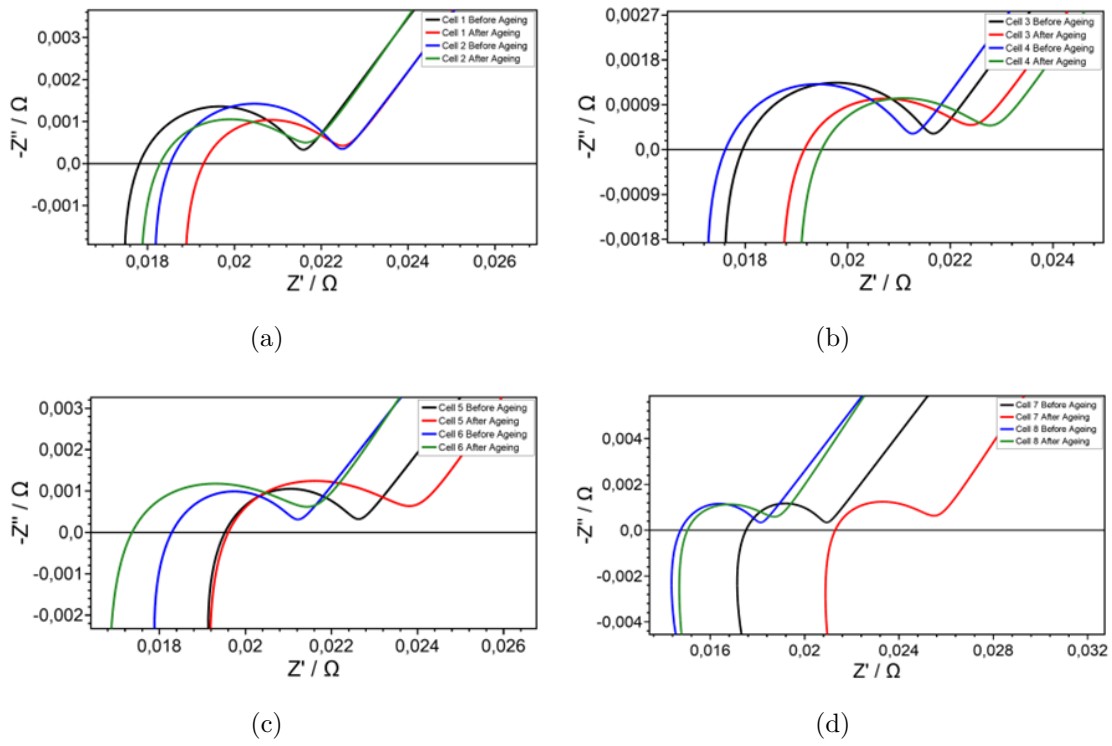

Figure 4.16: Nyquist plots for cells before and after ageing at 50 % SoC. a) displays cell 1 and 2, b) cell 3 and 4, c) cell 5 and 6 and, d) cells 7 and 8.

The most noteworthy change is the increase in $R_{\mathrm{CT/SEI}}$ for cells 5-7, indicating that LLI and possibly LAM have occurred. The reason why these cells display a marginal increase in $R_{\mathrm{CT/SEI}}$ is likely due to cells 5-8 being cycled in a wider SoC window, compared to cells 1-4. While there appears to be a small increase in ohmic resistance for some of the cells, there are uncertainties such as the inability to maintain an ideal setup and cell positions, as previously discussed in 4.1.4, making it impossible to draw any reliable conclusions. The fact that the capacity fade low, and the found degradation of the cells limited, further adds to the uncertainties.

Table 4.2: Ohmic resistance, R_{ohm}, and combined charge-transfer and SEI resistance, $R_{\text{CT/SEI}}$, presented for cells 1-8 before and after ageing at 50 % SoC.

	Cell	R_{Ohm} [mΩ]	$R_{\text{CT/SEI}}$ [mΩ]
Cell 1	Before Ageing	17.1	4.44
	After Ageing	18.4	4.13
Cell 2	Before Ageing	17.8	4.64
	After Ageing	17.3	4.41
Cell 3	Before Ageing	17.2	4.39
	After Ageing	18.3	4.23
Cell 4	Before Ageing	16.9	4.32
	After Ageing	18.6	4.27
Cell 5	Before Ageing	18.6	4.05
	After Ageing	18.5	5.50
Cell 6	Before Ageing	17.3	3.89
	After Ageing	16.1	5.56
Cell 7	Before Ageing	16.6	4.34
	After Ageing	20.2	5.45
Cell 8	Before Ageing	13.8	4.32
	After Ageing	14.2	4.64

The curve fitting of the results obtained from the EIS measurement allowed the determination of the ECM used in Figure 4.17. The ECM that was found to fit best to the cells characteristics is composed of a series of three sub-electrical-circuits, a resistor in parallel with an inductor; a resistor; and a resistor in series with a Constant Phase Element (CPE) and in parallel with a second CPE.

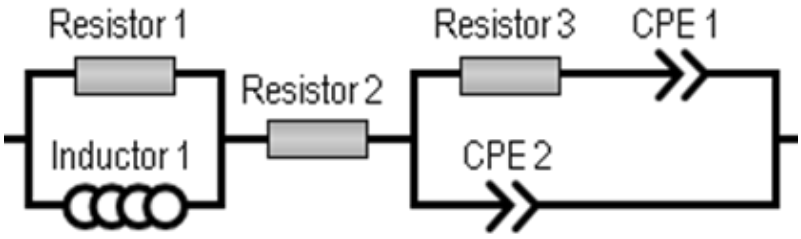

Figure 4.17: ECM used for the EIS analysis of Cells 1-8 as well as the reference cell.

Direct current internal resistance (DCIR) of battery cells varies depending on multiple factors, ranging from the battery materials to the operational conditions, and is directly related to the battery performance. The internal resistance is calculated

using Ohm's law, adapted into Equation 2.4, based on the voltage response to a 30 second charge and discharge pulse. This voltage response can be seen in Figure 4.18, before and after ageing for a change (a) and discharge pulse respectively (b).

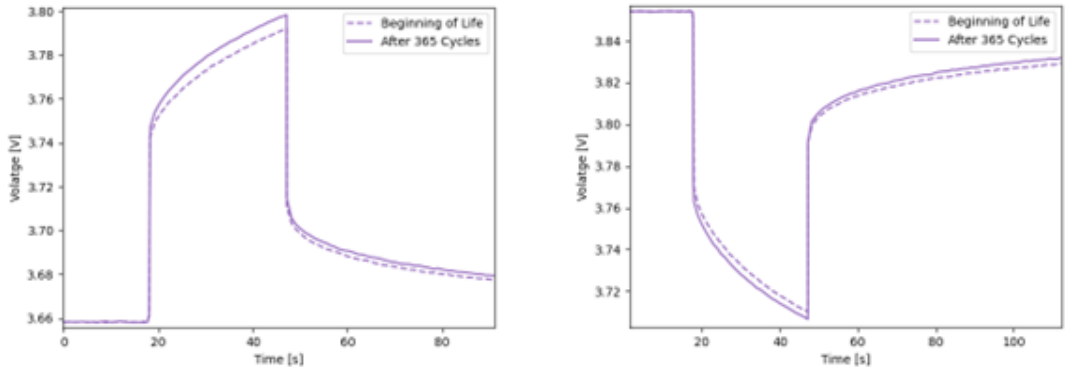

(a) (b)

Figure 4.18: Cell voltage [V] response to a 1C 30 second charge (a) and discharge (b) pulse current before and after 365 cycles.

Presented in Figure 4.19 is the dynamic resistive response for cell 5 during charge (a) and discharge (b) presented as a function of SoC. As the time of the response increases, a consistent monotonous rise in internal resistance is observed. Furthermore, a dependence on the SoC is noted. All time dependent processes, R_{2s} through R_{30s}, reaches a minimum at a SoC of between 30 % and 70 % for both fresh and aged cells. The minimum is slightly shifted towards higher SoC during charge compared to during discharge. This suggests that the underlying kinetic phenomena exhibit a more resistive behaviour as the cell approaches higher or lower SoC [86, 87]. This implies that the SoC impact the cell dynamic behaviour. At extreme SoC values, where the concentration of intercalated lithium is either very high or very low, even slight deviations from equilibrium can significantly impact the current-voltage characteristics of the cell. [88]. In addition, different reactions have different activation barriers, and likewise the charge-transfer will depend on the state of the charge.

The resistance experience a stronger SoC dependency with increasing time. It is expected that there is little change in the ohmic resistance during the charge phases [89, 90]. Hence, the polarization resistance is the main factor affecting the change in the total internal resistance. The same trend can be observed after ageing for all cells.

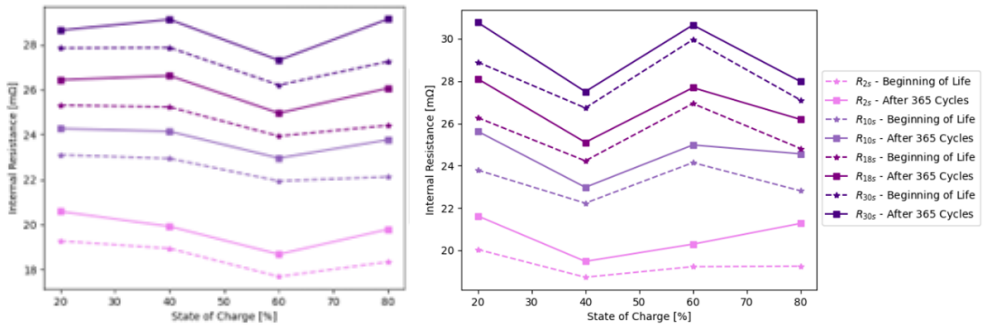

(a) (b)

Figure 4.19: Calculated internal resistance [mΩ] for cell 5 after 2 seconds, 10 seconds, 18 seconds and 30 seconds pulse duration during charge (a) and discharge (b), representing the different time-dependent electrochemical processes in cell 5 plotted against different states of charge.

A similar voltage response is seen in both charge and discharge pulses. The observed variations in resistance values could potentially be attributed to the differences in the energy required for deintercalation, from the positive electrode, and intercalation, into the negative electrode. These may differ from the reversed process, meaning the energy required for deintercalation from the negative electrode and intercalation into the positive electrode. It is possible that the disparity in energy is related to the observed difference in resistance during charge and discharge.

4.3.1 The Effect of Current Rate & SoC Window on the Cell Ageing

Two different charge current rates and SoC windows were used during cycling to potentially evoke different internal parameters. To achieve capacity regeneration, the underlying causes of ageing and the effect of different operational parameters must first be understood.

As discussed in Section 2.1.3, different operational parameters provokes different degradation mechanisms. Based on the SoH after 365 cycles, the total capacity lost indicated no correlation between capacity fade and the charge current rate. As cell degradation is an extremely complex phenomenon, relying on solely the capacity fade will not provide deeper insights in that regard however. To further deduce if the lost capacity originated from the same degradation mechanisms, or if the contribution of different degradation mechanisms resulted in the same total net capacity fade, the IC is further evaluated. This is presented in Figure 4.20, where cells cycled at 0.5C/1C and 0.7C/1C are compared for each of the SoC windows. For cells 2 and 3 cycled using a smaller SoC window, no distinction can be made regarding different amount of cell degradation as no distinction between the cell's curves in Figure 4.20a can be made. Both curves before and after ageing show a considerable overlap.

For cells 5 and 7 cycled with a slightly larger SoC window, a higher degree of LLI during discharge can be observed for cell 5 which was cycled with a higher charge current rate, see Figure 4.20b. This can be seen through a slight difference in peak high decrease and peak shift towards lower capacities for cell 5, as compared to cell 7. Seemingly, both cells experience the same amount of capacity fades of 3.18 % after ageing, but the degradation modes seemingly have been evoked to different degrees.

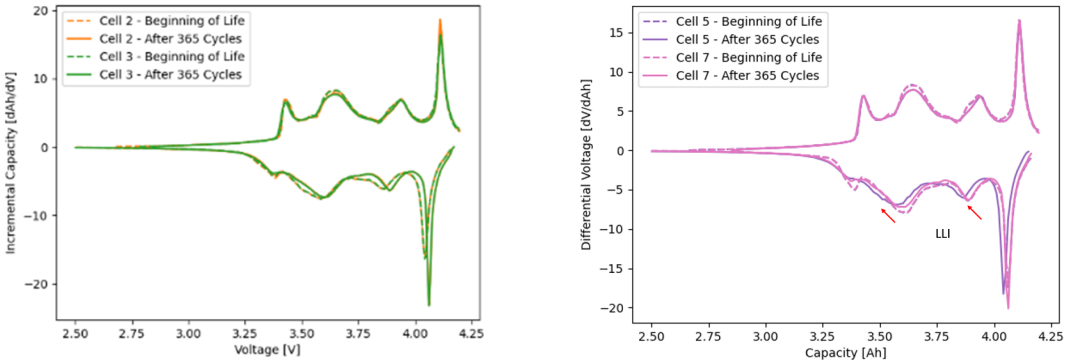

(a) (b)

Figure 4.20: Measured IC [dAh/dV] plotted against the voltage [V]. Charge and discharge before and after 365 cycles. (a) shows cell 2 cycled at 0.7C/1C and cell 3 cycled at 0.5C/1C while (b) shows cells 5 cycled at 0.7C/1C and cell 7 cycled at 0.5C/1C with a slightly increased SoC window. The identifiable curve changes due to ageing are marked and attributed to LLI.

When evaluating the degradation presented in Figure 4.20, the amount of cell degradation was seen to increase for the cells cycled at a larger SoC window combined with a larger charge current. As LLI partly represents the SEI later growth on the anode, the capacity lost due to LLI can be assumed to exhibit good linearity with increase in the current-rate, hence becoming the dominating degradation mode at this point of the cell life, whilst no conclusions can be drawn regarding the effect on LAM at this point. *Seo et al.* found a similar trend, where the amount of LLI exhibited a linear relationship with the current rate, whilst a non-linear relationship was observed for the LAM.

Although the current rate is considered one of the major cause of cell degradation, the obtained results after cycle ageing indicated minor current rate dependency. Since cell degradation is complex, many factors could have contributed to this. However, a likely cause could be due to the fact that the cells were not degraded enough, thereby not being able to exhibit the difference in degradation yet, as the cells are still far from the conventionally considered EoL. However, it is important to keep in mind that the cause could be more complex, and potentially related to the cell composition and chemistry.

From the differential analysis it is seen that LAM_{NE} dominates over LAM_{PE} in terms of a underlying degradation mode for the aged cells. The graphite signature is found to become less defined after cycling. This behavior is partly indicative of potential structural changes of the graphite staging. This is an expected behavior for cells comprised of a graphite anode, as graphite material loss is usually accelerated by high discharge rates, compared to positive electrode losses which exhibit a more moderate loss for all rates [91]. In addition, the dominating loss of anode active material could supposedly further be influenced by structural disordering due the cells being discharged to very low SoC during the cycling.

Generally, different degradation mechanisms are partly dominating either during the linear or nonlinear part of cell ageing. It is assumed that in the linear degradation domain which occurs during the early stages of ageing, as the cells adhered to throughout the thesis, consumption of lithium-ions is mainly attributed due to SEI growth. Additionally, at this stage, cells containing silicon additives suffer from a higher risk of SEI cracking, and consequently subsequent formation, which is due to their large volume expansion during operation. The other main mechanisms causing LLI, namely lithium plating, is generally observed during the later, non-linear, stages of ageing. As the ageing progresses, the continuous volume expansions can contribute to excessive cracking, thereby extruding debris, posing high chance of forming i-Li [92]. Based on this, the ageing procedure, current rates, and the number of cycles have a strong influence on the evoked degradation modes and mechanisms. Consequently, when designing the regeneration procedure this should be kept in mind.

When comparing the cells aged at different charging rates using EIS results, a trend regarding the ohmic resistance can be observed, see Figure 4.21 and Table 4.2. All cells aged at a charging rate of 0.5C show an increase in ohmic resistance whereas the cells aged at a charging rate of 0.7C exhibit a decrease. The exception is cell 1, but since it is an outlier and has aged significantly more than all other cells it cannot be used when comparing the cells side-by-side. However, the uncertainties present when analyzing the ohmic resistance can not be neglected, and it is therefore not possible to draw any conclusions from this observation alone. However, when instead looking at the different sets of cells cycles at different SoC windows, meaning cells 2-4 compared to cells 5-8, a significant increase in charge transfer and SEI resistance can be observed for cell 5-8. This observation suggests increased LLI for the cells cycled at a slightly larger SoC window, which could be due to an increased SEI layer, as previously discussed.

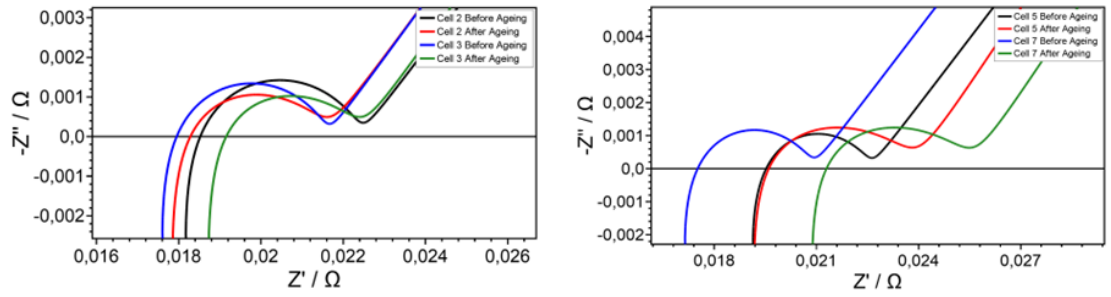

(a) (b)

Figure 4.21: Nyquist plots of cells aged at different charging rates, before and after ageing. The spectra were captured at 50 % SoC and shows cells 2 and 3 (a), which were aged with a smaller SoC window, and cells 5 and 7 (b), which were aged with a larger SoC window.

Opposed to the comparison done using DVA, ICA and EIS, the DCIR analysis indicate that different charge current rates affect the cell degradation. When comparing the internal resistance between cells aged at 0.5C/1C and 0.7C/1C, the internal resistance generally exhibits a larger increase after being aged with the slower charge current rate. Figure 4.22 illustrates a comparison between cell 5 and cell 6, cycled at 0.7C/1C and 0.5C/1C respectively. The increase in internal resistance could potentially be explained by the correlation between the current rate and temperature, as the internal resistance is significantly affected by the temperature [89]. When the cell's internal temperature rises, the internal resistance decreases. A higher current rate generates more heat, thus cycling with a higher current rate potentially slows down the resistance evolution, explaining the observed trend in Figure 4.22. This effect could explain how cell 5 still exhibited the same capacity fade as cell 7, whilst results indicated that cell 5 lost a higher amount of lithium inventory compared to cell 7, as seen in Figure 4.20b [90, 92].

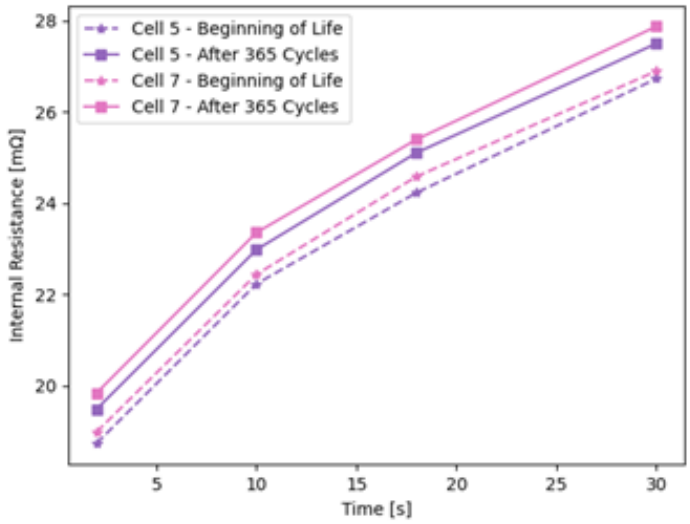

Figure 4.22: The calculated internal resistance [mΩ] with time [s] for cell 5 cycled at 0.7C/1C and cell 7 cycled at 0.5C/1C before and after 365 cycles as a response to a charge current pulse at 40 % SoC.

When analyzing the DCIR of the cells, the choice of battery tester was found to have a non-negligible influence on the measurements. As the used battery tester was interchanged between initial characterization, ageing, and regeneration for some of the cells the DCIR will be neglected from this point onward. This also includes the relaxation pulses implemented in the cycle ageing procedure as not all cells were cycled using the same battery tester, hence complicating the comparison.

4.3.2 The Effect of Storing the Cells After Cycling

Cells 4 and 6, not used for regeneration, were stored at room temperature after cycling was completed. As cell degradation is partly reversible, to fully quantify the extent of the regeneration procedures and to compare them to non-regenerated cells, stored cells are used as a reference. The purpose is to distinguish the effect of different parameters used during regeneration from the possible regain in the capacity as a result of resting.

Cells 4 and 6, cycled at 0.5C/1C and 0.7C/1C lost 10 and 40 mAh respectively during storage. The cells were stored directly after ageing for upwards of 8 weeks, during the same time frame in which cells 2,3 and 5 were regenerated.

To further analyze the effects of storage after ageing and to evaluate the reversibility of the detected cell degradation, DVA and ICA were used. Presented in Figure 4.23 and 4.24 is the discharge DV and IC curves for cells 4 and 6, comparing observations made before ageing, after ageing, and after storage. No shift of the peaks can be observed for either cell, indicating that no additional LLI has taken place. However, the height of the second discharge peak seemingly increases with the number of

cycles, and becomes even sharper after the subsequent storage. The same behaviour is partly observed for the third discharge peak. Both peaks are attributed to the anode.

Similar peak sharpening has been observed in other studies, providing two plausible explanations. The first reasonable cause for this phenomenon could be the homogeneity of lithium distribution [93]. Through relaxation, the cell's local potential in the anode and cathode active materials impacts the lithium distribution. During the charging and discharging processes in the RPT after storage, the distribution of lithium within the cell adjusts and potentially becomes more uniform as the cell undergoes the slow cycling [94]. Secondly, the homogeneous lithium distribution could possibly be due to the anode overhang effect. Another study claims that the peak sharpening is not related to the lithium distribution, but instead related to the intercalation content of the graphite anode, which in turn is influenced by the anode overhang commonly occurring during storage [95].

In addition to peak sharpening, the valley depth between discharge peak 3 and the end-of-curve is seen to increase. Contrary to LAM, defined by valley depth decrease, this would indicate regain of active material at the anode. The anode overhang effect could be hypothesized to be the reason for the gain of anode active material. However, there are uncertainties regarding the peak amplitude, as it is affected by multiple factors. Since some measurements were acquired using different battery testers, which acquires data differently, even if the same filter is applied, a noisier measurement reading would have a big impact on the derivative, meaning the DV and IC peaks.

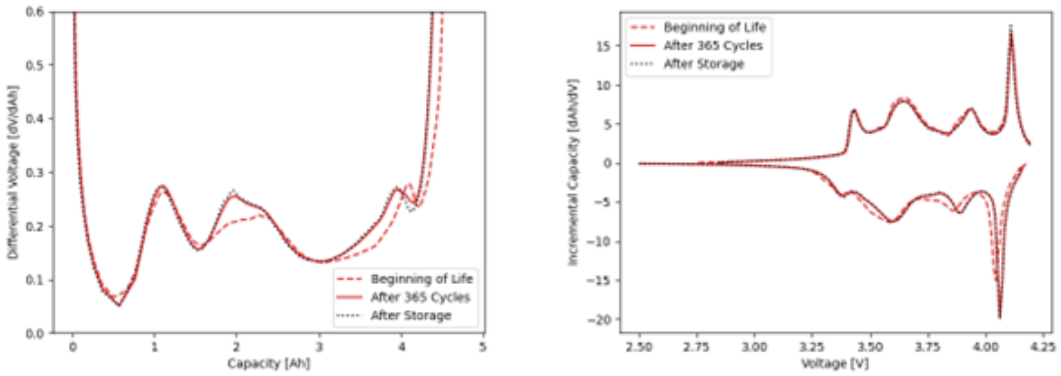

(a) (b)

Figure 4.23: Measured DV [dV/dAh] plotted against discharge capacity [Ah] (a) and IC [dAh/dV] plotted against voltage [V] for cell 4 at BoL, after 365 cycles and after subsequent storage.

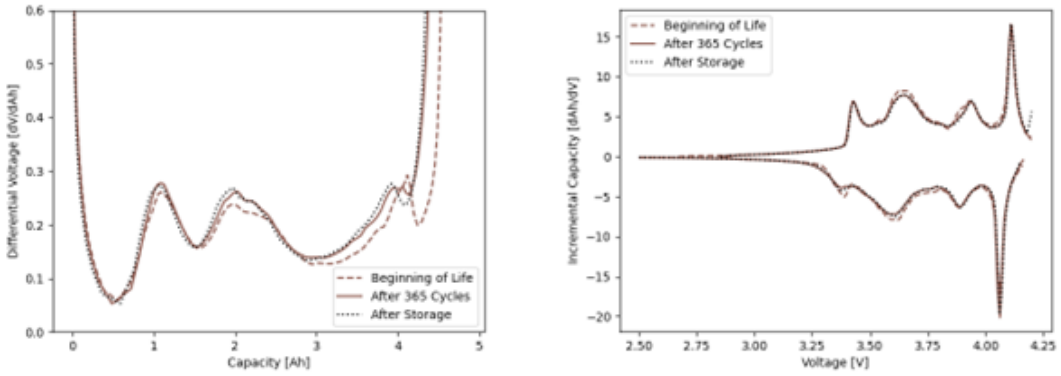

(a) (b)

Figure 4.24: Measured DV [dV/dAh] plotted against discharge capacity [Ah] (a) and IC [dAh/dV] plotted against voltage [V] for cell 6 at BoL, after 365 cycles and after subsequent storage.

4.4 Regeneration

For the purpose of regenerating lost capacity during cycle ageing, three different procedures were developed. The first approach targeted i-Li, the second aimed at dissolving lithium-ions that have crystallized or partaken in unwanted side-reactions, including SEI growth, and the third one constituted a combination of the two approaches. Through different means, all three approaches intend to regain capacity by targeting LLI, or more specifically lithium plating and SEI growth.

4.4.1 Approach 1 - Reconnection of i-Li

The aim of Approach 1 was to target i-Li by first implementing a fast-stripping step, followed by a slow discharge that could result in the reconnection of the electronically isolated and stripped-off lithium islands. A total of 52 cycles were completed on cell 2, but no regain in capacity is seen after regeneration. Instead, a further capacity fade of 50 mAh is observed.

The DV curve for cell 2 exhibited the most distinguishable changes and is presented in Figure 4.25. The small capacity fade promoted marginal changes in the DV curve after regeneration compared to after cycling. An indication towards LLI can be assumed by a slight shift of the endpoint of the curve towards lower capacities. A more notable change is observed for discharge peak P_1, contributed from the anode, and the valley corresponding to the IC peak P_1. The area of interest is highlighted in Figure 4.25 (a) and (b) shows a zoomed-in version of said area where the notable changes are marked. It is observed how the valley is decreasing in depth towards the initial depth at BoL. This change indicates that active material could have been recovered, and the anode thereby regained some of its storage capability.

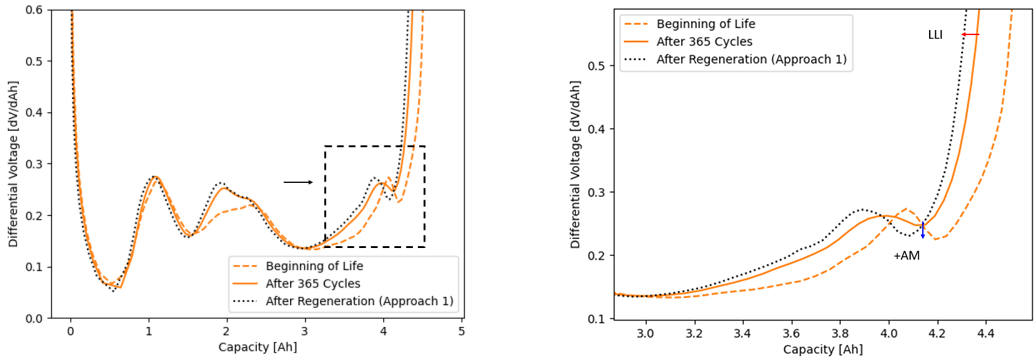

(a) (b)

Figure 4.25: Measured DV [dV/dAh] plotted against the discharge capacity [Ah] at BoL, after 365 cycles and after regeneration using Approach 1 for cell 2. In (b) a zoomed in version of the highlighted area in (a) can be seen, where the notable changes after regeneration have been marked.

A Nyquist plot for cell 2 at BoL, after cycling and after regeneration at 50 % SoC can be seen in Figure 4.26.

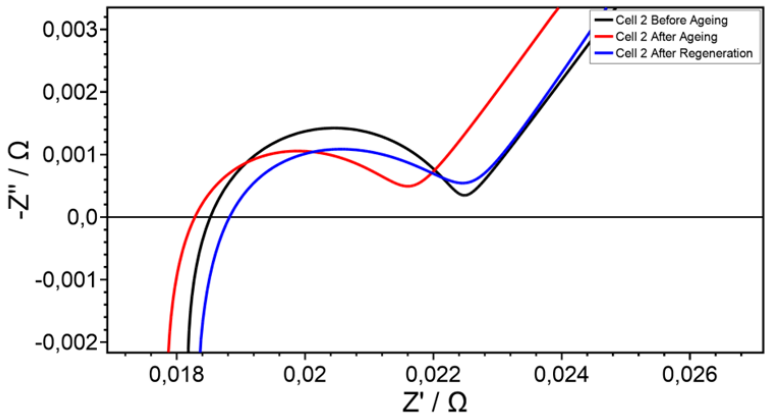

Figure 4.26: Nyquist plot for cell 2 at BoL, after 365 cycles and after regeneration using Approach 1 at 50 % SoC.

Table 4.3 shows the ohmic resistance as well as charge-transfer/SEI resistance corresponding to Figure 4.26. The ECM used remains the same, see Figure 4.17.

Table 4.3: Ohmic resistance, R_{Ohm}, and combined charge-transfer and SEI resistance, $R_{\text{CT/SEI}}$, are presented for cell 2 at BoL, after 365 cycles and after regeneration using Approach 1 at 50 % SoC.

Cell 2	R_{Ohm} [mΩ]	$R_{\text{CT/SEI}}$ [mΩ]
Before Ageing	17.8	4.64
After Ageing	17.3	4.41
After Regeneration	17.7	4.95

The results from EIS show a small increase in charge-transfer/SEI resistance, which could indicate that further LLI has occurred. Unfortunately, as previously mentioned, the ohmic resistance does not provide any additional information due to the uncertainties surrounding the tests.

Although the main target of the approach was i-Li, the DVA/ICA analysis indicate that some recovery of anode active material has occurred. However, no such indication of recovery is present when looking at the lithium inventory. Instead, DVA shows a shift in the curve and EIS an increase in charge-transfer/SEI resistance, both indicating further LLI. It is likely that there was not enough lithium plating occurring, resulting in little to none i-Li to recover for the approach to be successful. Further studies on more degraded cells are needed.

4.4.2 Approach 2 - Pulsing

Approach 2 was inspired by the method of desulfurization used to regenerate lead-acid batteries. By applying short pulses, just enough energy to dissolve lithium-ions from potential crystals or SEI would be applied without harming the cell. To find the optimal pulse procedure capable of this, different parameters such as the number of pulses, pulse duration, and amplitude were explored. Between all iterations, the capacity gain per pulse was calculated. If the cell was regenerated, the coulombic efficiency of the cell would increase and hence the amount of capacity gained per pulse would increase as well. A total of 48 iterations were performed, but some iterations at 80 % SoC were unable to be completed due to the voltage increasing above the limit of 4.2 V. However, no iteration indicated any influence on capacity gain, and no capacity regeneration could be observed at the end of the iterations. Instead a capacity fade of 20 mAh was observed. Since the capacity fade after ageing is still relatively low, it is unclear if this is a result of the parameter choices or if the cells simply needed to be aged further to observe capacity regeneration through this method.

Similar to Approach 1, the same trend is observed using differential analysis where indications of LLI are seen. In addition, Approach 2 appears to also result in regained active material at the anode as seen in Figure 4.27 (a) and marked in Figure 4.27 (b). However, the procedure were only applied during the daytime and the cell was at rest during the night. After storage, recall Figures 4.23 and 4.24, the same regain

of anode active material was observed, which could be due to the anode overhang effect. It is therefore also possible that the anode overhang effect could be a reason as to why cells 3 shows a regain in anode active materials.

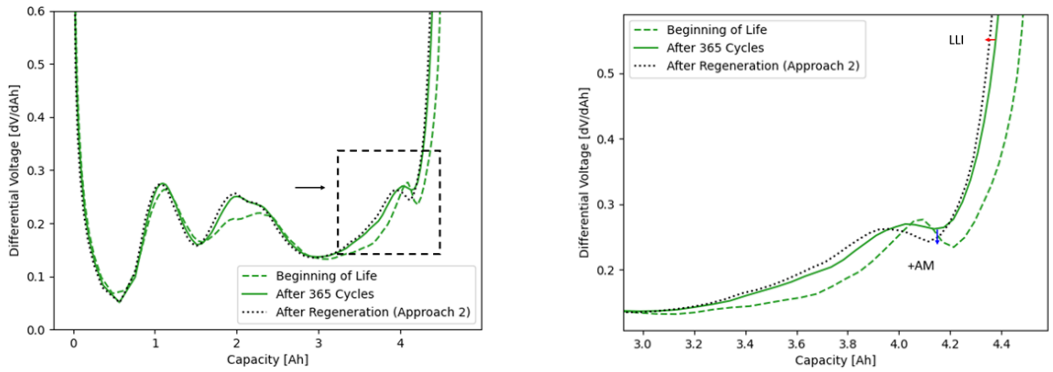

(a) (b)

Figure 4.27: Measured DV [dV/dAh] plotted against the discharge capacity [Ah] at BoL, after 365 cycles and after regeneration using Approach 2 for cell 3. In (b) a zoomed in version of the highlighted area in (a) can be seen, where the notable changes after regeneration have been marked.

Figure 4.28 shows the Nyquist plots for cell 3 at BoL, after ageing as well as after regeneration. The spectra were captured at 50 % SoC, and the corresponding ohmic and charge-transfer/SEI resistance can be seen in Table 4.4. The ECM used remained the same.

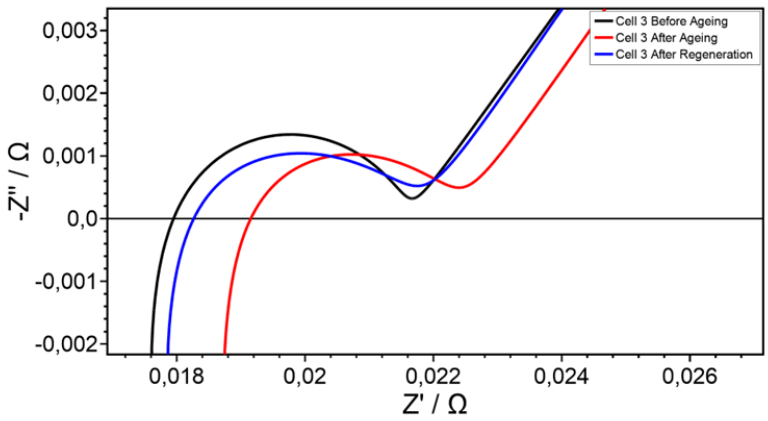

Figure 4.28: Nyquist plot for cell 3 at BoL, after 365 cycles and after regeneration using Approach 2 at 50 % SoC.

Table 4.4: Ohmic resistance, R_{Ohm}, and combined charge transfer and SEI resistance, $R_{\text{CT/SEI}}$, are presented for cell 3 at BoL, after 365 cycles and after regeneration using Approach 2 at 50 % SoC.

Cell 3	R_{Ohm} [mΩ]	$R_{\text{CT/SEI}}$ [mΩ]
Before Ageing	17.2	4.39
After Ageing	18.3	4.23
After Regeneration	17.2	4.69

A minor increase in charge transfer/SEI resistance can be seen from the EIS, which could indicate that some LLI has taken place. This corresponds to what was previously observed in the DVA. As in Approach 1, the results indicate that no regeneration has taken place, and instead ,the cell has kept ageing resulting in both further capacity fade and LLI.

4.4.3 Approach 3 - Combination of Approach 1 & Approach 2

Approach 3 aimed to combine the different features of Approaches 1 and 2. By utilizing the dissolution of lithium compounds and SEI with stripping of plated lithium, more lithium-ions can potentially be recovered/reconnected. Due to time restrictions a fractional factorial design was used to reduce 48 iterations down to 16. As in Approach 2, some iterations at 80 % SoC were unable to be completed due to the voltage exceeding the maximum. As with Approach 2, no increase in capacity gain from the pulses was seen throughout the regeneration. Instead, after the regeneration was completed an additional capacity fade of 50 mAh was observed.

Figure 4.29 presents the obtained DV curves at BoL, after ageing, and after regeneration. Similarly to Approaches 1 and 2, the low capacity fade evoked no major changes. However, compared to the discharge DV curve after regeneration for Approach 1 and 2, a shift towards higher capacities is observed for Approach 3. This indicates a partial regain of the lost lithium inventory after regeneration as compared to after ageing. Cell 5 also shows signs of recovered active anode material, represented by the valley depth increase seen in 4.29 (b). The same hypothesis as with Approach 2 is suggested here, regarding the anode overhang effect, as there was a longer rest period between ageing and the start of regeneration.

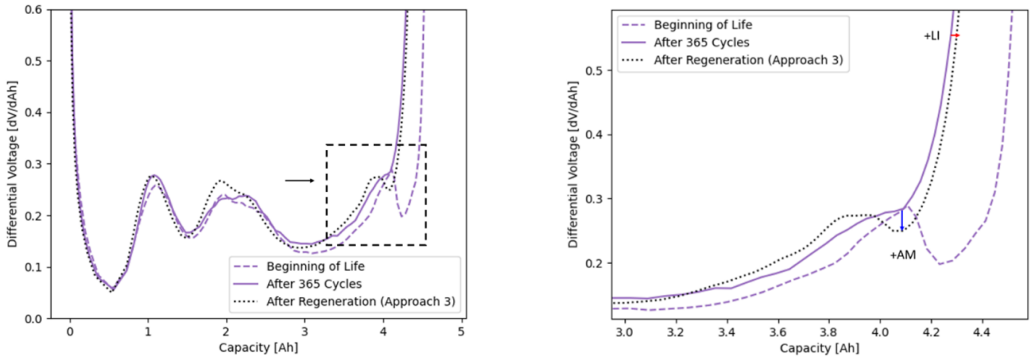

(a) (b)

Figure 4.29: Measured DV [dV/dAh] plotted against the discharge capacity [Ah] at BoL, after 366 cycles and after regeneration using Approach 3 for cell 5. In (b) a zoomed in version of the highlighted area in (a) can be seen, where the notable changes after regeneration have been marked.

The EIS results for cell 5 is shown in Figure 4.30, where Nyquist plots for before ageing, after ageing as well as after regeneration are displayed. The spectra were captured at 50 % SoC, and the corresponding ohmic and charge-transfer/SEI resistance can be seen in Table 4.5. The ECM used remained the same.

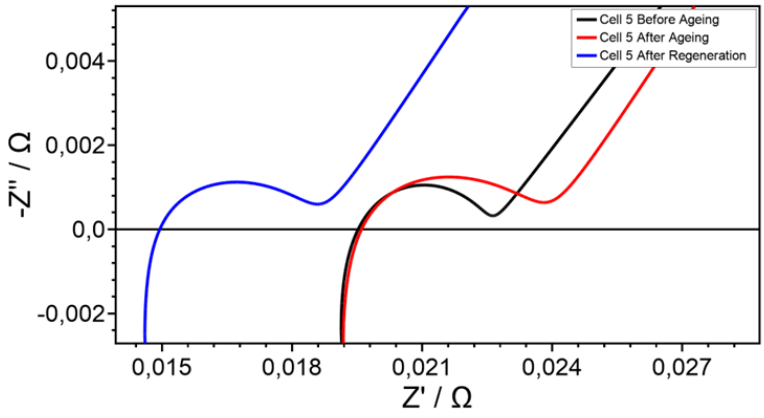

Figure 4.30: Nyquist plot of cell 5 at BoL, after 366 cycles and after regeneration using Approach 3 at 50 % SoC.

Table 4.5: Ohmic resistance, R_{Ohm}, and combined charge transfer and SEI resistance, $R_{\text{CT/SEI}}$, are presented for cell 5 at BoL, after 366 cycles and after regeneration using Approach 3 at 50 % SoC.

Cell 3	R_{Ohm} [mΩ]	$R_{\text{CT/SEI}}$ [mΩ]
Before Ageing	18.6	4.05
After Ageing	18.5	5.50
After Regeneration	14.2	4.57

The EIS results indicate a significant decrease in charge-transfer/SEI resistance, which suggests that recovery of lithium inventory has taken place. This observation corresponds with what was observed in the DVA. While a large, and interesting, decrease in ohmic resistance seems to have taken place, it is not possible to draw any conclusion due to the previously discussed uncertainties.

Indications of lithium inventory recovery can be found. The DVA shows a slight shift towards higher capacities when compared to the corresponding DVA after ageing, and the EIS shows a decrease in charge transfer/SEI resistance. Both of these factors speak in favour of a possible lithium inventory recovery potentially enabled by the combination of the approaches. While recovery is indicated, it is important to remember that the capacity fade is still relatively low, and further studies on more degraded cells are needed to confirm these results.

4.4.4 Comparison of the Regeneration Approaches

Presented in Table 4.1 is the discharge capacity measured after regeneration relative to the capacity measured after ageing (ΔQ). From the capacity, it can be concluded that all three methods resulted in a capacity fade.

Table 4.6: Measured discharge capacity after regeneration relative to after ageing for cells 2, 3, and 5 regenerated using Approaches 1, 2, and 3, respectively.

Cell Number	Regeneration Approach	ΔQ
2	1	-50 mAh
3	2	-20 mAh
5	3	-50 mAh

Furthermore, all three approaches, as well as the cells analyzed after storage, shows indications of active material recovery. The most probable reason across the board appears to be the anode overhang effect. Only cell 5 targeted by Approach 3 showed indications of lithium inventory being regained, which could be due to it being cycled at a wider SoC window, as compared to cells 2 and 3, and thereby achieving slightly larger capacity fade. While interesting, it is important to note that no capacity regeneration was observed for either cell in the end. Regardless, with such a low

capacity fade for all cells, it is very difficult to ascertain that any form of regain or regeneration has taken place. It is also important to recall that various cell chemistries will degrade differently and during different time frames, which need to be taken into account. Therefore, while Approach 3 shows promising indications, further studies are needed on more degraded cells to verify all three approaches.

5

Conclusion

Throughout this thesis, a range of different techniques have been explored for the investigation of performance and degradation in LIB cells. With the use of differential analysis and electrochemical impedance spectroscopy, an understanding of the electrochemical reactions occurring during cycle ageing were gained and later identified, in order to obtain qualitative and quantitative conclusions regarding degradation mechanisms and modes on which the design of regeneration procedures could be based on.

5.1 Conclusions from the Results

To interpret the results from the initial characterization, an understanding of the underlying electrochemistry is necessary, and the feature analysis is highly chemistry specific. From a comparison with earlier studies, the characterization revealed that the cells were likely composed of NMC/Si-G chemistry with a high nickel content, and most likely low silicon content. In addition to the cell chemistry, the operational parameters during ageing will have a large impact on the prompted cell degradation. For the experimental work, the effect of two different charge current rates and SoC windows were evaluated.

After approximately 365 cycles, all cells exhibited an average capacity fade of 2.94 %. While no difference in capacity fade could be seen between the cells cycled at difference charging rates, a larger capacity fade was observed for cells cycled with a higher SoC window. The large difference in effect between the stress factors could be explained by the cell chemistry. With the suspicion of silicon addition to the graphite, and the knowledge that Si-G compound anodes suffer from excessive volume expansions during intercalation/deintercalation, this might increase the risk of LAM_{NE}, and further on LLI as a result of cracking and new SEI formation. In addition, the DVA and ICA indicated the presence of mainly LAM_{NE} and LLI after cycling for all cells. The cells cycled with a higher SoC window exhibited a larger fraction of LAM_{NE} and LLI as well as an increase in the charge-transfer/SEI resistance obtained from EIS. Only for these cells could a marginal difference between the amount of degradation and charge current rates be seen whilst the net capacity fade showed no such indications. Moreover, both for the internal resistance and the charge-transfer/SEI resistance, a SoC dependency was found. The dependency

is very complex, as it depends on the intricate nature of an electrochemical cell, but different electrochemical processes and phase transformations are more or less resistive at different SoC.

Three regenerative approaches were then explored which aimed to recover the capacity lost during cycle ageing. Approach 1 aimed at reconnecting i-Li, Approach 2 at dissolving crystallized lithium-ions or lithium-ions consumed by the SEI formation/growth, and the third, Approach 3, utilized a combination of the approaches. Consequently, one of the first prerequisites for this type of regeneration would be that the aged cells suffer from LLI. After ageing, LLI was indeed observed, together with LAM. However due to the marginal capacity fade, and the visually similar fraction of LAM and LLI, the capacity lost to LLI is small. Moreover, as no *post-mortem* analysis was performed before the cells were regenerated, the potential existence, or amount, of plated lithium or i-Li is unknown before and after regeneration.

All regeneration approaches exhibited an indication of potential recovery of anode active material. However, due to the implementation of longer rest periods in Approach 2 and 3, this cannot be attributed to only the regeneration since a similar gain in anode active material was seen for cells kept in storage during the same time frame. Nonetheless, it is possible that the gain of anode active material can be tied to the anode overhang effect.

After Approach 1 and 2, an additional loss of lithium inventory was exhibited, whilst a potential recovery was observed after Approach 3. As the amount of degradation after cycling was low, it can only be speculated that when trying to reconnect both i-Li and the dissolved lithium-ions, the chances of regaining lithium inventory is increased. At this step, though different operational parameters were tested, no conclusions can be drawn regarding which parameter was most influential on the result.

In general, though some gain of anode active material was observed, all approaches resulted in a small capacity fade of 50 mAh, 20 mAh, and 50 mAh respectively. It is possible that the pulses alone has had a lesser effect on the ageing of cell 3, as compared to cells 2 and 5. Regarding their effect on regeneration, no conclusion can be drawn at this stage as further studies are needed on more degraded cells.

5.2 Method Development

To draw further, and more certain, conclusions, the experimental procedure and choice of analytical tools need future development. As mentioned, the lack of *post-mortem* analysis limited the analysis of both cell degradation and the effects of regeneration. This addition would provide some essential insight to the material characteristics of the cells. The differential analysis would be more accurate with the addition of half-cell measurements. This would provide valuable information regarding the ageing of the individual cells as the observed peaks could be correlated to the individual electrodes. Likewise, other analytical tools such as voltage relaxation and impedance tracking could be useful for obtaining additional information

relating to lithium plating.

The uncertainties of the results are also correlated to variations of extrinsic parameters. Throughout the experiments, both battery testers and occasionally cell holders were interchanged or switched. For sensitive measurement techniques such as EIS, DCIR, DVA and ICA, these types of changes largely influence measurement. The quality of the results would have benefited from repeating these tests, where an idea of the potential error could be gained.

5.3 Future Studies

There are many factors which potentially influence the results, making it harder to draw any solid conclusions. The first and most prominent of these is the fact that the capacity fade is still relatively low. There are also uncertainties in terms of outside interferences, data filtering and the lack of *post-mortem* analysis, making it hard to verify the observed cell behavior. Furthermore, while the regeneration approaches were designed with the idea of investigating a general regeneration technique in mind, the cell chemistry can not be easily neglected. Together with the fact that the cycle ageing did not degrade the cells as much as expected, it is likely that the regenerative approaches did not target an area which was significantly provoked in terms of degradation mechanisms. While these techniques show some promise, they need to be further evaluated in future studies.

Indications of SoC having a big impact on cell degradation was observed. To draw further conclusions regarding the effect of SoC and SoC window, additional tests need to be performed. This is true in general, for future studies the interplay between cell chemistry, degradation mechanisms and impact of both cycling and regeneration operational parameter needs to be further evaluated.

In addition to further development of the methods proposed, some additional measurements could prove interesting for future studies. As part of the regeneration aims at regaining lithium-ions through the implementation of high-energy pulses, if the SEI was damaged during said pulses, a new SEI layer would form during the subsequent cycling, thereby consuming lithium-ions.

The final future goal of developing a non-invasive regeneration procedure is for it to be implemented into the battery management system of EVs. The battery management system would detect degradation happening in the LIB cells, which in theory could be regenerated when needed, *e.g.* during nighttime or when the EV is not in use, thereby extending the lifetime.

Bibliography

[1] IEA, *World Energy Outlook 2022*, 2022. [Online]. Available: https://www.iea.org/reports/world-energy-outlook-2022.

[2] ATA, *Economics and Industry Data*, 2023. [Online]. Available: https://www.trucking.org/economics-and-industry-data.

[3] EC, "Directive 2007/64/EC of the European Parliament and of the Council," *Fundamental Texts On European Private Law*, vol. 58, no. September 2006, pp. 1–28, 2020. DOI: 10.5040/9781782258674.0026.

[4] European Comission, "Regulation of the European Parliament and of the Council concerning batteries and waste batteries, repealing. Directive 2006/66/EC and amending Regulation (EU) No 2019/1020," in *European Commission*, vol. 0353, 2020. [Online]. Available: https://eur-lex.europa.eu/legal-content/EN/TXT/PDF/?uri=CELEX:52020PC0798.

[5] J. Dow, *Tesla cofounder's Redwood shows 95 % efficiency in battery recycling pilot*, 2023. [Online]. Available: https://electrek.co/2023/03/02/tesla-cofounders-redwood-shows-95-efficiency-in-battery-recycling-pilot/.

[6] R. B. Cooper, "Pulse Charging Lead-Acid Batteries to Improve Performance and Reverse the Effects of Sulfation," Ph.D. dissertation. [Online]. Available: https://researchrepository.wvu.edu/cgi/viewcontent.cgi?article=2226&context=etd.

[7] S. Schilling, *Ensuring Lead-Acid Battery Performance With Pulse Technology*, 1999. [Online]. Available: https://www.pulsetech.net/media/wysiwyg/Pulsetech/etc/SAEPaper-for-web.pdf.

[8] X. Huang, Y. Li, A. B. Acharya, X. Sui, J. Meng, R. Teodorescu, and D.-I. Stroe, "A Review of Pulsed Current Technique for Lithium-ion Batteries," *Energies*, vol. 13, no. 10, 2020, ISSN: 1996-1073. DOI: 10.3390/en13102458.

[9] C. Jin, T. Liu, O. Sheng, M. Li, T. Liu, Y. Yuan, J. Nai, Z. Ju, W. Zhang, Y. Liu, Y. Wang, Z. Lin, J. Lu, and X. Tao, "Rejuvenating dead lithium supply in lithium metal anodes by iodine redox," *Nature Energy*, vol. 6, no. 4, pp. 378–387, 2021, ISSN: 2058-7546. DOI: 10.1038/s41560-021-00789-7.

[10] F. Liu, R. Xu, Y. Wu, D. T. Boyle, A. Yang, J. Xu, Y. Zhu, Y. Ye, Z. Yu, Z. Zhang, X. Xiao, W. Huang, H. Wang, H. Chen, and Y. Cui, "Dynamic spatial progression of isolated lithium during battery operations," *Nature*, vol. 600, no. 7890, pp. 659–663, 2021, ISSN: 1476-4687. DOI: 10.1038/s41586-021-04168-w.

[11] X. Wu, K. Song, X. Zhang, N. Hu, L. Li, W. Li, L. Zhang, and H. Zhang, "Safety Issues in Lithium Ion Batteries: Materials and Cell Design," *Frontiers in Energy Research*, vol. 7, Jul. 2019, ISSN: 2296-598X. DOI: 10.3389/fenrg.2019.00065. [Online]. Available: https://doi.org/10.3389/fenrg.2019.00065.

[12] M. Laipan, L. Xiang, J. Yu, B. R. Martin, R. Zhu, J. Zhu, H. He, A. Clearfield, and L. Sun, "Layered intercalation compounds: Mechanisms, new methodologies, and advanced applications," *Progress in Materials Science*, vol. 109, p. 100 631, 2020, ISSN: 0079-6425. DOI: https://doi.org/10.1016/j.pmatsci.2019.100631.

[13] J. Gao, S.-Q. Shi, and H. Li, "Brief overview of electrochemical potential in lithium ion batteries," *Chinese Physics B*, vol. 25, no. 1, p. 018 210, Jan. 2016, ISSN: 1674-1056. DOI: 10.1088/1674-1056/25/1/018210.

[14] E. Moyassari, L. Streck, N. Paul, M. Trunk, R. Neagu, C.-C. Chang, S.-C. Hou, B. Märkisch, R. Gilles, and A. Jossen, "Impact of Silicon Content within Silicon-Graphite Anodes on Performance and Li Concentration Profiles of Li-Ion Cells using Neutron Depth Profiling," *Journal of The Electrochemical Society*, vol. 168, no. 2, p. 20 519, Feb. 2021. DOI: 10.1149/1945-7111/abe1db.

[15] N. Nitta, F. Wu, J. T. Lee, and G. Yushin, "Li-ion battery materials: present and future," *Materials Today*, vol. 18, no. 5, pp. 252–264, 2015, ISSN: 1369-7021. DOI: https://doi.org/10.1016/j.mattod.2014.10.040.

[16] R. C. Massé, C. Liu, Y. Li, L. Mai, and G. Cao, "Energy storage through intercalation reactions: electrodes for rechargeable batteries," *National Science Review*, vol. 4, no. 1, pp. 26–53, 2016, ISSN: 2095-5138. DOI: 10.1093/nsr/nww093.

[17] A. Casimir, H. Zhang, O. Ogoke, J. C. Amine, J. Lu, and G. Wu, "Silicon-based anodes for lithium-ion batteries: Effectiveness of materials synthesis and electrode preparation," *Nano Energy*, vol. 27, pp. 359–376, 2016, ISSN: 2211-2855. DOI: https://doi.org/10.1016/j.nanoen.2016.07.023.

[18] Q. Zhao, Y. Zhang, Y. Meng, Y. Wang, J. Ou, Y. Guo, and D. Xiao, "Phytic acid derived LiFePO4 beyond theoretical capacity as high-energy density cathode for lithium ion battery," *Nano Energy*, vol. 34, pp. 408–420, 2017, ISSN: 2211-2855. DOI: https://doi.org/10.1016/j.nanoen.2017.03.006.

[19] S. Bruno, K. M. Abraham, W. A. van Schalkwijk, and J. Hassoun, *Lithium Batteries - Advanced Technologies and Applications*, 1st ed. John Wiley & Sons, 2013, pp. 1–20, ISBN: 978-1-118-18365-6. [Online]. Available: https://app.knovel.com/hotlink/khtml/id:kt011BT4G2/lithium-batteries-advanced/concluding-remarks.

[20] Z. Chen, D. L. Danilov, L. H. J. Raijmakers, K. Chayambuka, M. Jiang, L. Zhou, J. Zhou, R.-A. Eichel, and P. H. L. Notten, "Overpotential analysis of graphite-based Li-ion batteries seen from a porous electrode modeling perspective," *Journal of Power Sources*, vol. 509, p. 230 345, 2021, ISSN: 0378-7753. DOI: https://doi.org/10.1016/j.jpowsour.2021.230345.

[21] S. Wang, H. M. Amdadul, C. Fernandez, and C. Yu, *Battery State Estimation - Methods and Models*. Institution of Engineering and Technology (The IET), 2021, pp. 11–84, ISBN: 978-1-83953-529-1. [Online]. Available: https://app.

knovel.com/hotlink/khtml/id:kt012WDKV2/battery-state-estimation/mechanism--introduction.

[22] A. Barai, K. Uddin, W. D. Widanage, A. McGordon, and P. Jennings, "A study of the influence of measurement timescale on internal resistance characterisation methodologies for lithium-ion cells," *Scientific Reports*, vol. 8, no. 1, p. 21, 2018, ISSN: 2045-2322. DOI: 10.1038/s41598-017-18424-5.

[23] X. Wei, B. Zhu, and W. Xu, "Internal Resistance Identification in Vehicle Power Lithium-Ion Battery and Application in Lifetime Evaluation," in *2009 International Conference on Measuring Technology and Mechatronics Automation*, vol. 3, 2009, pp. 388–392, ISBN: 2157-1481 VO - 3. DOI: 10.1109/ICMTMA.2009.468.

[24] S. Barcellona, S. Colnago, G. Dotelli, S. Latorrata, and L. Piegari, "Aging effect on the variation of Li-ion battery resistance as function of temperature and state of charge," *Journal of Energy Storage*, vol. 50, p. 104 658, 2022, ISSN: 2352-152X. DOI: https://doi.org/10.1016/j.est.2022.104658.

[25] Suhak Lee, "Electrode-Specific Degradation Diagnostics for Lithium-Ion Batteries with Practical Considerations," *University of Michigan*, vol. 53, no. 9, pp. 1689–1699, 2021, ISSN: 1098-6596.

[26] A. Barré, B. Deguilhem, S. Grolleau, M. Gérard, F. Suard, and D. Riu, "A review on lithium-ion battery ageing mechanisms and estimations for automotive applications," *Journal of Power Sources*, vol. 241, pp. 680–689, 2013, ISSN: 0378-7753. DOI: https://doi.org/10.1016/j.jpowsour.2013.05.040.

[27] C. R. Birkl, M. R. Roberts, E. McTurk, P. G. Bruce, and D. A. Howey, "Degradation diagnostics for lithium ion cells," *Journal of Power Sources*, vol. 341, pp. 373–386, 2017, ISSN: 0378-7753. DOI: https://doi.org/10.1016/j.jpowsour.2016.12.011.

[28] X. Han, M. Ouyang, L. Lu, J. Li, Y. Zheng, and Z. Li, "A comparative study of commercial lithium ion battery cycle life in electrical vehicle: Aging mechanism identification," *Journal of Power Sources*, vol. 251, pp. 38–54, 2014, ISSN: 0378-7753. DOI: https://doi.org/10.1016/j.jpowsour.2013.11.029.

[29] Z. Gao, H. Xie, X. Yang, W. Niu, S. Li, and S. Chen, "The Dilemma of C-Rate and Cycle Life for Lithium-Ion Batteries under Low Temperature Fast Charging," *Batteries*, vol. 8, no. 11, 2022. DOI: 10.3390/batteries8110234.

[30] S. S. Zhang, K. Xu, and T. R. Jow, "The low temperature performance of Li-ion batteries," *Journal of Power Sources*, vol. 115, no. 1, pp. 137–140, 2003, ISSN: 0378-7753. DOI: https://doi.org/10.1016/S0378-7753(02)00618-3.

[31] C. Pastor-Fernández, K. Uddin, G. H. Chouchelamane, W. D. Widanage, and J. Marco, "A Comparison between Electrochemical Impedance Spectroscopy and Incremental Capacity-Differential Voltage as Li-ion Diagnostic Techniques to Identify and Quantify the Effects of Degradation Modes within Battery Management Systems," *Journal of Power Sources*, vol. 360, pp. 301–318, 2017, ISSN: 0378-7753. DOI: https://doi.org/10.1016/j.jpowsour.2017.03.042.

[32] M. Keyser, K. Gi-Heon, J. Neubauer, A. Pesaran, S. Santhanagopalan, and K. Smith, *Design and Analysis of Large Lithium-Ion Battery Systems*, 1st ed. Artech House, 2014, pp. 81–115, ISBN: 978-1-60807-713-7.

[33] G. Plett, *Battery Management Systems, Volume II: Equivalent-Circuit Methods*, 1st ed. Artech, 2015, pp. 167–236, ISBN: 9781630810283. [Online]. Available: http://ieeexplore.ieee.org/document/9100098.

[34] F. Leng, C. M. Tan, and M. Pecht, "Effect of Temperature on the Aging rate of Li Ion Battery Operating above Room Temperature," *Scientific Reports*, vol. 5, no. 1, p. 12 967, 2015, ISSN: 2045-2322. DOI: 10.1038/srep12967.

[35] P. Sun, X. Zhang, S. Wang, and Y. Zhu, "Lithium-ion battery degradation caused by overcharging at low temperatures," *Thermal Science and Engineering Progress*, vol. 30, p. 101 266, 2022, ISSN: 2451-9049. DOI: https://doi.org/10.1016/j.tsep.2022.101266.

[36] E. Wikner, E. Björklund, J. Fridner, D. Brandell, and T. Thiringer, "How the utilised SOC window in commercial Li-ion pouch cells influence battery ageing," *Journal of Power Sources Advances*, vol. 8, p. 100 054, 2021, ISSN: 2666-2485. DOI: https://doi.org/10.1016/j.powera.2021.100054.

[37] S. Barcellona and L. Piegari, "Effect of current on cycle aging of lithium ion batteries," *Journal of Energy Storage*, vol. 29, p. 101 310, 2020, ISSN: 2352-152X. DOI: https://doi.org/10.1016/j.est.2020.101310.

[38] J. Świątowska and P. Barboux, "Chapter 4 - Lithium Battery Technologies: From the Electrodes to the Batteries," in A. Chagnes and J. B. T. .-. L. P. C. Świątowska, Eds., Amsterdam: Elsevier, 2015, pp. 125–166, ISBN: 978-0-12-801417-2. DOI: https://doi.org/10.1016/B978-0-12-801417-2.00004-9.

[39] F. Hildenbrand, D. Ditscheid, E. Barbers, and D. U. Sauer, "Influence of the anode overhang on the open-circuit voltage and the ageing of lithium-ion batteries—a model based study," *Applied Energy*, vol. 332, p. 120 395, 2023, ISSN: 0306-2619. DOI: https://doi.org/10.1016/j.apenergy.2022.120395.

[40] B. Gyenes, D. Stevens, V. Chevrier, and J. Dahn, "Understanding anomalous behavior in coulombic efficiency measurements on li-ion batteries," *Journal of the Electrochemical Society*, vol. 162, A278–A283, Dec. 2014. DOI: 10.1149/2.0191503jes.

[41] S. J. An, J. Li, C. Daniel, D. Mohanty, S. Nagpure, and D. L. Wood, "The state of understanding of the lithium-ion-battery graphite solid electrolyte interphase (SEI) and its relationship to formation cycling," *Carbon*, vol. 105, pp. 52–76, 2016, ISSN: 0008-6223. DOI: https://doi.org/10.1016/j.carbon.2016.04.008.

[42] F C Walsh and M E Herron, "Electrocrystallization and electrochemical control of crystal growth: fundamental considerations and electrodeposition of metals," *Journal of Physics D: Applied Physics*, vol. 24, no. 2, p. 217, 1991, ISSN: 0022-3727. DOI: 10.1088/0022-3727/24/2/019.

[43] Z. Li, J. Huang, B. Yann Liaw, V. Metzler, and J. Zhang, "A review of lithium deposition in lithium-ion and lithium metal secondary batteries," *Journal of Power Sources*, vol. 254, pp. 168–182, 2014, ISSN: 0378-7753. DOI: https://doi.org/10.1016/j.jpowsour.2013.12.099.

[44] M. Sadd, S. Xiong, J. R. Bowen, F. Marone, and A. Matic, "Investigating microstructure evolution of lithium metal during plating and stripping via operando X-ray tomographic microscopy," *Nature Communications*, vol. 14, no. 1, p. 854, 2023, ISSN: 2041-1723. DOI: 10.1038/s41467-023-36568-z.

[45] U. R. Koleti, A. Rajan, C. Tan, S. Moharana, T. Q. Dinh, and J. Marco, "A Study on the Influence of Lithium Plating on Battery Degradation," *Energies*, vol. 13, no. 13, 2020. DOI: 10.3390/en13133458.

[46] B. Bitzer and A. Gruhle, "A new method for detecting lithium plating by measuring the cell thickness," *Journal of Power Sources*, vol. 262, pp. 297–302, 2014, ISSN: 0378-7753. DOI: https://doi.org/10.1016/j.jpowsour.2014.03.142.

[47] R. Zhang, X. Shen, Y.-T. Zhang, X.-L. Zhong, H.-T. Ju, T.-X. Huang, X. Chen, J.-D. Zhang, and J.-Q. Huang, "Dead lithium formation in lithium metal batteries: A phase field model," *Journal of Energy Chemistry*, vol. 71, pp. 29–35, 2022, ISSN: 2095-4956. DOI: https://doi.org/10.1016/j.jechem.2021.12.020.

[48] Q. Zhao, L. Hu, W. Li, C. Liu, M. Jiang, and J. Shi, "Recovery and Regeneration of Spent Lithium-Ion Batteries From New Energy Vehicles," *Frontiers in Chemistry*, vol. 8, 2020, ISSN: 2296-2646. DOI: 10.3389/fchem.2020.00807.

[49] H. Zurange, "Regeneration of Cathode Materials From Used Li-Ion Batteries Via A Direct Recycling Process," Ph.D. dissertation, Purdue University, 2020. DOI: http://dx.doi.org/10.7912/C2/2750.

[50] Z. Jiang, J. Sun, P. Jia, W. Wang, Z. Song, X. Zhao, and Y. Mao, "A sustainable strategy for spent Li-ion battery regeneration: microwave-hydrothermal relithiation complemented with anode-revived graphene to construct a LiFePO4/MWrGO cathode material," *Sustainable Energy Fuels*, vol. 6, no. 9, pp. 2207–2222, 2022. DOI: 10.1039/D1SE01750K. [Online]. Available: http://dx.doi.org/10.1039/D1SE01750K.

[51] H. A. Catherino, F. F. Feres, and F. Trinidad, "Sulfation in lead–acid batteries," *Journal of Power Sources*, vol. 129, no. 1, pp. 113–120, 2004, ISSN: 0378-7753. DOI: https://doi.org/10.1016/j.jpowsour.2003.11.003.

[52] E. Mehdi, A. El, and M. Zazi, "Impact of Pulse Voltage as Desulfator to Improve Automotive Lead Acid Battery Capacity," *International Journal of Advanced Computer Science and Applications*, vol. 8, no. 7, pp. 522–526, 2017, ISSN: 2158107X. DOI: 10.14569/ijacsa.2017.080772.

[53] S. Okuno, *Method for removing lead sulfate film formed in lead-acid battery*, 2006.

[54] A. Ohajianya, E. Mbamala, C. Amakom, and C. Akujor, "An empirical investigation of lead-acid battery desulfation using a high-frequency pulse desulfator," *Journal of Advances in Science and Engineering*, vol. 4, pp. 44–52, Jan. 2021. DOI: 10.37121/jase.v4i1.140.

[55] R. A. Gelbman, *Apparatus for Charging and Desulfating Lead-Acid Batteries*, 2001.

[56] Y. Yin, Y. Bi, Y. Hu, and S.-Y. Choe, "Optimal Fast Charging Method for a Large-Format Lithium-Ion Battery Based on Nonlinear Model Predictive Control and Reduced Order Electrochemical Model," *Journal of The Electrochemical Society*, vol. 167, no. 16, p. 160 559, 2020, ISSN: 1945-7111. DOI: 10.1149/1945-7111/abd607.

[57] P. E. de Jongh and P. H. L. Notten, "Effect of current pulses on lithium intercalation batteries," *Solid State Ionics*, vol. 148, no. 3, pp. 259–268, 2002, ISSN: 0167-2738. DOI: https://doi.org/10.1016/S0167-2738(02)00062-0.

[58] M. Abdel Monem, K. Trad, N. Omar, O. Hegazy, B. Mantels, G. Mulder, P. Van den Bossche, and J. Van Mierlo, "Lithium-ion batteries: Evaluation study of different charging methodologies based on aging process," *Applied Energy*, vol. 152, pp. 143–155, 2015, ISSN: 0306-2619. DOI: https://doi.org/10.1016/j.apenergy.2015.02.064.

[59] P.-T. Chen, F.-H. Yang, Z.-T. Cao, J.-M. Jhang, H.-M. Gao, M.-H. Yang, and K. D. Huang, "Reviving Aged Lithium-Ion Batteries and Prolonging their Cycle Life by Sinusoidal Waveform Charging Strategy," *Batteries & Supercaps*, vol. 2, no. 8, pp. 673–677, Aug. 2019. DOI: https://doi.org/10.1002/batt.201900022.

[60] J. Keil, N. Paul, V. Baran, P. Keil, R. Gilles, and A. Jossen, "Linear and Nonlinear Aging of Lithium-Ion Cells Investigated by Electrochemical Analysis and In-Situ Neutron Diffraction," *Journal of The Electrochemical Society*, vol. 166, no. 16, A3908, Nov. 2019. DOI: 10.1149/2.1271915jes.

[61] M. Z. Mayers, J. W. Kaminski, and T. F. I. I. I. Miller, "Suppression of Dendrite Formation via Pulse Charging in Rechargeable Lithium Metal Batteries," *The Journal of Physical Chemistry C*, vol. 116, no. 50, pp. 26 214–26 221, Dec. 2012, ISSN: 1932-7447. DOI: 10.1021/jp309321w.

[62] L.-R. Chen, S.-L. Wu, D.-T. Shieh, and T.-R. Chen, "Sinusoidal-Ripple-Current Charging Strategy and Optimal Charging Frequency Study for Li-Ion Batteries," *IEEE Transactions on Industrial Electronics*, vol. 60, no. 1, pp. 88–97, 2013. DOI: 10.1109/TIE.2012.2186106.

[63] M. S. Chandrasekar and M. Pushpavanam, "Pulse and pulse reverse plating—Conceptual, advantages and applications," *Electrochimica Acta*, vol. 53, no. 8, pp. 3313–3322, 2008, ISSN: 0013-4686. DOI: https://doi.org/10.1016/j.electacta.2007.11.054.

[64] Y. Qin, X. Chen, A. Tomaszewska, H. Chen, Y. Wei, H. Zhu, Y. Li, Z. Cui, J. Huang, J. Du, X. Han, L. Lu, B. Wu, K. Sun, Q. Zhang, and M. Ouyang, "Lithium-ion batteries under pulsed current operation to stabilize future grids," *Cell Reports Physical Science*, vol. 3, no. 1, p. 100 708, 2022, ISSN: 2666-3864. DOI: https://doi.org/10.1016/j.xcrp.2021.100708.

[65] X. Li, J. Jiang, L. Y. Wang, D. Chen, Y. Zhang, and C. Zhang, "A capacity model based on charging process for state of health estimation of lithium ion batteries," *Applied Energy*, vol. 177, pp. 537–543, 2016, ISSN: 0306-2619. DOI: https://doi.org/10.1016/j.apenergy.2016.05.109.

[66] L. Zheng, J. Zhu, D. D.-C. Lu, G. Wang, and T. He, "Incremental capacity analysis and differential voltage analysis based state of charge and capacity estimation for lithium-ion batteries," *Energy*, vol. 150, pp. 759–769, 2018, ISSN: 0360-5442. DOI: https://doi.org/10.1016/j.energy.2018.03.023.

[67] P. Keil and A. Jossen, "Calendar Aging of NCA Lithium-Ion Batteries Investigated by Differential Voltage Analysis and Coulomb Tracking," *Journal of The Electrochemical Society*, vol. 164, no. 1, A6066, 2017, ISSN: 1945-7111. DOI: 10.1149/2.0091701jes.

[68] P. Dillmann, D. Watkinson, E. Angelini, and A. Adriaens, *Corrosion and Conservation of Cultural Heritage Metallic Artefacts (EFC 65)*, 2013. [Online]. Available: https://app.knovel.com/hotlink/khtml/id:kt011NUEY5/corrosion-conservation/electroche-electrochemical.

[69] S. Wang, Y. Fan, D.-I. Stroe, C. Fernandez, C. Yu, W. Cao, and Z. Chen, "Battery System Modeling," in Elsevier, 2021, pp. 47–94, ISBN: 978-0-323-90472-8. DOI: https://doi.org/10.1016/B978-0-323-90472-8.00008-1.

[70] R. Srinivasan and F. Fasmin, *An Introduction to Electrochemical Impedance Spectroscopy*, 1st. CRC Press, 2021, pp. 1–25. DOI: https://doi.org/10.1201/9781003127932.

[71] W. R. Wagner, G. Zhang, S. E. Sakiyama-Elbert, and M. J. Yaszemski, *Biomaterials Science - An Introduction to Materials in Medicine (4th Edition)*, 2020. [Online]. Available: https://app.knovel.com/hotlink/khtml/id:kt012LH5R2/biomaterials-science/resistive-faradaic-capacitive.

[72] G. Seo, J. Ha, M. Kim, J. Park, J. Lee, E. Park, S. Bong, K. Lee, S. J. Kwon, S.-p. Moon, J. Choi, and J. Lee, "Rapid determination of lithium-ion battery degradation: High C-rate LAM and calculated limiting LLI," *Journal of Energy Chemistry*, vol. 67, pp. 663–671, 2022, ISSN: 2095-4956. DOI: https://doi.org/10.1016/j.jechem.2021.11.009.

[73] X. Li, A. M. Colclasure, D. P. Finegan, D. Ren, Y. Shi, X. Feng, L. Cao, Y. Yang, and K. Smith, "Degradation mechanisms of high capacity 18650 cells containing Si-graphite anode and nickel-rich NMC cathode," *Electrochimica Acta*, vol. 297, pp. 1109–1120, 2019, ISSN: 0013-4686. DOI: https://doi.org/10.1016/j.electacta.2018.11.194.

[74] M. Schindler, J. Sturm, S. Ludwig, J. Schmitt, and A. Jossen, "Evolution of initial cell-to-cell variations during a three-year production cycle," *eTransportation*, vol. 8, p. 100 102, 2021, ISSN: 2590-1168. DOI: https://doi.org/10.1016/j.etran.2020.100102.

[75] J. Sturm, A. Rheinfeld, I. Zilberman, F. B. Spingler, S. Kosch, F. Frie, and A. Jossen, "Modeling and simulation of inhomogeneities in a 18650 nickel-rich, silicon-graphite lithium-ion cell during fast charging," *Journal of Power Sources*, vol. 412, pp. 204–223, 2019, ISSN: 0378-7753. DOI: https://doi.org/10.1016/j.jpowsour.2018.11.043.

[76] I. Zilberman, J. Sturm, and A. Jossen, "Reversible self-discharge and calendar aging of 18650 nickel-rich, silicon-graphite lithium-ion cells," *Journal of Power Sources*, vol. 425, pp. 217–226, 2019, ISSN: 0378-7753. DOI: https://doi.org/10.1016/j.jpowsour.2019.03.109.

[77] R. Jung, M. Metzger, F. Maglia, C. Stinner, and H. A. Gasteiger, "Oxygen Release and Its Effect on the Cycling Stability of LiNixMnyCozO2 (NMC) Cathode Materials for Li-Ion Batteries," *Journal of The Electrochemical Society*, vol. 164, no. 7, A1361, 2017, ISSN: 1945-7111. DOI: 10.1149/2.0021707jes.

[78] B. Fuchsbichler, C. Stangl, H. Kren, F. Uhlig, and S. Koller, "High capacity graphite–silicon composite anode material for lithium-ion batteries," *Journal of Power Sources*, vol. 196, no. 5, pp. 2889–2892, 2011, ISSN: 0378-7753. DOI: https://doi.org/10.1016/j.jpowsour.2010.10.081.

[79] M. Dubarry, C. Truchot, and B. Y. Liaw, "Synthesize battery degradation modes via a diagnostic and prognostic model," *Journal of Power Sources*, vol. 219, pp. 204–216, 2012, ISSN: 0378-7753. DOI: https://doi.org/10.1016/j.jpowsour.2012.07.016.

[80] M. Dubarry, C. Truchot, B. Y. Liaw, K. Gering, S. Sazhin, D. Jamison, and C. Michelbacher, "Evaluation of commercial lithium-ion cells based on composite positive electrode for plug-in hybrid electric vehicle applications. Part II. Degradation mechanism under 2C cycle aging," *Journal of Power Sources*, vol. 196, no. 23, pp. 10 336–10 343, 2011, ISSN: 0378-7753. DOI: https://doi.org/10.1016/j.jpowsour.2011.08.078.

[81] J. Wang, J. Purewal, P. Liu, J. Hicks-Garner, S. Soukazian, E. Sherman, A. Sorenson, L. Vu, H. Tataria, and M. W. Verbrugge, "Degradation of lithium ion batteries employing graphite negatives and nickel–cobalt–manganese oxide + spinel manganese oxide positives: Part 1, aging mechanisms and life estimation," *Journal of Power Sources*, vol. 269, pp. 937–948, 2014, ISSN: 0378-7753. DOI: https://doi.org/10.1016/j.jpowsour.2014.07.030.

[82] R. Xiong, Y. Pan, W. Shen, H. Li, and F. Sun, "Lithium-ion battery aging mechanisms and diagnosis method for automotive applications: Recent advances and perspectives," *Renewable and Sustainable Energy Reviews*, vol. 131, p. 110 048, 2020, ISSN: 1364-0321. DOI: https://doi.org/10.1016/j.rser.2020.110048.

[83] A. Krupp, E. Ferg, F. Schuldt, K. Derendorf, and C. Agert, *Incremental Capacity Analysis as a State of Health Estimation Method for Lithium-Ion Battery Modules with Series-Connected Cells*, 2021. DOI: 10.3390/batteries7010002.

[84] Z. Yang, S. E. Trask, X. Wu, and B. J. Ingram, *Effect of Si Content on Extreme Fast Charging Behavior in Silicon–Graphite Composite Anodes*, 2023. DOI: 10.3390/batteries9020138.

[85] A. Mikheenkova, A. J. Smith, K. B. Frenander, Y. Tesfamhret, N. R. Chowdhury, C.-W. Tai, T. Thiringer, R. Wreland Lindström, M. Hahlin, and M. J. Lacey, "Ageing of High Energy Density Automotive Li-ion Batteries: The Effect of Temperature and State-of-Charge," 2023. DOI: 10.26434/CHEMRXIV-2023-N4CD9.

[86] W. Waag, S. Käbitz, and D. U. Sauer, "Experimental investigation of the lithium-ion battery impedance characteristic at various conditions and aging states and its influence on the application," *Applied Energy*, vol. 102, pp. 885–897, 2013, ISSN: 0306-2619. DOI: https://doi.org/10.1016/j.apenergy.2012.09.030.

[87] D. J. Noelle, M. Wang, A. V. Le, Y. Shi, and Y. Qiao, "Internal resistance and polarization dynamics of lithium-ion batteries upon internal shorting," *Applied Energy*, vol. 212, pp. 796–808, 2018, ISSN: 0306-2619. DOI: https://doi.org/10.1016/j.apenergy.2017.12.086.

[88] M. Schönleber, C. Uhlmann, P. Braun, A. Weber, and E. Ivers-Tiffée, "A Consistent Derivation of the Impedance of a Lithium-Ion Battery Electrode and its Dependency on the State-of-Charge," *Electrochimica Acta*, vol. 243, pp. 250–259, 2017, ISSN: 0013-4686. DOI: https://doi.org/10.1016/j.electacta.2017.05.009.

[89] C. Qiu, G. He, W. Shi, M. Zou, and C. Liu, "The polarization characteristics of lithium-ion batteries under cyclic charge and discharge," *Journal of Solid State Electrochemistry*, vol. 23, no. 6, pp. 1887–1902, 2019, ISSN: 1433-0768. DOI: 10.1007/s10008-019-04282-w. [Online]. Available: https://doi.org/10.1007/s10008-019-04282-w.

[90] Y. Zhu, F. Yan, J. Kang, C. Du, C. Zhang, and R. F. Turkson, "Fading analysis of the Li(NiCoMn)O2 battery under different SOC cycle intervals," *Ionics*, vol. 23, no. 6, pp. 1383–1390, 2017, ISSN: 1862-0760. DOI: 10.1007/s11581-016-1968-7.

[91] S. F. Schuster, T. Bach, E. Fleder, J. Müller, M. Brand, G. Sextl, and A. Jossen, "Nonlinear aging characteristics of lithium-ion cells under different operational conditions," *Journal of Energy Storage*, vol. 1, pp. 44–53, 2015, ISSN: 2352-152X. DOI: https://doi.org/10.1016/j.est.2015.05.003.

[92] M. A. Hoque, P. Nurmi, A. Kumar, S. Varjonen, J. Song, M. G. Pecht, and S. Tarkoma, "Data driven analysis of lithium-ion battery internal resistance towards reliable state of health prediction," *Journal of Power Sources*, vol. 513, p. 230 519, 2021, ISSN: 0378-7753. DOI: https://doi.org/10.1016/j.jpowsour.2021.230519.

[93] M. Lewerenz, P. Dechent, and D. U. Sauer, "Investigation of capacity recovery during rest period at different states-of-charge after cycle life test for prismatic Li(Ni1/3Mn1/3Co1/3)O2-graphite cells," *Journal of Energy Storage*, vol. 21, pp. 680–690, 2019, ISSN: 2352-152X. DOI: https://doi.org/10.1016/j.est.2019.01.004.

[94] M. Lewerenz, A. Marongiu, A. Warnecke, and D. U. Sauer, "Differential voltage analysis as a tool for analyzing inhomogeneous aging: A case study for LiFePO4|Graphite cylindrical cells," *Journal of Power Sources*, vol. 368, pp. 57–67, 2017, ISSN: 0378-7753. DOI: https://doi.org/10.1016/j.jpowsour.2017.09.059.

[95] H. Kato, Y. Kobayashi, and H. Miyashiro, "Differential voltage curve analysis of a lithium-ion battery during discharge," *Journal of Power Sources*, vol. 398, pp. 49–54, 2018, ISSN: 0378-7753. DOI: https://doi.org/10.1016/j.jpowsour.2018.07.043.

A

Supplementary Measurement Data

A.1 Differential Charge Voltage After Ageing

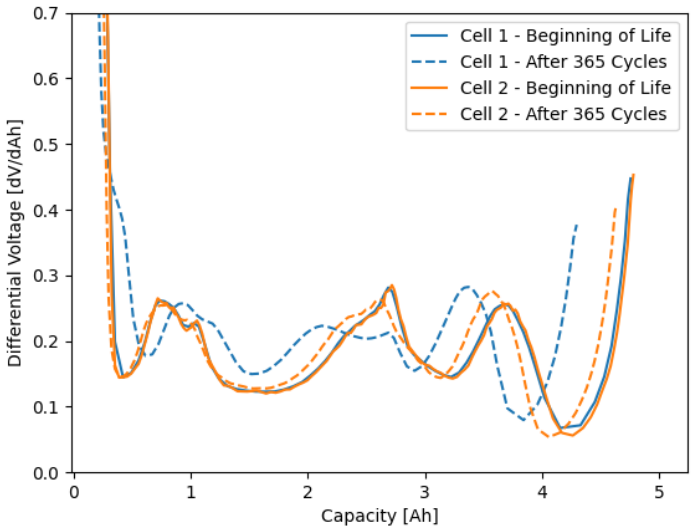

Figure A.1: Measured DV [dV/dA] plotted against charge capacity [Ah] at BoL and after 365 cycles for cell 1 and 2.

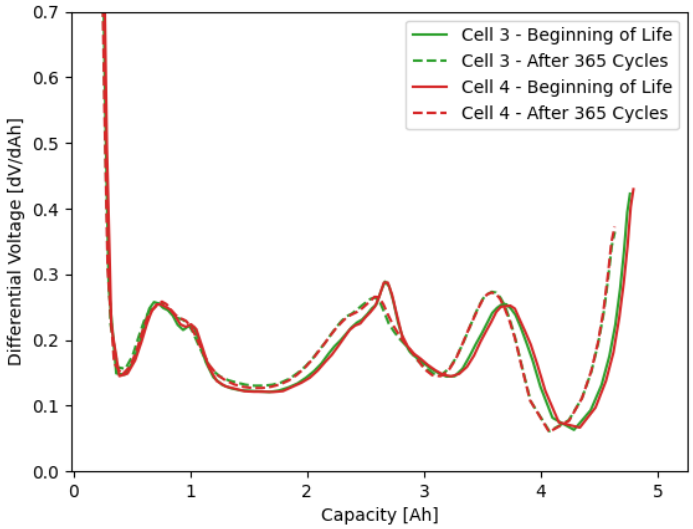

Figure A.2: Measured DV [dV/dA] plotted against charge capacity [Ah] at BoL and after 365 cycles for cell 3 and 4.

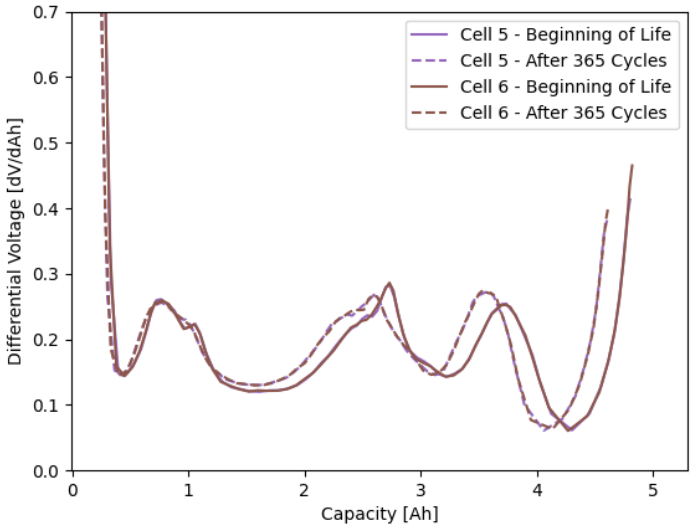

Figure A.3: Measured DV [dV/dA] plotted against charge capacity [Ah] at BoL and after 365 cycles for cell 5 and 6.

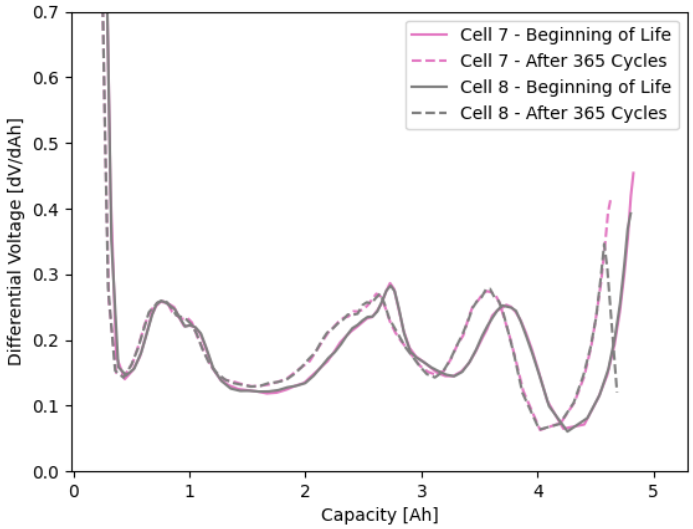

Figure A.4: Measured DV [dV/dA] plotted against charge capacity [Ah] at BoL and after 365 cycles for cell 7 and 8.

A.2 Differential Charge Voltage After Storage

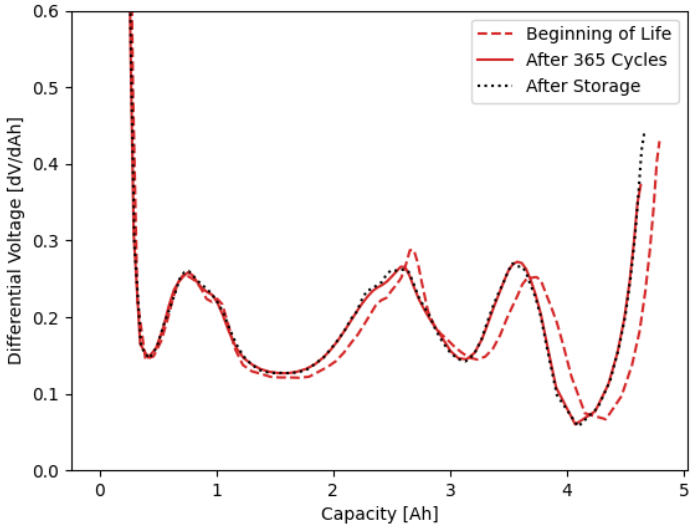

Figure A.5: Measured DV [dV/dA] plotted against charge capacity [Ah] at BoL, after 365 cycles and after storage for cell 4.

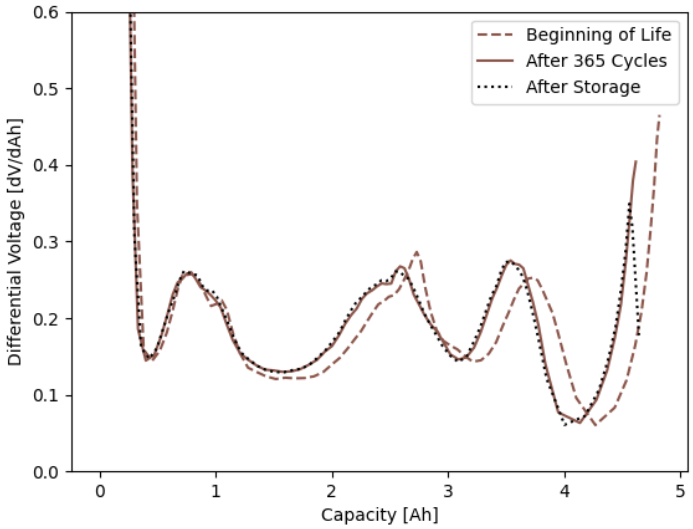

Figure A.6: Measured DV [dV/dA] plotted against charge capacity [Ah] at BoL, after 365 cycles and after storage for cell 6.

A.3 Differential Charge Voltage After Regeneration

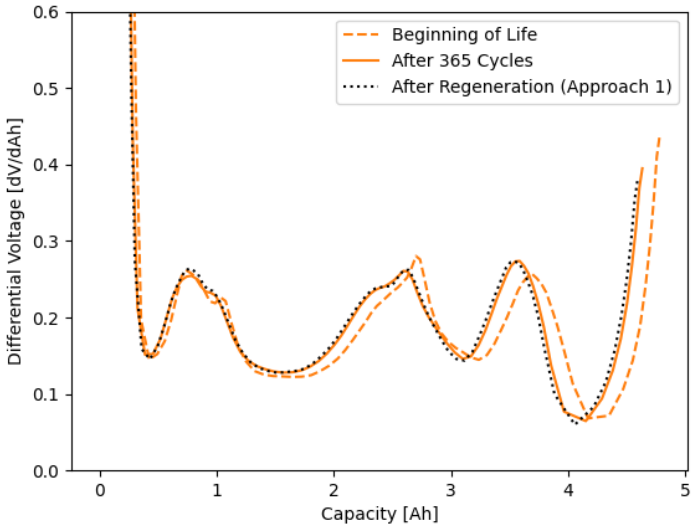

Figure A.7: Measured DV [dV/dA] plotted against charge capacity [Ah] at BoL, after 365 cycles and after regeneration using Approach 1 for cell 2.

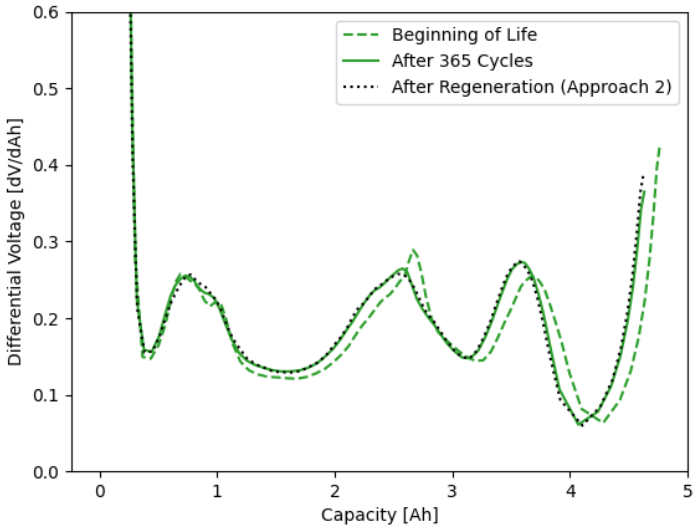

Figure A.8: Measured DV [dV/dA] plotted against charge capacity [Ah] at BoL, after 365 cycles and after regeneration using Approach 2 for cell 3.

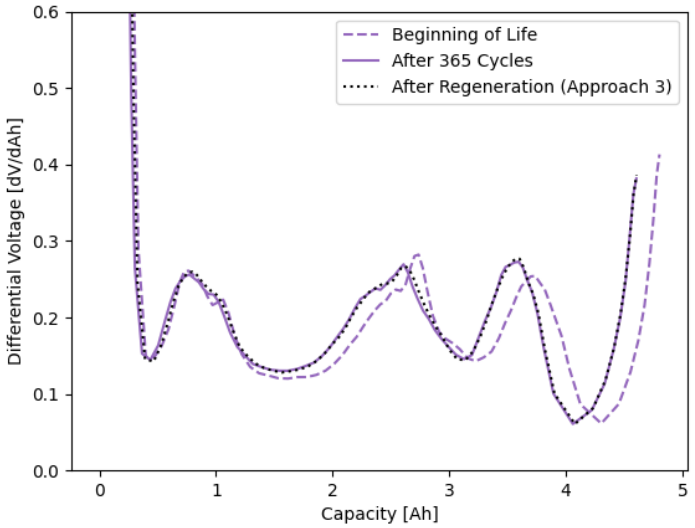

Figure A.9: Measured DV [dV/dA] plotted against charge capacity [Ah] at BoL, after 365 cycles and after regeneration using Approach 3 for cell 5.

A.4 Incremental Capacity After Regeneration

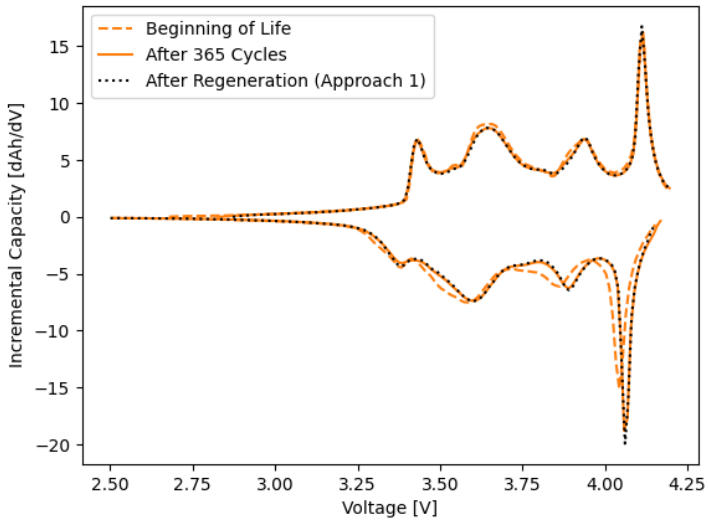

Figure A.10: Measured IC [dAh/dV] plotted against voltage [V] at BoL, after 365 cycles and after regeneration using Approach 1 for cell 2 during charge and discharge.

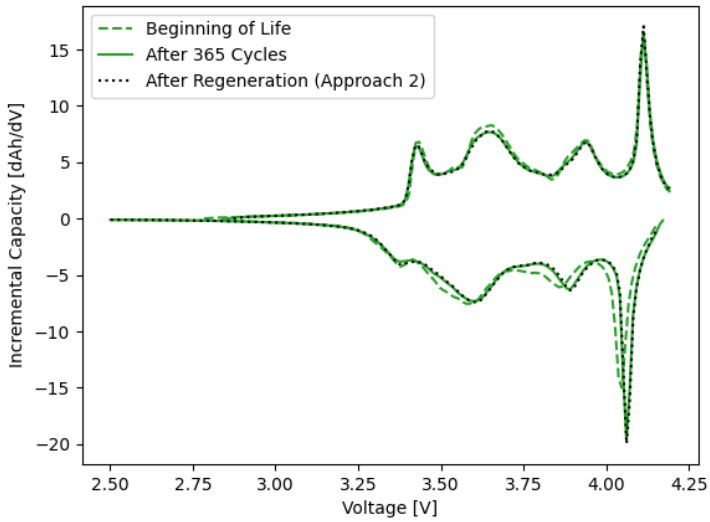

Figure A.11: Measured IC [dAh/dV] plotted against voltage [V] at BoL, after 365 cycles and after regeneration using Approach 2 for cell 3 during charge and discharge.

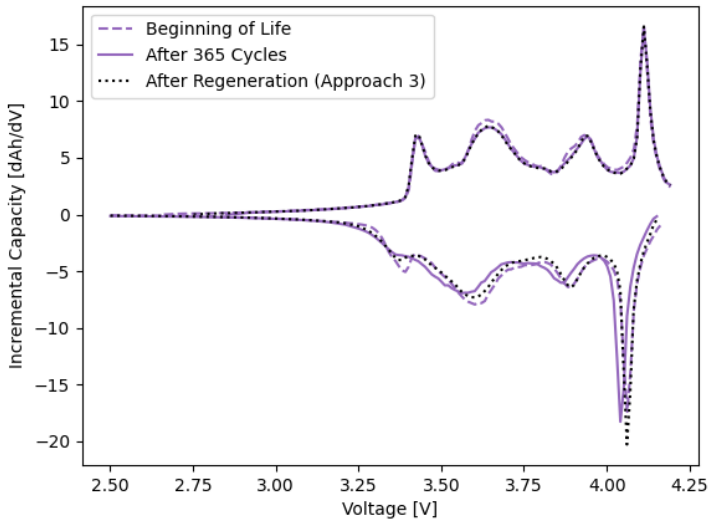

Figure A.12: Measured IC [dAh/dV] plotted against voltage [V] at BoL, after 365 cycles and after regeneration using Approach 3 for cell 5 during charge and discharge.

A.5 Temperature Evolution During Ageing

Table A.1: Measured average temperature for cells 1-8 during 365 cycles.

	Cell 1	Cell 2	Cell 3	Cell 4	Cell 5	Cell 6	Cell 7	Cell 8
Average Temperature [C°]	27.17 ±2.2	26.98 ±2.2	25.37 ±2.2	24.69 ±2.2	26.19 ±2.2	28.60 ±2.2	28.81 ±2.2	27.79 ±2.2

DEPARTMENT OF CHEMISTRY & CHEMICAL ENGINEERING
CHALMERS UNIVERSITY OF TECHNOLOGY
Gothenburg, Sweden
www.chalmers.se

CHALMERS
UNIVERSITY OF TECHNOLOGY